UNIVERSITY OF OKLAHOMA

Graduate College

Developing Selective Conversion of Oxygenates through a Combined Experimental and Computational Approach

A DISSERTATION

SUBMITTED TO THE GRADUATE FACULTY

In partial fulfillment of the requirements for the

Degree of

DOCTOR OF PHILOSOPHY

By

Mohammed Reda Bababrik
Norman, Oklahoma
2019

Developing Selective Conversion of Oxygenates through a Combined Experimental and Computational Approach

A DISSERTATION APPROVED FOR THE SCHOOL OF CHEMICAL, BIOLOGICAL AND MATERIALS ENGINEERING

BY THE COMMITTEE CONSISTING OF

Dr. Bin Wang, Chair

Dr. Steven P. Crossley

Dr. Daniel E. Resasco

Dr. Paul Huang

Dr. Garg Jivtesh

With love to my parents, Boubker Bababrik, Khadija Hindi, My Sisters, Narjisse Bababrik, Hajar Bababrik, my brother Youssef Bababrik, my brothers-in-law, Abdellatif Bennani, Ahmad Chbani, my nephew, Saleem Bennani, and my nieces, Layla and Ghita Bennani

Acknowledgements

I would like to convey my utmost gratitude to my advisor, Dr. Bin Wang. His emphasis on leadership, communication, and professional development is seldom seen in academia and has prepared me to confidently face the next challenge. His dedication to his students and to research has been a major source of inspiration. He has become a research I will always thrive to resemble. Beyond education, he has been a great support on a personal level. I will forever be grateful that he put and kept his faith and continued his support during the difficult times. I am also thankful for the freedom he gave me in research. I would like to also thank all my committee members, Dr. Daniel Resasco, Dr. Steven Crossley, Dr. Paul Huang, and Dr. Garg Jivtesh for their guidance throughout my career as a graduate student. I would like to thank Dr. Resasco, Dr. Crossley, and Dr. Lobban for the brainstorming meetings and ideas through these years.

I am also grateful for the outstanding colleagues and friends I was able to encounter in the department. Your assistance, collaboration, and friendship made my journey easier and enjoyable. With special thanks to Tong Mou, Dr. Nicholas Briggs, Dr. Taiwo Omotoso, Dr. Abhishek Gumidyala, and Dr. Lawrence Barrett for training me on lab equipment. I would also like to express my gratitude for having the opportunity to work with some of the most diligent collaborators. A special thanks to Dr, Zhen Zhao for the contributions he made which helped bring our work to the highest level.

Last but not least, I would like to express my deepest gratitude to my family and friends back at home in Morocco. Their company and moral support through WhatsApp have helped me during tough times. My parents have supported me financially and ensured the best educational environment during both my undergraduate and graduate college years. Your support and

encouragement made me the man I am today, and I am forever grateful for that. I hope one day I can repay you for all you've done.

Table of Contents

List of Tables

List of Figures

Abstract

In this thesis, several gaps for oxygenated biomass compounds conversion on transition metals have been addressed. Through a combined computational and experimental approach, several factors affecting selectivity in heterogeneous catalysis were investigated. Ligand interaction with surface supported metal-organic complexes, substrate-metal bond strength, solvent effect, and electrode potentials have all been known as major factors in controlling selectivity. We were able to study the effect of the aforementioned factors by studying different catalytic reactions.

The first part of study consisted of investigation of metal–organic complexes on metal surfaces, in which we show how the substrate influences their interaction with ligand species. The study was motivated by the desire to design future catalysts and molecule-based devices. Of particular relevance are metal-supported porphyrins and phthalocyanines, a class of molecules with a tetrapyrrole macrocycle that can act as a chemical cavity. Into this cavity a wide variety of metal cations can be coordinated, providing these molecules with diverse functional properties for a broad range of applications, specifically in highly selective heterogeneous catalysts. Utilizing a benchmark DFT study by comparing different functionals, we were able to predict that the electronic effect on the iron phthalocyanine/water moiety on the Ag (111) surface is remarkably similar to that of coordination with an ammonia molecule. However, the main difference between the traditional *trans*-effect and the "surface *trans*-effect" is that, rather than involving a direct interaction between the metal complex center and an atom in the coordinating ligand, it is the interaction between the metal complex center and the delocalized electronic states of the metal substrate that drives the surface *trans*-effect. The prediction of the remarkable similarity of the electronic effect of the "surface *trans*-effect" to the traditional *trans*-effect, as shown in the charge

redistribution maps, strongly suggests that this phenomenon is truly a *trans*-effect, not only in appearance, but also in physical manifestation. Surprisingly, though it manifests a *trans*-effect, this effect is not due to an interaction with a single substrate atom, but instead with the surface delocalized electrons making this a true surface, rather than a local effect.

The second part of the study consisted of investigating a detailed reaction mechanism by including adsorption and surface reaction on metal substrates. DFT calculations were used to explain experimental results reported in literature. We found that the reaction of gamma-valerolactone (GVL) on Ru (0001) favored decarbonylation to produce 2-butanol. Multiple routes of GVL reaction on the transition metal were considered. The routes to produce 1,4 pentadiol, 2-pentanol, 2-butanol, and 2-MTHF all shared a common intermediate; however, the rate-limiting step varies from hydrogenation in the case of 1,4 pentadiol and 2-pentanol, to decarbonylation in the case of 2-butanol. The identification of the rate limiting steps can be used as a guide for design of new catalysts with tailored reaction selectivity.

In heterogenous catalytic reactions of oxygenated biomass compounds upgrading, reactions are usually carried out in the presence of water. Though many previous studies of the solvent effect have been reported, the role that solvents play in altering the kinetics and thermodynamics of a reaction remains to be explored. In particular, despite its presence in biomass, the effect of water in heterogenous catalysis is not well defined. In chapter 4, we introduced an explicit solvent in our theoretical and experiment study of furfural hydrogenation on Pd (111). We found that water stabilizes the system resulting in lower reaction energies. The low energies resulted in an increase in reaction rates in an aqueous phase compared to reaction conducted in cyclohexane. Water solvents form hydrogen bonds with the polar aldehyde group in furfural, and this interaction results in a change in the adsorption mode of furfural. The interaction of the aldehyde group with metal is weakened by the presence of water resulting in a lower activation energy of the hydrogenation

steps to form furfuryl alcohol. Furthermore, we showed that water can participate directly in the reaction and act as a proton donor through the Grotthuss mechanism. A microkinetic study was carried out on the system to show that the rate of the hydrogenation of the oxygen decreases when water is present. The rate of this step is further increased when hydrogen is picked up by a water, and, through a network of hydrogen-bonded water molecules, the hydrogen is transferred to oxygen of the aldehyde group.

To add another degree of complexity, an electrode potential was introduced to the electrocatalytic reaction as descried in Chapter 6. We compared conventional thermal reactions, where heat is the primary energy source to drive the reaction, with electrocatalytic reactions where an electrode potential is the energy source. In addition to the energy source, the hydrogen source and reaction conditions are also different in these two methods. We studied the reaction of furfural on copper to compare the two approaches. We found that selectivity of furfural is greatly influenced by bias. In thermal reactions, the hydrogenation and ring rearrangement products dominated. However, in the electrocatalytic reaction, the hydrodeoxygenation of furfural to produce 2-methylfuran was the major route especially at increasing potentials. The C-O bond in the aldehyde group was cleaved through a dehydration step. A computational study showed that, using an explicit water solvent, the hydrogenation of the aldehyde group was energetically favored. However, by applying a potential, the activation energies for the dehydration steps become energetically favored as these steps consist of a transfer of an H^+ and e^-, in which the energy of the electron is controlled through the bias. The advantage of this electrocatalytic strategy includes high selectivity toward attack of the oxygen-containing polar functional groups, room temperature and ambient pressure in the absence of an external hydrogen source. This study shows the potential of electrocatalysis in the upgrading of oxygenated biomass compounds.

Chapter 1: Introduction

1.1 Oxygenates in Biomass

Throughout mankind's history, Plant biomass has been employed to provide vital products such as food, energy, and feed along with valuable goods that improved standards of living such as flavors and fragrances. However, in the latter half of the 19th century, the discovery of fossil fuel created an inexpensive energy source which helped industrialize our society and improve conditions of life on different fronts. In the last two decades, concerns have been raised about the current situation where most of the energy demand is met by a single source (fossil fuels) especially in the transport sector[1]. Interest in a more flexible system combining multiple energy sources increased sharply in order complement petroleum production within the finite existing reservoirs and decrease greenhouse gas emissions. Dwindling fossil feedstocks and greenhouse effect are not the only factors pushing the chemical society into looking at renewable carbon sources. The chemistry from biomass derived chemicals can give rise to a new portfolio of products that have no resemblance among those currently manufactured through fossil fuel based hydrocarbons[2, 3].

Utilization of renewable carbon sources in the production of fossil fuel like compounds and attractive chemicals requires obtaining an inexpensive and abundant biomass feedstock. Biomass feedstock can be obtained from waste materials, forest products, aquatic biomass, and energy crops. These lignocellulose containing sources are attractive biomass feedstocks because they are considered non-edible, therefore they do not interfere with the food supply. Lignocellulosic biomass must be first separated into its constituent parts (cellulose (40-50%), hemicellulose (25-35%), and lignin (15-20%)) and then processed to produce upgradable platforms that can be converted into transportation fuels and renewable chemicals[3].

The two main strategies employed to process lignocellulosic biomass are thermochemical and hydrolysis[3-6]. Thermochemical upgrading of biomass feedstock can take place by gasification, pyrolysis, or liquefaction. All three routes employ harsh conditions (high temperatures and pressures) making them less appealing[7, 8]. In gasification, biomass is partially combusted under elevated temperature (1000K) in the presence of air, oxygen, or steam to produce syngas composed of mainly CO and H_2. Through Fisher-Tropsch synthesis, gaseous products from biomass gasification can be upgraded to gasoline or diesel. One of the limitations of the gasification route is the abundant presence of water in biomass which is conventionally considered a negative effect in the Fisher-Tropsch synthesis process. The second route for the thermochemical upgrading of biomass is through pyrolysis. At elevated temperatures and short residence times, lignocellulosic biomass feedstock is decomposed into a liquid mixture containing hundreds of different oxygenated compounds[9-11]. However, due to the properties of the liquid (high acidity, corrosive, and low energy density), an extensive purification treatment is needed in order to make the pyrolysis products suitable for use as fuel. In contrast with the gasification route where gas products are upgraded to fuel, liquefaction is an alternative route where liquid bio-oil is produced through a catalytic thermal decomposition of large molecules at higher pressures (5-20 atm) and longer residence times compared to pyrolysis, the resulting unstable shorter compounds then polymerize to form bio-oils[3].

Another main approach for primary processing of lignocellulosic biomass is through hydrolysis. Strong acids, such as HCl, H_2SO_4, and HNO_3, in aqueous environment are used to decompose polysaccharides through a sequence of reactions involving protonation, dehydration, cleavage of bonds, and deprotonation into the corresponding sugars[5]. The isolated sugars can then be further upgraded through catalytic reactions into compounds such as furfural,

hydroxymethylfurfural, levulinic acid, and γ-valerolactone, all of which serve as important building blocks for fuel additives[1].

Aside from which strategy is employed to process lignocellulosic biomass, the bio-oil product is a complex mixture of unstable, highly reactive oxygenates as shown in Figure 1[3, 4, 12]. Catalytic treatment of the platform molecules produced through primary processing of biomass is necessary in the synthesis of more stable intermediates and fuel additives[13, 14].

Multiple catalytic upgrading chemistries have been studied for the different unique chemical species produced following the primary thermal treatment of biomass. As shown in Figure 1, most of the products have a low carbon number. Carbon-carbon coupling is necessary to increase the density and reach fuel range species.

Chemical approaches for integrating low carbon number compounds into higher carbon number compounds have been studies for bio-oils. Ketonization, in which two carboxylic acids are coupled to produce a higher carbon number ketone, is one of the main chemistries adapted for the catalytic upgrading of the decomposed products from hemicellulose, cellulose, and lignin. During this process, CO_2 is released affecting the carbon yield of the reaction[15]. Aldol condensation is another chemistry route that combines two carbonyl compounds in the presence of a base or acid catalyst to produce a ketone while retaining all original carbon[16]. Chemistries such as alkylation, hydroxyalkilation, and acylation have been employed to upgrade the aromatics such as phenolics and furfurals which represent a significant portion of the bio-oil (Figure 1). The latter chemistries allow for the retention of most of the carbon while producing higher carbon compounds. Oxidation and hydrogenation of aldehydes, alcohols, and sugars to produce carboxylic acids and alcohols respectively are important chemistries employed to yield intermediates for the alkylation and ketonization routes.

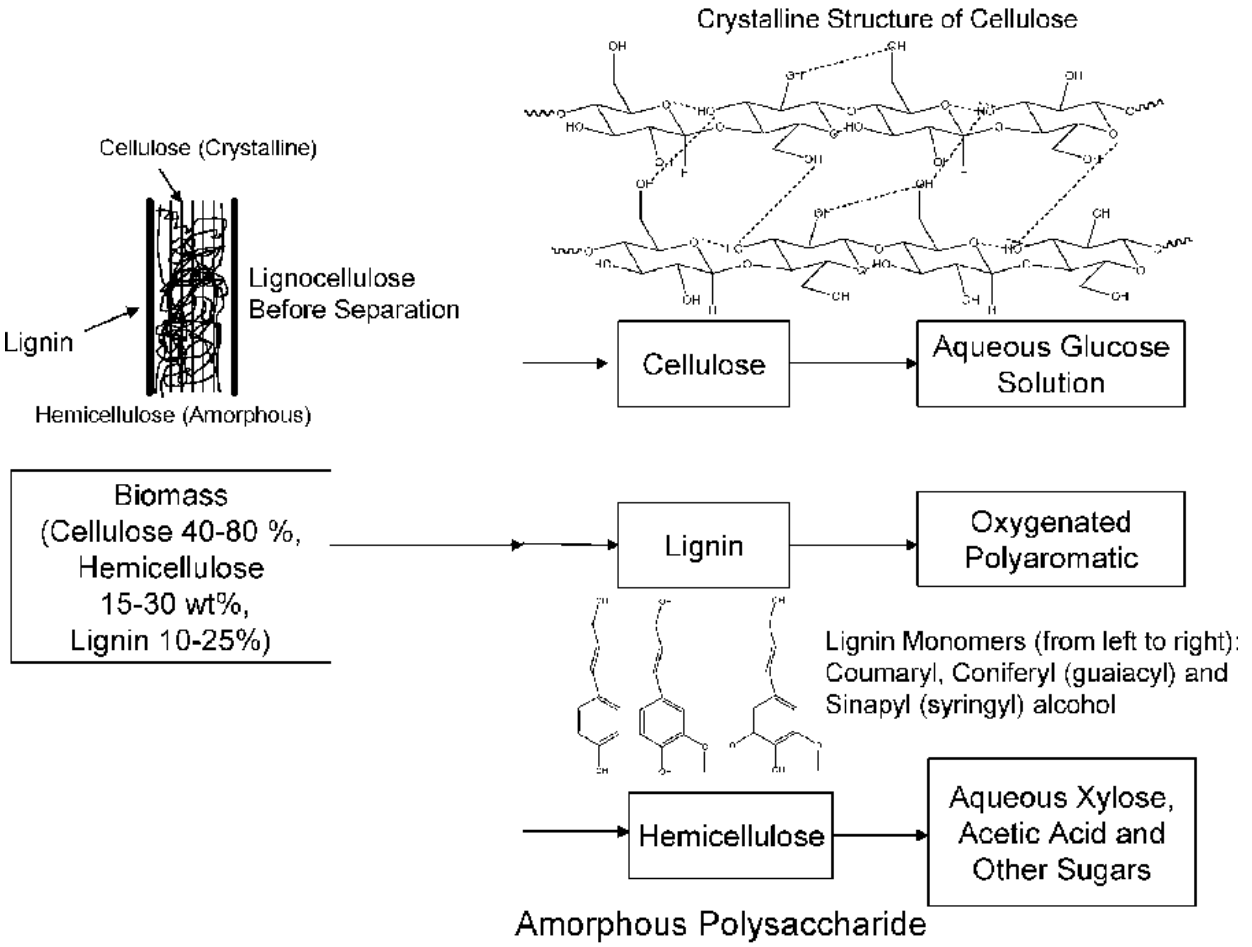

Figure 1. Structures of biomass fractions before and after reactions (Adapted from [4])

Hydrodeoxygenation is considered the critical step in the production of fuel from bio-oils. The removal of oxygen in the presence of hydrogen through dehydration or subtraction of CO_2 is usually performed after carbon-carbon coupling step. Hydrodeoxygenation through the dehydration route is always preferred as it allows for the retention of the carbon yield. Hydrogen is produced industrially through steam reforming which required harsh conditions. Controlling and minimizing the amount of hydrogen consumed in the hydrodeoxygenation route is of paramount importance in the economical optimization of producing fuel from biomass. To achieve maximum yields while minimizing the hydrogen consumed and avoiding side reactions, extensive research

has been dedicated to understanding the detailed mechanism and investigating selectivity for hydrodeoxygenation reactions of different bio-oil compounds[17, 18].

1.2 Catalytic selectivity in hydrogenation and hydrodeoxygenation reactions

Controlling catalytic selectivity represents a fundamental challenge in reaction engineering and is critical for increasing efficiency of chemical separation by minimizing production of undesired byproducts. This challenge becomes particularly true for heterocyclic, renewable oxygenates such as biomass-derived furanics and phenolics, selective conversion of which may contribute significantly in distributed energy and chemical production in developing countries[19]. Conversion of these oxygenates involves multiple reaction paths that lead to a variety of different products (Figure 2)[20-24]. These competing reactions include hydrogenation of the C=C and C=O bonds, C-O and C-C bond scission, ring opening and rearrangement, and polymerization; high selectivity of catalytic conversion of these oxygenates is critical for their applications as renewable fuels, lubricants and composites[25-27].

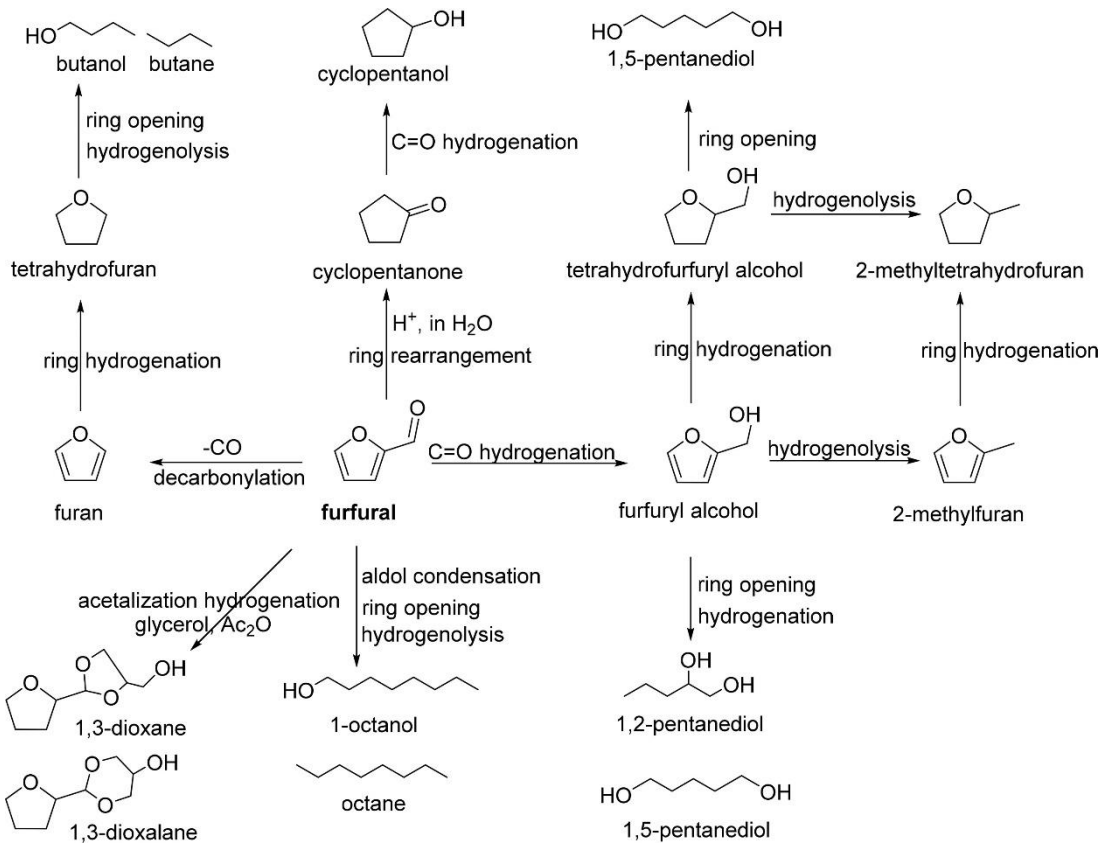

Figure 2. Reductive conversion of furfural to chemicals and biofuels (Adapted from [24])

As stated in 1.1, hydrodeoxygenation reactions have been widely used in processing of both petroleum and biomass. Because of the importance of this step for producing fuel products, extensive research has been dedicated to understanding the controlling parameters in reactions to remove oxygen in the presence of hydrogen.

Several metal catalysts such as Pt, Pd, Ru, Au, Rh, Ni, Cu, Co, and Fe have been shown to catalyze the hydrogenation and hydrodeoxygenation reactions of biomass derived compounds such as furfurals and γ-valerolactone. Catalyst selection, tuning of catalyst particle size, morphology, and surface modifications through co-adsorbates, reaction conditions, and solvents are among the most important parameters that can be tuned to achieve selective transformation[24].

In the last decade, noble metals, such as Pd, Pt, and Ru, have been the main catalysts screened for the reductive conversion of furanics due to their high activities towards hydrogenation, hydrodeoxygenation, and decarboxylation[28-30]. However, these catalysts are limited and highly expensive. Non-noble metal catalysts such as Fe, Ni, and Cu became promising alternatives provided that their activity and selectivity can be optimized through metal additives for hydrogenation and hydrodeoxygenation reactions[31, 32]. Metal promoters for example can be added to the latter metals to alter selectivity. The Fe additive has been reported to alter the adsorption conformation of furfural on Ni facets. Due to the oxophilic nature of Fe, furfural adsorption on Ni in the presence of Fe is altered. DFT calculations have shown that furfural adsorbs through both the furan ring and aldehyde group on FeNi (111) which promotes the hydrodeoxygenation of furfural to methyl furan. Additives can also be in the form of reducible supports such as TiO_2 and Fe_2O_3. The oxophilic nature of the supports enhances the interaction of C=O bond of aldehydes for example with the less oxophilic active metals, such as Au, resulting in an increase in selectivity towards the unsaturated alcohols in a hydrogenation reaction.

In addition to metal additives, it is well established in literature that metal catalyst particle size affects the distribution of adsorption sites (corners, edges, and facets) which also results in different adsorption conformations of substrates. such effects were observed for the hydrogenation and hydrodeoxygenation of furanics on noble metal catalysts. Pushkarev et al. reported that the reaction of furfural on Pt nanoparticles favored the hydrogenation route to furfuryl alcohol when the particle size was increased from 1.5 to 7.1 nm, while the selectivity towards the decarboxylation product furan decreased, suggesting that the adsorption conformation mode of furfural changed when facet surfaces predominated at high particle size[29]. Similarly, Claus et al. showed a similar correlation between hydrogenation selectivity of acrolein on Au/TiO_2 and

particle size. Reactions using larger Au particle resulted in an increase in selectivity towards C=O bond hydrogenated products against those resulting from the hydrogenation of C=C bond[33].

Reaction conditions can also alter the outcome of hydrogenation and hydrodeoxygenation reactions. Wang et al. proposed that surface coverage of the substrate and hydrogen affect the adsorption conformation of furfural on Pd (111)[34]. At higher concentrations of furfural, the substrate prefers a tilted adsorption conformation due to the adsorbate-adsorbate interaction. Similarly, hydrogen covered Pd changes the adsorption conformation of furfural from flat to tilted. This change results in a weaker interaction between the metal and the furanic ring. The hydrogenation of the aldehyde group to yield furfuryl alcohol is preferred under these conditions compared to the hydrogenation of the ring.

Nakagawa et al. also investigated experimentally hydrogen coverage effect on furfural and 5-hydroxymethylfurfural hydrogenation on monometallic Pd and Pd-Ir/SiO_2[35]. They showed that increasing hydrogen pressures improved selectivity towards hydrogenated products by suppressing side reactions responsible for producing byproducts from non-hydrogenation paths.

Along with hydrogen pressures and substrate concentrations, reaction temperature has also been used to control selectivity. Higher reaction temperatures can sometime promote side reactions affecting the selectivity and yields of desired products[35]. Higher temperatures can lead to a change in the adsorption mode of substrates and intermediates on metal surfaces. Chen et al. showed that furfural can have multiple adsorption modes on different metals. Increasing temperatures resulted a change from the η^2 -(C,O)-aldehyde adsorption mode to a η^1 - (C)-acyl species[28, 36]. The latter mode is considered a precursor for the decarbonylation route of furfural to furan, while the aldehyde adsorption mode favors the hydrogenation and hydrogenolysis routes

to produce furfuryl alcohol, tetrahydrofurfural, and methyl furan. Similar results were reported by Resasco et al. on Pd/SiO_2[18].

Another means of controlling selectivity is through modification of the metal catalyst surfaces by organic species. The reported surface modifiers, such as CO and organic ligands including thiophene, acetylene, and self-assembled monolayers (SAMs), have been shown to be effective in dictating the surface coverage and adsorption modes[21, 37]. SAMs, organic assemblies with headgroup that adsorbs strongly on the metal surface and a tail of adjustable density, act as spectators and only affect the adsorption of substrates. Medlin et al. first revealed the effectiveness of SAMs in dictating selectivity of furfural hydrogenation on Pd/Al_2O_3. In the absence of organic ligands, 95% selectivity of furan was observed. In contrast, the decorated Pd/Al_2O_3 with thiols restricted the flat adsorption conformation of furfural by decreasing the terrace sites availability resulting in a predominantly upright adsorbed furfural. The latter adsorption mode decreased the selectivity to furan from 95% to 30% while increasing the hydrogenation and hydrodeoxygenation products (furfuryl alcohol and methyl furan)[24].

In heterogenous catalysis, selectivity and reaction rates can strongly depend on solvents. Depending on the polarity of the solvent, some reaction intermediates and/or transition states bound to the catalyst surface can be stabilized resulting in modified product distributions and rate enhancements. Solvents can also be used as heat sinks and for heat transfer. They provide an extra degree of freedom to engineer reactions. The bio-oil product of biomass thermal processing is a mixture of multiple different compounds along with water as the largest cut[12]. The separation of water and building block compounds can be very expensive. Therefore, understanding the effect of solvents in general and water specifically becomes of paramount importance. In hydrogenation reactions, polar and non-polar solvents have been compared to study the effect of solvent on

furfural. Deng et al. showed that the rate of furfural hydrogenation toward furfuryl alcohol and methyl furan increases in polar media[22]. However, the effect is less when polar aprotic solvent is used such as tert-butanol compares with polar protic solvents as shown in Figure 3**. S**electivity was also greatly affected by the solvent. Polar protic solvents favored the hydrogenation of furfural to yield furfuryl alcohol. In contrast, polar aprotic solvent favored the hydrogenolysis route of furfural to form methyl furan. These findings support the idea that solvent may serve as a hydrogen donor in catalytic transfer hydrogenation reactions (Figure 3). In addition, solvents, such as water, are capable of transferring charged reaction species such as protons through the H-bonds network over long ranges resulting in hydrogen being more accessible. this process is known as the Grotthuss mechanism[38]. Solvent can also modify the adsorption geometries of reactive intermediates and transition states through hydrogen bonding or competitive adsorption resulting in differences in reaction rates and product distributions.

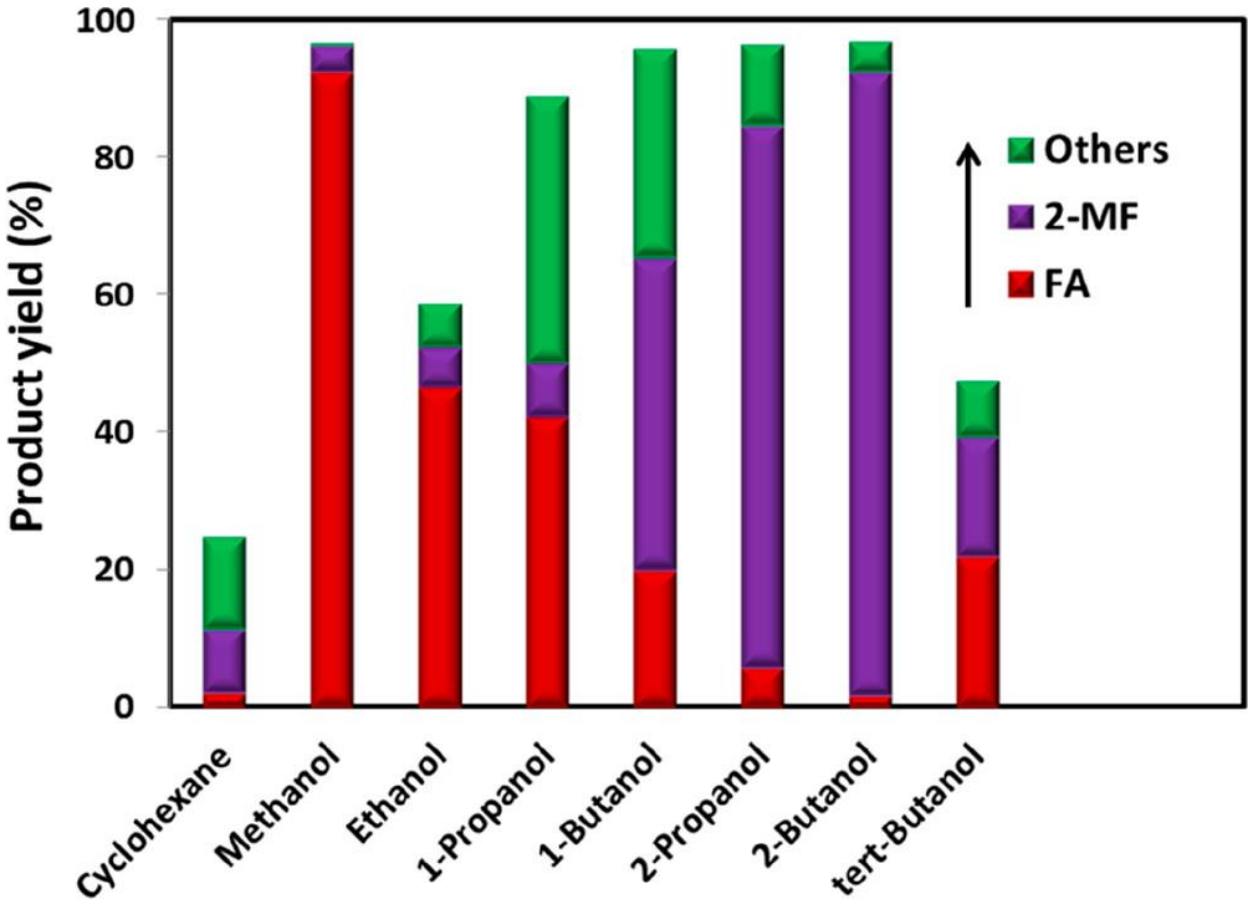

Figure 3. Solvent effects on product yields of furfural hydrogenation (Adapted from [22])

Hydrogenation and hydrogenolysis reaction studies have been carried out traditionally in batch reactors under high temperature, and pressure conditions in the presence of hydrogen gas fed into the reactor from an external source. Recently, electrochemical hydrogenation and hydrogenolysis has attracted a lot of attention since reactions can be carried in mild conditions (room temperature and ambient pressure) in the absence of an external hydrogen source. Electrocatalysis can be combined with renewable energy sources (i.e. solar cells) to yield a sustainable path to producing chemicals that can be used as solvents and/or biofuel from biomass feedstock. An advantage of electrocatalysis is the added degree of freedom (e.g. potential) that can be controlled to tune reaction pathways. The main difference between thermal and electrocatalytic

hydrogenation is the source of hydrogen. In thermal hydrogenation, hydrogen gas is fed into the reactor at high pressures. Hydrogen molecules then adsorb on the surface of the catalyst and undergo dissociation reaction according to reaction R1. The dissociated hydrogen can then be used to hydrogenate substrates adsorbed on the surface. On the other hand, in an electrochemical cell, hydrogen is produced through the oxygen evolution reaction catalyzed by the counter-electrode on the anode side according to reaction R2. Protons are then transported through the electrolyte to the cathode side of the cell where they combine with electrons on the surface of the working electrode according to R3.

$$H_2 + 2M \longrightarrow 2H^*M \qquad (R1)$$

$$\textbf{\textit{Anode}} \qquad 2H_2O \longrightarrow 4H^+ + 4e^- + O_2 \qquad (R2)$$

$$\textbf{\textit{Cathode}} \qquad H_3O^+ + e^- + M \longrightarrow H^*M + H_2O \qquad (R3)$$

1.3 Coupling between theory and experiment in heterogeneous catalysis

In heterogenous catalysis, reactions take place at the boundary between the solid catalyst and a liquid or gas phase and can be considered as the intersection where condensed-matter physics and chemistry cross. Understanding surface chemical reactions is of paramount importance in our age as heterogenous catalysis alone has been estimated to be a prerequisite of more than 20% of all production processes in the industrial world[39]. While surface science experiments provide us with quantitative description of surface phenomena, computational surface science through density functional theory (DFT) and molecular dynamics (MD) allows the understanding of the trends. Combining computational and experimental results to develop concepts in understanding which

properties determine reaction rates and product distributions can move us closer to developing efficient sustainable energy systems.

Reaction rates and selectivity for different products along with heat and mass transfer properties represent starting points in the design of a chemical reactor. Phenomenological kinetics is widely used in heterogenous catalysis in the study of reaction rates and development of reaction mechanisms. However, the latter method applies simplified assumptions which can in some cases be detrimental to the theory[40]. Phenomenological kinetics rate equations are mostly used through an adjustment of rate constants to fit experimental data. Numerous examples exist where mechanisms developed through data fitting using phenomenological kinetics rate equations and were later shown to be incorrect, or one set of experimental data could be fitted with two or more mutually exclusive mechanisms. In other cases, the collection of necessary experimental data for kinetic studies can be difficult or impossible. As a result of the limitations mentioned above, computational surface chemistry becomes valuable in providing experimental guidance and verification of developed concepts, along with predictions of kinetic parameters and mechanisms of heterogeneously catalyzed chemical reactions[41].

Chapter 2: Direct quantitative identification of the “surface trans-effect”*

2.1 Introduction

The wealth of research of the last four decades into the adsorption of molecules and molecular ligands on metal surfaces[42-53] has demonstrated the strong similarity between the behavior of these molecule–metal interactions and those found in metal coordination compounds. In particular, the local bonding of molecules to metal substrates has been found to commonly reflect the local atomic, rather than delocalized metallic, character of the surface.[49, 53] Recently, spectroscopic measurements on the adsorption of planar metallo-complexes on metal surfaces[54, 55] have been interpreted as evidence for one further example of this analogue behavior, namely the well-known trans-effect in metal coordination chemistry. Here we provide quantitative structural measurements that clearly demonstrate that this surface induced trans-effect does indeed occur in one such system, but, contrary to expectations of a local atomic effect, the results of density functional theory (DFT) calculations show that this is a true surface effect. Specifically, we show that although the charge redistribution associated with the effect mimics that of bonding to a single atom in a coordination compound, the molecule bonds not to a single localized surface atom, but rather to the metal surface as a whole.

The study of metal–organic complexes on metal surfaces, and the way in which the substrate influences their interaction with ligand species, is motivated by the desire to design future catalysts and molecule-based devices.[54, 56-69] Of particular relevance are metal-supported porphyrins and phthalocyanines,[59, 60] a class of molecules with a tetrapyrrole macrocycle that can act as a

* *Deimel, P.S., et al., Direct quantitative identification of the "surface trans-effect". Chemical Science, 2016. **7**(9): p. 5647-5656.*

chemical cavity. Into this cavity a wide variety of metal cations can be coordinated, providing these molecules with diverse functional properties for a broad range of applications in, e.g., highly selective heterogeneous catalysts,[61-63] molecular magnets,[64, 65] molecular motors,[66] spintronics[67, 68] and gas sensors,[54, 69]. However, the physical understanding and control of the processes that occur at the interface with metal supports are still in their infancy. So far, most studies conducted on these organic/metal interfaces have provided qualitative information, most prominently using scanning tunneling microscopy (STM) (e.g. ref. [54, 67, 70, 71]) and X-ray photoelectron spectroscopy (XPS) (e.g. ref. [54, 55, 62, 63, 71]). Theoretical calculations have also been performed, but comparisons of STM images with simulated images obtained from DFT calculations do not provide unique structural solutions despite being widely exploited for this purpose. The long-standing controversy concerning the structure of the Ag(111)/p(4x4)-O phase illustrates this problem.[72] Moreover, DFT calculations indicate that chemical shifts in the photoelectron binding energy of core level orbitals do not provide a unique indicator of adsorption sites and coordination environment.[73] By contrast, quantitative structural measurements can provide a relatively unambiguous benchmark upon which to test theoretical predictions.[51, 74]

One particular phenomenon that has been reported recently in this field is a Signiant electronic or chemical change in adsorbed metallo-porphyrin (MP) and metallo-phthalocyanine (MPc) based species after the addition of small molecular ligands to the metal center that has been coined the surface trans-effect. The influence of this phenomenon has had repercussions across a wide variety of fields that utilize such supported metal–organic complexes.[64, 75-78] Of particular note is the influence it has on gas sensors: in the utilization of iron phthalocyanine supported on graphene, exposure to nitric oxide apparently results in partial electron-doping of the graphene layer that manifests as a decrease in the conductance of the system.[79] The surface trans-effect may also be

the cause of the muted reactivity typically observed for MP and MPc on metal substrates,[63] where the interaction between the molecule and the surface appears to prevent reaction pathways that are available to the molecule when dissolved in a solvent.

The prototypical system, when MP and MPc molecules are adsorbed on a metallic substrate, has the central molecular macrocycle orientated (approximately) parallel to the substrate plane.[80, 81] It is this adsorption geometry that leaves the centrally coordinated metal ion close to the substrate, but also free to interact with potential ligand molecules at the position trans to (i.e. opposite to) the substrate. Flechtner et al.[54] reported that when cobalt tetraphenyl porphyrin (Co-TPP) was adsorbed onto Ag(111), a significant difference in Co 2p photoelectron binding energy was observed in XPS between single-layer and multilayer samples. However, this energy difference was greatly reduced following exposure to NO. This experimental finding was tentatively ascribed to a weakening of the interaction between the metal center of the porphyrin and the substrate caused by the ligation of NO at the position trans to the substrate. This was interpreted as being, at least phenomenologically, similar to the traditional trans-effect observed in coordination chemistry,[82-84] in which a ligand with an intense trans-effect, either through being a strong s-donor or p-acceptor, weakens the ligand–metal bond that is trans to it. In Figure. 4 a phenomenon associated with the traditional trans-effect is illustrated by a hypothetical scheme. Here, a ligand with an intense trans-effect, NO, replaces an NH_3 molecule (Figure 4a and b), weakening the NH_3–metal bond that is trans/opposite to it, and thus promoting the replacement of this ammonia molecule by a second ligand (Figure 4b and c). A consequence of this is that an intense trans-effect ligand induces a longer metal–ligand bond length at the trans position (Figure 4b), whereas a milder trans-effect ligand results in a shorter metal–ligand bond at the trans position (Figure 4c). Similarly, when dealing with octahedral coordination, as in the case of molecular

ligation to phthalocyanines and porphyrins, if molecular ammonia is replaced by molecular water, a ligand with an even milder trans-effect than ammonia, this replacement will lead to a shortening of the bond length of the remaining ammonia molecule that is trans to it (Figure 5a and b). In the proposed surface trans-effect, the surface plays the role of one of the ligands, not only inducing a trans- (or trans-like-) effect, as shown in Figure 4d and 5c, but also experiencing a trans- (or trans-like-) effect, as shown in Figure 4e and 5d. This interpretation was tested by Hieringer et al., [55] who probed the interaction of Fe-TPP, Co-TPP and Zn-TPP with NO on the Ag(111) surface using ultraviolet photoelectron spectroscopy, XPS and STM, and qualitatively comparing the shifts in the Co 2p XPS binding energy with those obtained from DFT calculations. These DFT calculations predicted a significant structural displacement of the metal ion by >0.6/0.7 A˚ for Co and >0.4/0.7 A˚ for Fe (PBE/PBE + vdW). Since the original work of Flechtner et al., several other groups have observed various electronic and chemical effects that have all been attributed to this "surface trans-effect"[60, 63, 64, 75-78, 85]. However, prior to our study, there have been no investigations of the predicted structural changes, nor has there been a quantitative comparison of theoretical predictions to experimental results.

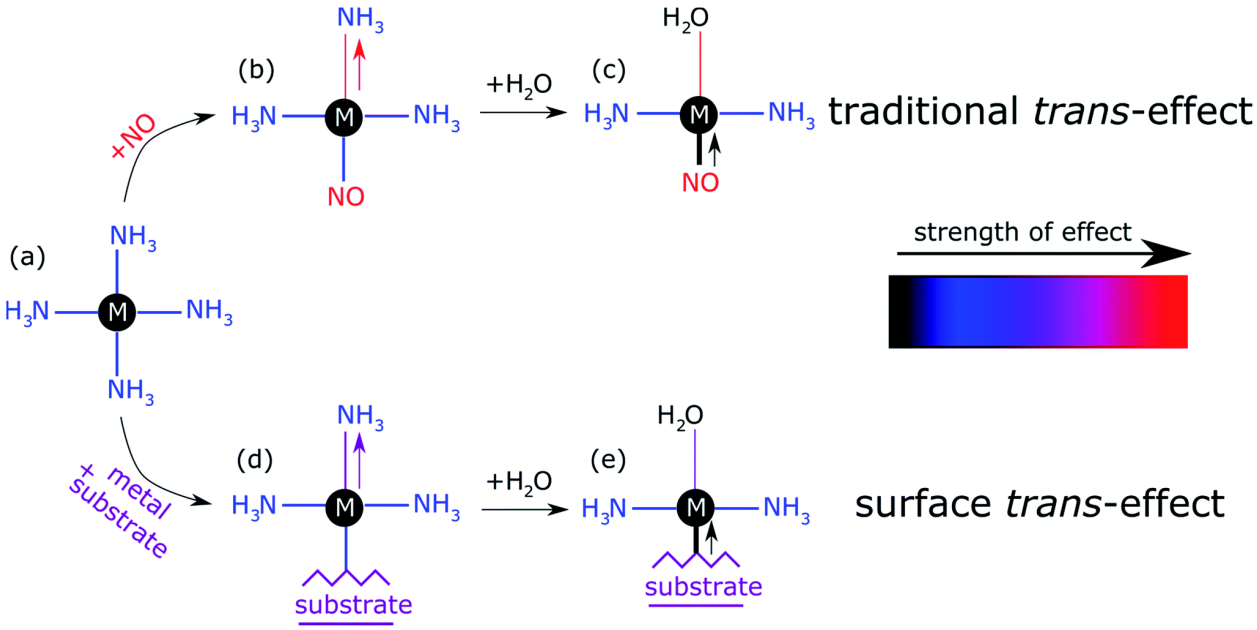

Figure 4. Schematic illustration of the traditional trans-effect and surface trans-effect for a hypothetical system, assuming that the intensity of the effect increases from H_2O < NH_3 < metal substrate < NO (indicated with the color scheme)

Here we present the results of such a quantitative experimental test of DFT predictions, utilizing normal incidence X-ray standing waves (NIXSW)[86] to measure the displacement of iron phthalocyanine (FePc – shown schematically in Figure 6a), adsorbed on a single crystal Ag(111) surface, before and after ligation of ammonia and water. The choice of system was inspired by the results of published DFT calculations (which did not include dispersion forces) predicting a 0.9 A˚ displacement of the iron centers of FePc on the Au(111) surface upon ligation of ammonia, as well as by a report of experimentally observed electronic changes indicative of the "surface trans-effect"[87].

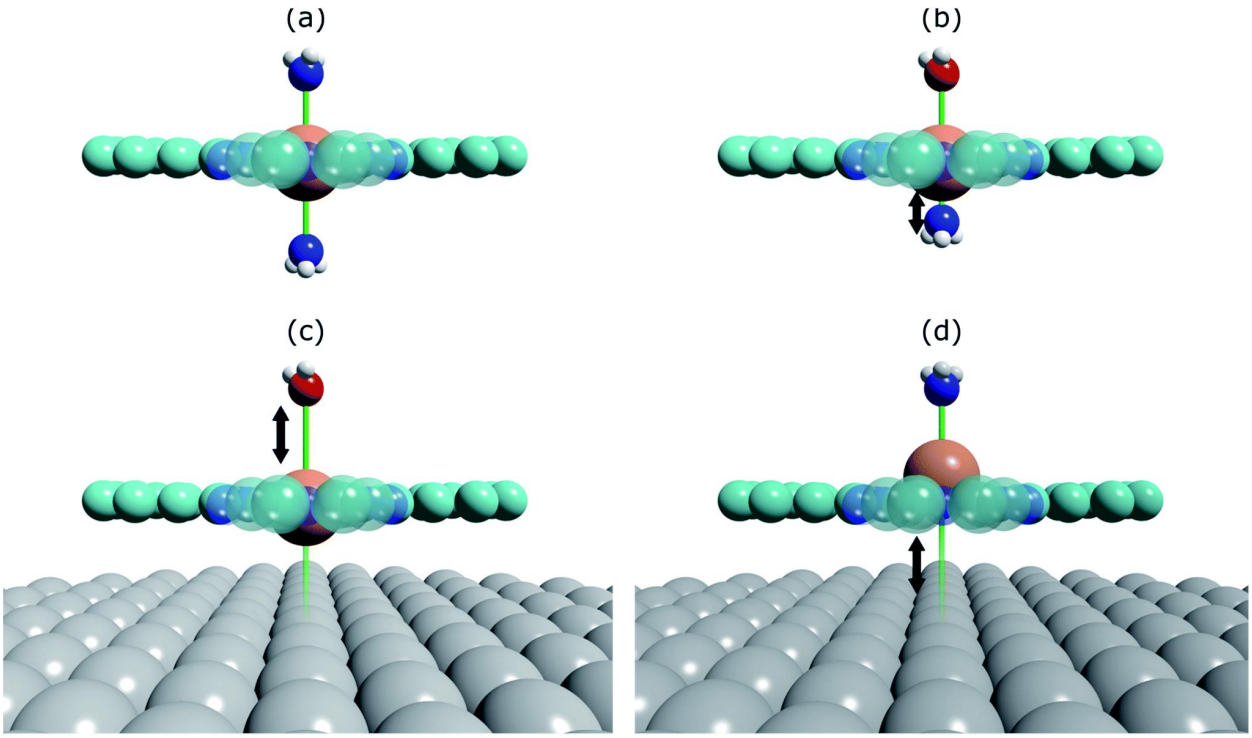

Figure 5. Structural schematics of (a) (NH_3)–FePc–(NH_3), where two ammonia molecules are trans to each other, (b) (H_2O)–FePc–(NH_3), where the ammonia molecule is trans to a water molecule, (c) (H_2O)–FePc–Ag(111), where water is trans to the Ag(111) surface, and (d) (NH_3)–FePc–Ag(111), where ammonia is trans to the Ag(111) surface

The NIXSW[86] technique exploits the standing wavefield generated by the interference between an incident photon beam and its reflected component at a Bragg condition. As the incident photon energy is scanned through the Darwin reflectivity curve, the antinodes of the standing wave move from being half way between the atomic scattering planes to being coincident with them. As the standing wave extends beyond the termination (surface) of the substrate, adsorbates that lie above the surface will experience varying electromagnetic field intensity as a function of the incident photon energy, dependent on their position relative to the extended scattered planes. Therefore, monitoring the X-ray absorption at an adsorbate atom as a function of photon energy yields a profile indicative of the average position (coherent position) of the atom relative to the scattering planes of the substrate, and a parameter related to the fraction of atoms that occupy that position (coherent fraction). By using normal incidence to scattered planes that are parallel to the

surface, the coherent position for an adsorbate species becomes equal to the average height of the adsorbate atom above the outermost substrate layer, provided that the relaxation of the outermost substrate layers can be neglected.

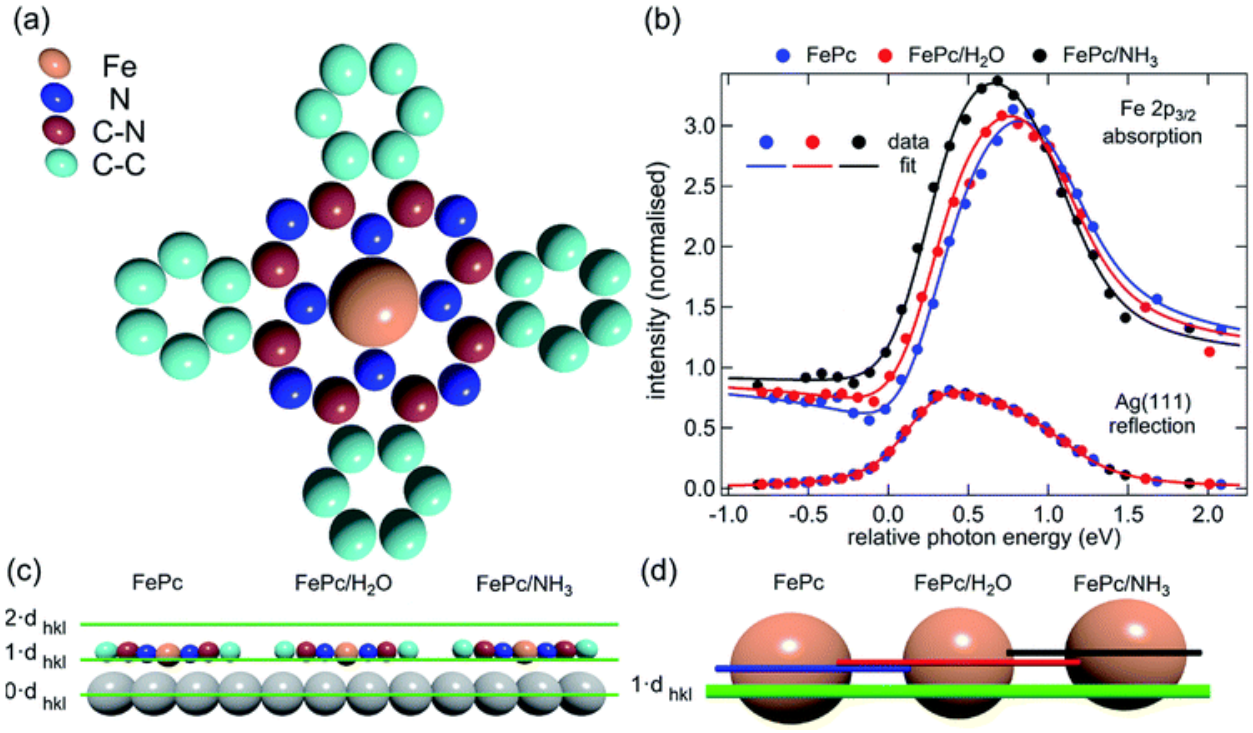

Figure 6. (a) Molecular structure of FePc. (b) Comparison of the Fe 2p3/2 X-ray absorption profiles before molecular ligation (FePc), after water ligation (FePc/H_2O) and after ammonia ligation (FePc/NH_3). (c) To scale schematic representation of the quantitative analysis of the XSW data. (d) A 4× magnification of the displacement of the Fe atoms

2.2 Methods

Experimental section

The experiments were performed by colleagues at the Technical University of Munich. XSW measurements were performed at the I09 beam line at the Diamond Light Source. The intensity and width of the (111) Bragg reflection of Ag, measured at almost exactly normal incidence, (~2640 eV at ~60 K) was acquired from a fluorescent screen mounted on the port through which the incident photons passed. The Darwin reflectivity curve was used to define the energy scale

with respect to the Bragg energy, the energy broadening due to imperfections in the monochromator (Si(111) double-crystal) and the mosaicity of the single crystal substrate (which was found to be negligible). The experimental chamber was orientated with either a 60° or 90° angle between the incident photon beam and the center of the detector, a VG Scienta EW4000 HAXPES hemispherical electron analyzer with an angular acceptance range of ±30°. The integrated intensities of the Fe 2p, N 1s and C 1s photoemission peaks were used to monitor the relative X-ray absorption of the Fe, N and C atoms, respectively. Both instrumental geometries led to similar values for the NIXSW fitting parameters once non-dipolar effects in the angular dependence of the photoemission were taken into account. Specifically, the backward-forward asymmetry parameterQ was calculated theoretically using the average angle acquired on the analyzer ($\theta = 30°$ and $\theta = 18°$ respectively, as defined in ref. [88]). To minimize radiation damage to the adsorbed molecules the sample was held at ~60 K, and the X-ray beam (defocused to approximately $300 \times 300\ \mu m^2$) was stepped over the sample during each XSW measurement such that each energy point in a single scan was acquired from a different position on the sample. The base pressure in the end station was $\sim 5 \times 10^{-10}$ mbar, which necessitated re-preparation of the sample every ~8 hours to limit the adsorption of residual water in the vacuum. A clean Ag (111) crystal was prepared by repeated cycles of Ar^+ sputtering and annealing to 800 K for 25 minutes. A multilayer of FePc was deposited by sublimation of FePc powder (Sigma Aldrich, 90% pure by dye content, triply purified[89]) at 680 K onto the sample held at room temperature. The sample was then annealed to ~600 K for 40 minutes, desorbing the excess FePc and resulting in a low energy electron diffraction pattern consistent with a saturated incommensurate single-layer described by a matrix of $\begin{pmatrix} 4.80 & -0.40 \\ 2.58 & 5.68 \end{pmatrix}$.[90] This Ag(111)/FePc system was subsequently exposed to ammonia or water by backfilling of the chamber to pressures of 10^{-8} mbar with the

substrate held at 60 K. Due to the placement of the ion gauge near the turbomolecular pump, at a significant distance from the sample, an accurate measure of the exposure rate was not possible; however the coverage of all exposures was monitored by XPS measurements (not shown) and indicated in all cases a coverage of ammonia or water greater than around 1 molecule per 3 silver surface atoms (~0.33 ML), which is greater than that required to saturate each Fe atom (~0.04 ML). Between ~0.33 ML and ~3 ML, no trend was observed in the variation of the height of the FePc molecules, as a function of ammonia (or water) coverage. At each stage of the preparation XPS was utilized to monitor any possible contaminants, and, with the exception of the aforementioned adsorption of residual water in the vacuum and damage caused by the X-ray beam after lengthy exposure, none were observed. An in-depth discussion of the data reduction will be reported in a later publication, but in all cases a Voigt lineshape was used to model the photoemission peaks, except the Fe $2p_{3/2}$ multiplet structure, which was modelled with a Gaussian lineshape. The backgrounds of the Fe $2p_{3/2}$ spectra were fitted using a template background (measured over the same energy range on the clean Ag (111) substrate), whereas Shirley backgrounds were used for the N 1s and C 1s spectra. For the N 1s spectra two Gaussians were also applied to compensate for the underlying Ag plasmons.

Computational section

The density functional calculations were carried out using the VASP package[91]. The PBE–GGA exchange–correlation potential[92] was used, and the electron-core interactions were treated in the projector augmented wave method.[93, 94] The van der Waals interaction has been taken into account through the so-called DFT-D2 and D3 semi-empirical methods via a pair-wise force field[95] or by using a non-local optB88-vdW (DFT-vdW) exchange–correlation functional.[96, 97] All the calculations were performed using a four-layer Ag slab embedded in 15 Å of vacuum

space, ensuring 10 Å separation between adjacent supercells. Structures were optimized using energies calculated at a single k point (the Γ point of the Brillouin zone) with a kinetic cut-off energy of 400 eV. The coordinates of the uppermost Ag layer and the molecules were fully relaxed until the atomic forces were smaller than 0.01 eV $Å^{-1}$. When the DFT-D2 method was used, the van der Waals interaction of either only the top layer (DFT-D2-1L), or all the layers (DFT-D2), was taken into account in the pairwise interaction[95].

2.3 Results and discussion

The XSW absorption profiles, monitored by the Fe 2p3/2 photoemission, from a single-layer of adsorbed FePc, both before and after exposure to ammonia or water, show a clear shift of the maximum of the profile to lower photon energies following molecular uptake (Figure 6b). This shift indicates that there is an increase in the coherent position, and thus in the height of the adsorbed Fe atom above the Ag (111) surface, due to additional molecular ligation. Specifically, the results shown in Figure 6b indicate that the Fe atom is at its lowest position prior to ligation, at its highest position when ligated to ammonia, and at an intermediate position when ligated to water. Quantitative analysis of the absorption profiles shows that the average height of the Fe atom changes by +0.19 ± 0.07 Å after the adsorption of ammonia, and by +0.07 ± 0.04 Å after the adsorption of water. Similar effects, though significantly smaller, were observed for the absorption profiles recorded for the carbon and nitrogen atoms, as shown schematically in Figure 6c and detailed in Table 1 (coherent positions, coherent fractions and absolute heights shown in Appendix A), indicating that there is a shift of the whole molecule to greater heights above the surface.

Also reported in Table 1 are the atomic displacements predicted by DFT calculations. The results from the DFT-D2 calculations agree surprisingly well with the experimental XSW results. The DFT-D3 calculations overestimated the effect of ammonia ligation, most notably to the Fe

metal center. The DFT-vdW calculations using optimized exchange energy also show results comparable to the experiments, but with better agreement for the absolute positions, which were overestimated for both DFT-D2 and DFT-D3 (see Appendix A). It should be noted that due to the large size of the system, hybrid functional and random phase approximation (RPA) calculations are impractical, though it is anticipated that the correction of the self-interaction using the hybrid functional will not significantly affect the predicted atomic displacement that is the focus of the present investigation.

In contrast, theoretical calculations without van der Waals corrections predict a significantly larger displacement of the entire molecule than is experimentally observed. However, the qualitative trends, e.g. a smaller displacement due to water adsorption and a smaller displacement of the molecular backbone than of the Fe atom, are reproduced. Inclusion of van der Waals corrections into the calculations decreases the size of the displacement dramatically for both ligands, bringing the theory into excellent quantitative agreement with the experimental measurements.

	Ag(111)/FePc/(NH_3)–Ag(111)/FePc				Ag(111)/FePc/(H_2O)–Ag(111)/FePc			
	Fe	N	C–N	C–C	Fe	N	C–N	C–C
XSW (Å)	0.19(7)	0.13(7)	0.07(6)	0.06(6)	0.07(4)	0.08(9)	0.01(2)	−0.02(5)
DFT (Å)	1.10	0.82	0.78	0.51	0.15	0.06	0.05	0.01
DFT-D2 (Å)	0.19	0.09	0.08	0.03	0.07	0.03	0.03	0.01
DFT-vdW (Å)	0.22	0.12	0.11	0.06	0.04	0.02	0.02	0.02
DFT + D3 (Å)	0.31	0.16	0.14	0.06	0.07	0.02	0.01	0.00

Table 1. Comparison of the experimental and theoretical displacements in the FePc height, in angstrom units, above the surface (averaged over ¨ the molecule in an atop, bridge and hollow site) for the Fe, C and N atoms upon ligation of NH_3 (Ag(111)/FePc/(NH_3)–Ag(111)/FePc) and H_2O (Ag(111)/FePc/(H_2O)–Ag(111)/FePc). The number in brackets is the uncertainty (standard error at two standard deviations) in the last decimal place.

The observed displacement of the Fe center of FePc is qualitatively consistent with the results of the DFT calculations of Hieringer et al.;[55] the weakening of the metal center interaction with the metal substrate does indeed have a structural effect similar to that expected from the

traditional trans-effect in coordination chemistry. It has long been established that adsorbates on metal surfaces follow rules comparable to those developed in coordination chemistry,[49, 98] so extending this analogous behavior to metal–organic complexes adsorbed on metal surfaces may appear entirely reasonable. However, one should question the "surface trans-effect" terminology, because the comparison with metal coordination compounds effectively requires the surface to be considered not only as having an effect comparable to a ligand, but one whose interaction with the metal center of the phthalocyanine has a specific directionality. In other words, to be physically a trans-effect the interaction cannot be mediated through long-range forces (e.g. induced dipoles or vdW forces), instead it must be induced through the sharing of an orbital of the metal center by both the surface and the ligand trans to it, in order to satisfy either a σ-donor or a π-acceptor interpretation of the traditional trans-effect.[82, 83] The hybridization of metal adatoms to metal surface atoms, when coadsorbed with molecules to form metal–organic coordination networks, has been proposed from theoretical calculations.[99, 100] However, it is not clear to what extent this is comparable to the interaction between the metal surface and the metal centers within adsorbed MP and MPc molecules. This raises the question: if it looks like the trans-effect, acts like the trans-effect, does it mean it is the trans-effect? In other words, is the term "surface trans-effect" merely a useful description of the observed phenomena in broad terms, or does it have actual physical meaning?

The overlayer studied here, a saturated single-layer of FePc on Ag(111), is known to be incommensurate with the underlying substrate.[90] However, the coherent fractions observed for the adsorbed molecule are relatively high (see Table S1†), so the variation in the height of the molecules above the surface is small, despite the local coordination of the Fe atom varying over an effective infinity of sites. If the Fe-substrate height were the same throughout the

incommensurate overlayer then the local Fe–Ag atomic distance would increase as the number of nearest neighbor Ag atoms increases (e.g. the distance is longer over a hollow site than over an atop site). This is qualitatively similar to what is observed for small molecular species when adsorbed in atop, bridge and hollow sites[49] on metal surfaces, an effect interpreted as following rules similar to those devised for coordination chemistry. However, this does not necessarily suggest that, if the interaction between the metal complex and the metal substrate follows the same general trend, then the Fe_{ads}–Ag_{surf} interaction would also be comparable to that of the ligand to metal center interaction in coordination chemistry. More generally, as there are effectively an infinite number of different local adsorption sites in the incommensurate layer, it is clear that most Fe atoms will not be directly above a Ag atom, so there will not be a silver atom in a site trans to the adsorbed molecular ligand; in contrast, the traditional trans-effect clearly suggests a strong directional influence. This implies that if the "surface-trans-effect" is indeed a trans-effect, then the substrate to metal complex interaction cannot be mediated by direct interaction to the silver atoms, instead it must be the delocalized metal surface electrons that drive the effect.

To try to address these issues, calculations for several simple model structures have been conducted, encouraged by the good quantitative agreement between the theory and the experiment in reproducing the structural consequences of this "surface trans-effect". Specifically, further calculations were performed on traditional trans-effect systems, comparing (NH_3)–FePc–(NH_3), (H_2O)–FePc–(H_2O), (NH_3)–FePc–(H_2O) and (NH_3)–FePc–(NO). The N–Fe and O–Fe bond lengths are listed in the Appendix A and compared to those of the relevant Ag(111)/FePc calculations; these values show that the effect of the Ag substrate is to induce a bond length between the trans-ligand and the Fe atom that is significantly longer than that induced by ammonia or water, but shorter than that induced by NO. This difference in bond length would place the silver

surface as having a potential trans-effect somewhere between the weak (water, ammonia) and the strong (NO) ligands. When charge redistribution maps (CRMs) are compared (Figure 7) it can be seen that the effects on the Fe center of introducing the Ag surface (Figure 7a) or an NH_3 ligand (Figure 7b) trans to a water molecule are remarkably similar. In both cases there is significant redistribution of charge into the σ-bonds that lie between the introduced species (Ag(111)/NH_3) and the Fe center, while a smaller increase in charge density occurs between the O and Fe atoms. This is mostly manifest as an accumulation of charge density in the Fe d_z^2 orbital and a comparable decrease in the Fe d_{xz} and d_{yz} orbitals. Introducing an NH_3 ligand (Figure. 7c) trans to the Ag(111) substrate has an effect on the NH_3 species similar to that produced when it is introduced trans to a water ligand (Figure 7b). However, Figure 7c shows the opposite effect occurs at the Fe metal center (charge depletion in d_z^2 and accumulation in d_{xz} and d_{yz}) when compared to the behavior seen in both Figure 7a and b. This might result from the Ag (111) having a stronger trans-effect than the NH3 ligand, indicated by the longer trans-ligand to Fe bond length for Ag, shown Appendix A. The CRMs including Ag(111) shown in Figure 7 are calculated for the Fe center above a hollow site, but similar calculations (not shown here) for an atop and a bridge site show the same effect, further indicating that it is the interaction with the delocalized metal electrons of the substrate, rather than a direct interaction with a substrate atom that drives the surface trans-effect. These calculations thus indicate that the same effect would be seen for both commensurate and incommensurate overlayers. The intensity of the surface trans-effect seen on Ag (111) appears to be dependent upon the ability to accumulate charge between the Ag(111) surface and the FePc. This may explain why the inclusion of dispersion forces dramatically changes the predicted structural differences induced by the surface trans-effect. The vdW corrections predict a less negative electrostatic potential for the clean Ag(111) surface than the uncorrected calculations do

(Figure 8). Specifically, at the measured adsorption height of the FePc molecule (~2.8 Å, corresponding to 1.2 Ag substrate layer spacings) the potential, with respect to the vacuum level, is less negative by ~0.4 eV. Therefore, in the region between the surface and the adsorbed molecule there is a significant decrease in the energy required to remove an electron to the vacuum level, i.e. the local work function has decreased. We posit that this lowering of the local work function, when using the vdW-DF functional, allows a greater charge accumulation in the σ-bonding area intensifying the Ag (111) surface trans-effect. Such a sensitivity to change in the local work function would reinforce the idea that the surface trans-effect arises from interactions with the electrostatic potential of the substrate, rather than being mediated through direct interaction with any individual atom. The theoretical calculations thus predict that the "surface trans-effect" is mediated through redistribution of charge along the trans σ-bonds in a manner similar to that of the traditional trans-effect.

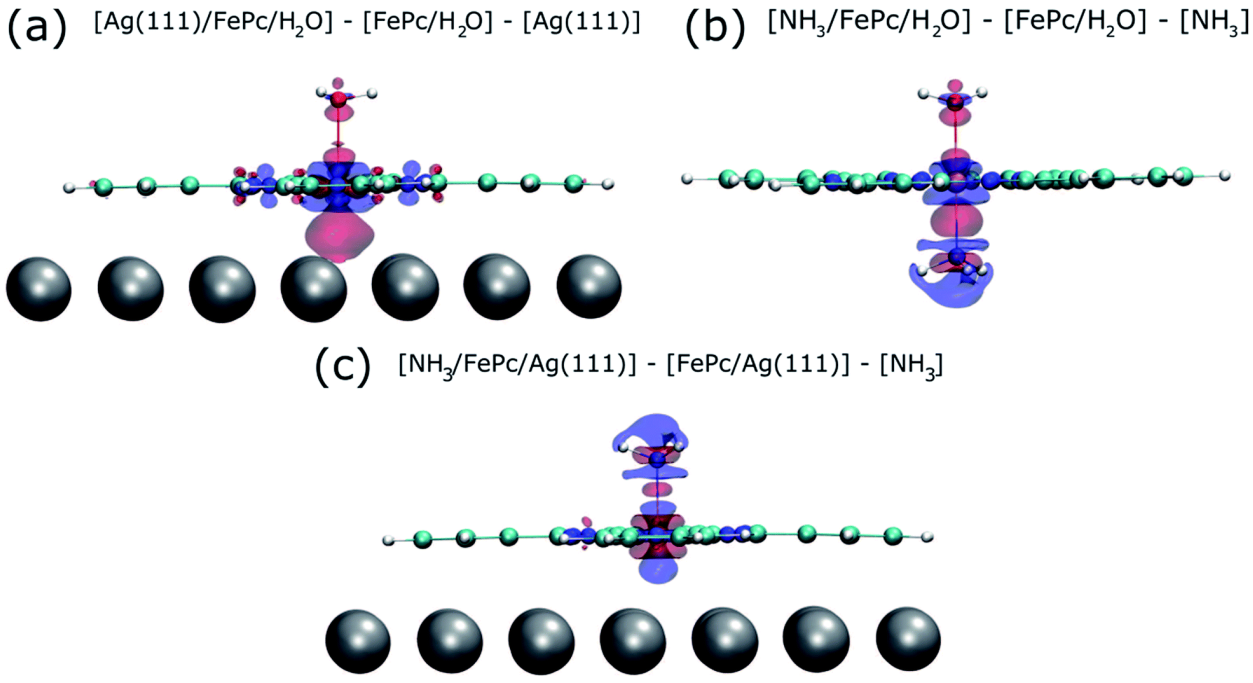

Figure 7 Charge redistribution map (CRM) showing an isosurface plot with ±0.02 e Å^{-3} (red is an increase, blue a decrease in charge density). Shown is (a) the difference caused by adding the

Ag (111) surface trans to a water molecule, (b) by adding ammonia trans to a water molecule and (c) by adding ammonia trans to the Ag(111) surface.

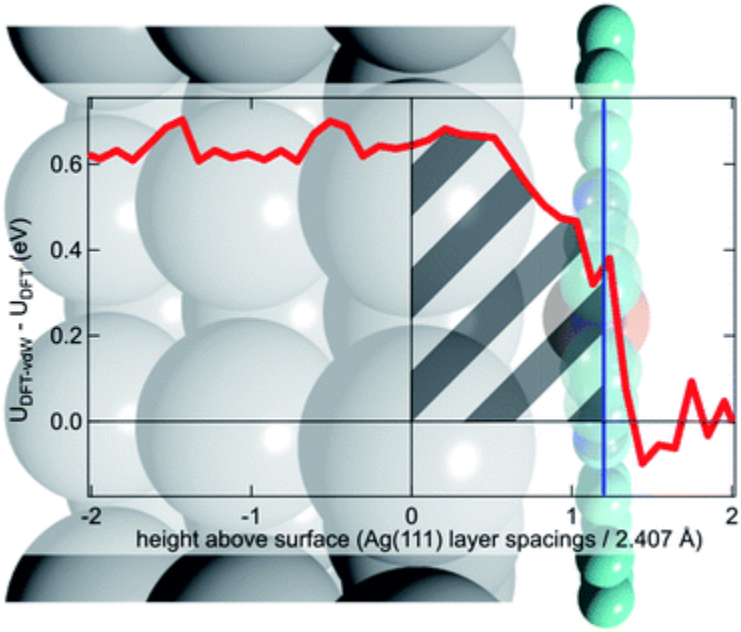

Figure 8 Difference between the optB88-vdW and PBE functionals in the calculated plane-averaged electrostatic potential from a clean Ag surface (red line), the termination of which is set at 0, overlaid atop a schematic of Ag(111)/FePc.

2.4 Conclusion

Utilizing the X-ray standing wave technique, we have obtained the first quantitative structural measurement of the consequences of the "surface trans-effect", observing the displacement of the metal center of a metal–organic species by its ligation to a molecular ligand. This displacement has been modelled by DFT calculations that show excellent agreement with the experimental results, provided that corrections are included for dispersion forces. Furthermore, these dispersion-corrected calculations predict that the electronic effect on the FePc/water moiety of introducing the Ag (111) surface is remarkably similar to that of introducing an ammonia molecule. However, the main difference between the traditional trans-effect and the surface trans-effect would seem to be that, rather than involving a direct interaction between the metal complex center and an atom

in the coordinating ligand/surface, it is the interaction between the metal complex center and the delocalized electronic states of the metal substrate that drives the surface trans-effect.

This result has wide-ranging implications in the field of metal–organic complexes supported on metal substrates. The most obvious relevance is for potential catalysts, especially considering adsorbed planar species like MPs and MPcs, as the active site is inherently trans to the substrate, and the coordination of a ligand trans to the substrate gives rise to the activated complex of such a catalyst. It can be inferred that the weakening of the metal center–ligand interaction by the substrate will suppress the reactivity of the adsorbed complex, suggesting that one cannot simply adsorb a liquid or gas phase catalyst onto a metal substrate and expect comparable activity. Instead, as concluded in our previous published work[63], it may be necessary to choose metal centers that are traditionally seen as being "too reactive" for catalytic reactions. It is also not unreasonable, as was proposed by Hieringer et al.,[55] to expect that different substrates will have varying intensities of the surface trans-effect. This extra degree of freedom could be exploited to tune the selectivity of such a catalyst, for example, in electrochemical oxygen[71] and carbon dioxide64 reduction, where the metal–organic complexes are positioned on a metallic electrode. In a similar manner, the consequences for the design of electronic devices that assume the substrate to be an inert component will be deleterious; the influence of the substrate must be considered from the outset. On the other hand, this result is potentially promising in the field of adsorbed gas sensors. As the surface trans-effect not only affects the ligand to metal center interaction, but also the surface to metal center interaction, the response of the adsorbed metal complex to a gaseous species will induce an effect on the substrate, potentially amplifying the response of the gas sensor as was observed for NO ligation to FePc on graphene.[79]

As it has now been clearly demonstrated that the surface trans-effect occurs in a manner similar to that in traditional coordination chemistry, it raises the question as to whether there is a comparable cis-effect. The cis-effect is considerably less studied in coordination chemistry than the trans-effect but can have a similar influence on the reactivity of a metal complex, especially in octahedral systems. However the experimental results presented here provide no evidence for such an effect, though some redistribution of charge in the plane of the FePc molecule was seen in the CRM's (see Figure 7a). It is therefore probable that a surface cis-effect does indeed exist, hence a study like that presented here, but investigating a system where a potential cis-effect would be expected to dominate, could be fruitful.

Finally, the prediction of the remarkable similarity of the electronic effect of the "surface trans-effect" to the traditional trans-effect, as shown in the charge redistribution maps, strongly suggests that this phenomenon is truly a trans-effect, not only in appearance, but also in physical manifestation. Surprisingly, though it manifests as a trans-effect, this effect is not due to an interaction with a single substrate atom, but instead with the surface delocalized electrons making this a true surface, rather than local, effect, thus the name "surface trans-effect" is fully justified.

Acknowledgements

The computations were performed at the Extreme Science and Engineering Discovery Environment (XSEDE) and the OU Supercomputing Center for Education & Research (OSCER) at the University of Oklahoma. I would also like to acknowledge financial support by the US Department of Energy, DOE/EPSCOR (Grant DESC0004600).

Chapter 3: Reaction Mechanism for the Conversion of γ-Valerolactone (GVL) over a Ru Catalyst: A First-Principles Study*

3.1 Introduction

Renewable oxygenates derived from lignocellulosic biomass have attracted extensive attention, because they can be converted to valuable chemicals or blended into fuels.[3, 101-106] Among a variety of these biomass-derived oxygenates, γ-valerolactone (GVL) has been particularly interesting, because of its excellent properties as a solvent of biomass-derived streams[107, 108] and the possibility of being used as a precursor for high-value chemicals.[109, 110] GVL can be produced via a multistep process in which acid catalysts convert sugars into levulinic acid, followed by noble-metal-catalyzed reduction reaction in the presence of H2.[111-113] In addition, GVL can be converted from furfural, which is also an important platform chemical obtained from thermal treatment of biomass at moderate temperatures via dehydration of xylose.[114-117] It has been reported that conversion of furfural to GVL can be catalyzed by zeolites with Bronsted and Lewis acid sites, combined with sequential transfer–hydrogenation.[117]

GVL can be converted to a variety of chemicals, such as liquid alkenes, through an integrated catalytic system.[109, 118] Hydrogenation of GVL over Cu–Cr oxide at 240–260 °C produces 1,4-pentanediol (1,4-PDO) and 2-methyltetrahydrofuran (2-MTHF).[119] The former one can be potentially used as a monomer to produce biomass-derived biodegradable polymers, and the latter has been identified as a fuel component.[112] The chemical conversion of GVL may involve a multistep process, including ring opening, hydrogenation, and dehydration.[120] Significant

* *Bababrik, R.M., B. Wang, and D.E. Resasco, Reaction Mechanism for the Conversion of gamma-Valerolactone (GVL) over a Ru Catalyst: A First-Principles Study. Industrial & Engineering Chemistry Research, 2017.* ***56****(12): p. 3217-3222.*

efforts have been focused on the use of a ruthenium catalyst, with either homogeneous molecular catalysts[120] or supported nanoparticles,[121-123] with and without a solvent environment. Using a molecular Ru catalyst, by tuning the ligands and the additives in the solution, Geilen et al. have shown that the selectivity of GVL conversion can be controlled to either a high yield of 1,4-PDO or a high yield of 2-MTHF.[120] Using heterogeneous Ru/C catalysts, Al-shaal et al. have shown that, in a solvent-free environment, GVL can be converted to a mixture of 2-MTHF, 2-butanol (2-BuOH), and small amounts of 2-pentanol (2-PeOH). They proposed that the formation of 1,4-PDO is the rate-determining step in the hydrogenation of GVL.[121] Very recently, Rozenblit et al. have investigated the aqueous-phase conversion of GVL over a Ru/C catalyst, and proposed that GVL might be converted to 1,4-PDO, 2-BuOH, and 2-PeOH in parallel paths derived from the same surface acyl species produced through the ring-opening reaction.[122] In the same study, it was shown that the major product, 2-BuOH, results from the direct decarbonylation of the acyl species. Several elementary steps, including the ring opening and decarbonylation, have been studied using density functional theory (DFT) calculations.[122] However, a detailed reaction profile has not been investigated, and it is still not clear what are the rate-limiting steps to form the various products observed, such as 1,4-PDO, 2-BuOH, and 2-PeOH.

Here, we report a complete reaction profile obtained using DFT calculations, through which we show several missing links in the previously proposed reaction mechanisms of GVL ring-opening and hydrogenation reactions. We have found that hydrogenation of the unsaturated acyl species formed after the ring-opening reaction of GVL is the rate-limiting step for the reaction path toward 1,4-PDO and 2-PeOH, because of the strong interaction between the Ru surface and the O and C atoms in the acyl species. By contrast, the rate-limiting step for the formation of 2-BuOH is the decarbonylation step. The formation of 2-BuOH has the lowest overall reaction barrier. In addition,

we show that both 2-BuOH and 2-PeOH can be formed from the same acyl intermediate, which can also be formed through dehydrogenation of 1,4-PDO. In other words, 2-BuOH and 2-PeOH can be both primary and secondary products in the conversion of GVL over a ruthenium catalyst. Finally, we provide a discussion about how these calculations can be used to interpret relevant experimental results recently reported in the literature.

3.2 Methods

DFT calculations were carried out using the VASP package.[94] The Perdew–Burke–Ernzerhof generalized gradient approximation exchange-correlation potential (PBE-GGA)[92] was used, and the electron–core interactions were treated in the projector augmented wave (PAW) method.[93, 94] Structures were optimized until the atomic forces were smaller than 0.02 eV Å–1 with a kinetic cutoff energy of 400 eV. van der Waals interactions were taken into account by incorporating the DFT-D3 semiempirical method,[95] which significantly improves the calculation accuracy of weak adsorption systems.[124] Reaction barriers were determined with the Nudged Elastic Band method.[125, 126] The Ru(0001) surface was used for the calculations, because of its low surface energy,[127] and was modeled with a 6 × 6 supercell, which contained repeated slabs with four metal layers separated by an 18 Å vacuum region. The bottom two Ru layers were fixed at their bulk positions while the top two layers were fully relaxed.

3.3 Results and Discussion

We computed several different adsorption geometries of GVL on Ru (0001) to determine the most stable structure. It was found that GVL adsorbs on the metal surface through the carbonyl carbon and carbonyl oxygen, as well as the oxygen of the furanic ring. The carbonyl carbon binds to a hexagonal close-packed (hcp) site of the Ru (0001) surface through interaction with three surface Ru atoms with a distance of 2.19 Å. Both the carbonyl oxygen and the furanic ring oxygen

bind to a surface Ru atom with distances of 2.05 and 2.21 Å (Appendix B), respectively. This adsorption configuration is in agreement with a previous calculation.[122] GVL adsorbed with this structure can undergo a ring-opening reaction with an activation barrier of 25 kJ/mol, as discussed below in Figure 9. In addition, we find an almost equally stable structure (less stable by 0.6 kJ/mol), which is shown in Appendix B, in which the carbonyl oxygen binds to a surface Ru atom with a bond length of 2.27 Å, along with the methyl group pointing toward the surface. The GVL molecule adopting this configuration needs to overcome an activation barrier of 69 kJ/mol of the ring-opening reactions (Appendix B). Considering the similar adsorption energy between these two structures, we think they may reach equilibrium at the surface and the one with the lower activation barrier will dominate the surface reactions, while the second adsorption configuration may not be kinetically relevant.

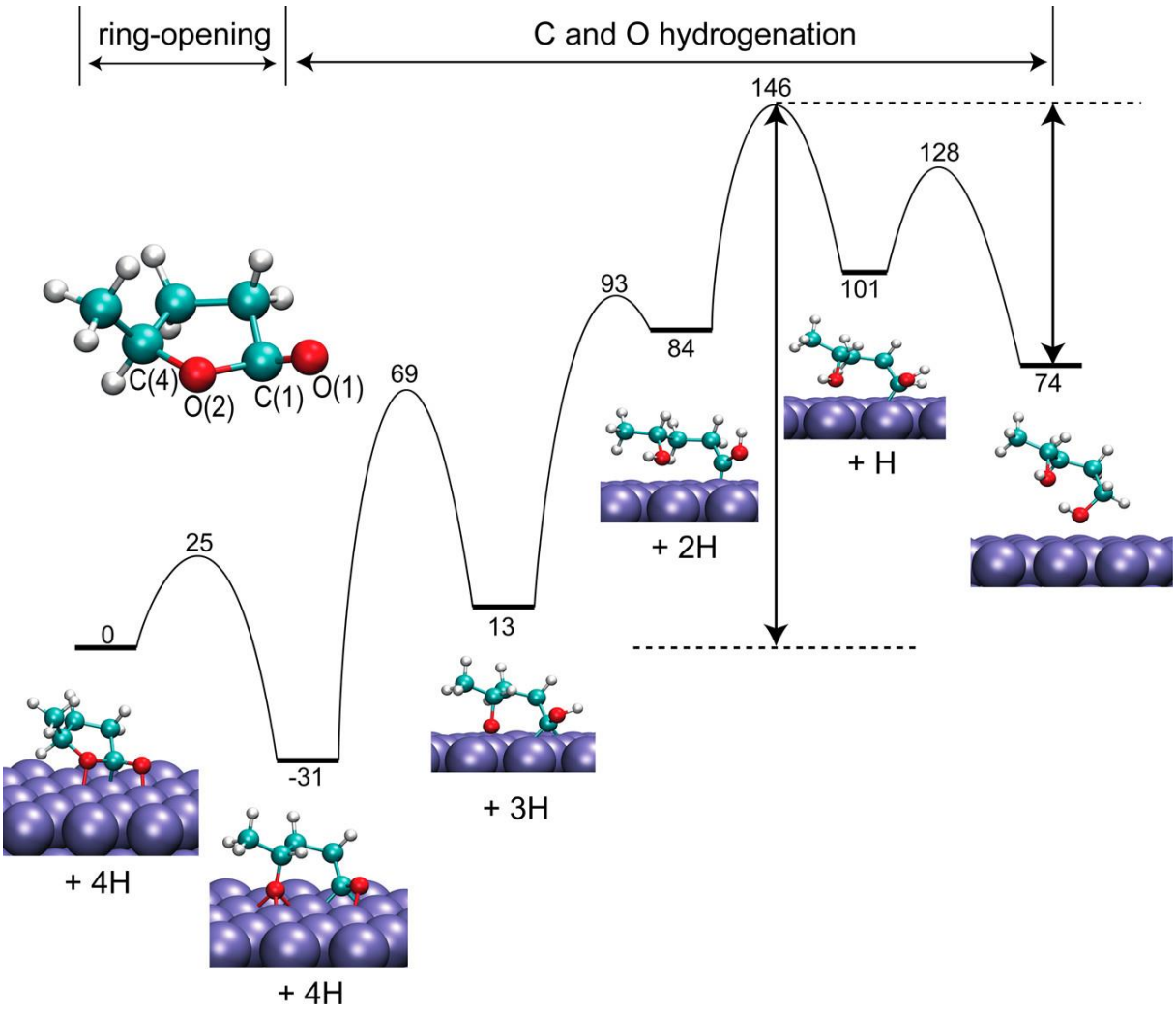

Figure 9 Energy profile calculations (kJ/mol) for the formation of 1,4-PDO from GVL. Structures of the initial, intermediate, and final states are shown. The two arrows indicate the apparent barriers for the forward and backward reactions

In order to understand the reaction steps that GVL can undergo based on the products, detailed step-by-step reaction pathways were developed. Figure 9 shows that GVL can undergo a ring-opening step, forming a surface-adsorbed acyl species. This exothermic ring-opening reaction (−31 kJ/mol) is driven by the strong Ru interaction to both carbon and oxygen,[128] which also drives ring-opening reactions of other heterocyclic aromatics such as furanics.[129] The combination of low energy barrier and exothermicity of this step suggest that adsorbed GVL molecules on Ru(0001) may undergo ring opening easily through the breaking of the C(1)–O(2)

bond. Alternatively, the GVL ring could open at the C(4)–O(2) bond. However, Rozenblit et al. has shown that ring opening of GVL through breaking the C(4)–O(2) bond has a much greater energy cost.(24) Moreover, the cleavage of the C(1)–O(2) bond gives a much better agreement with the product distribution found in varied experiments[121, 122] than the C(4)–O(2) cleavage.

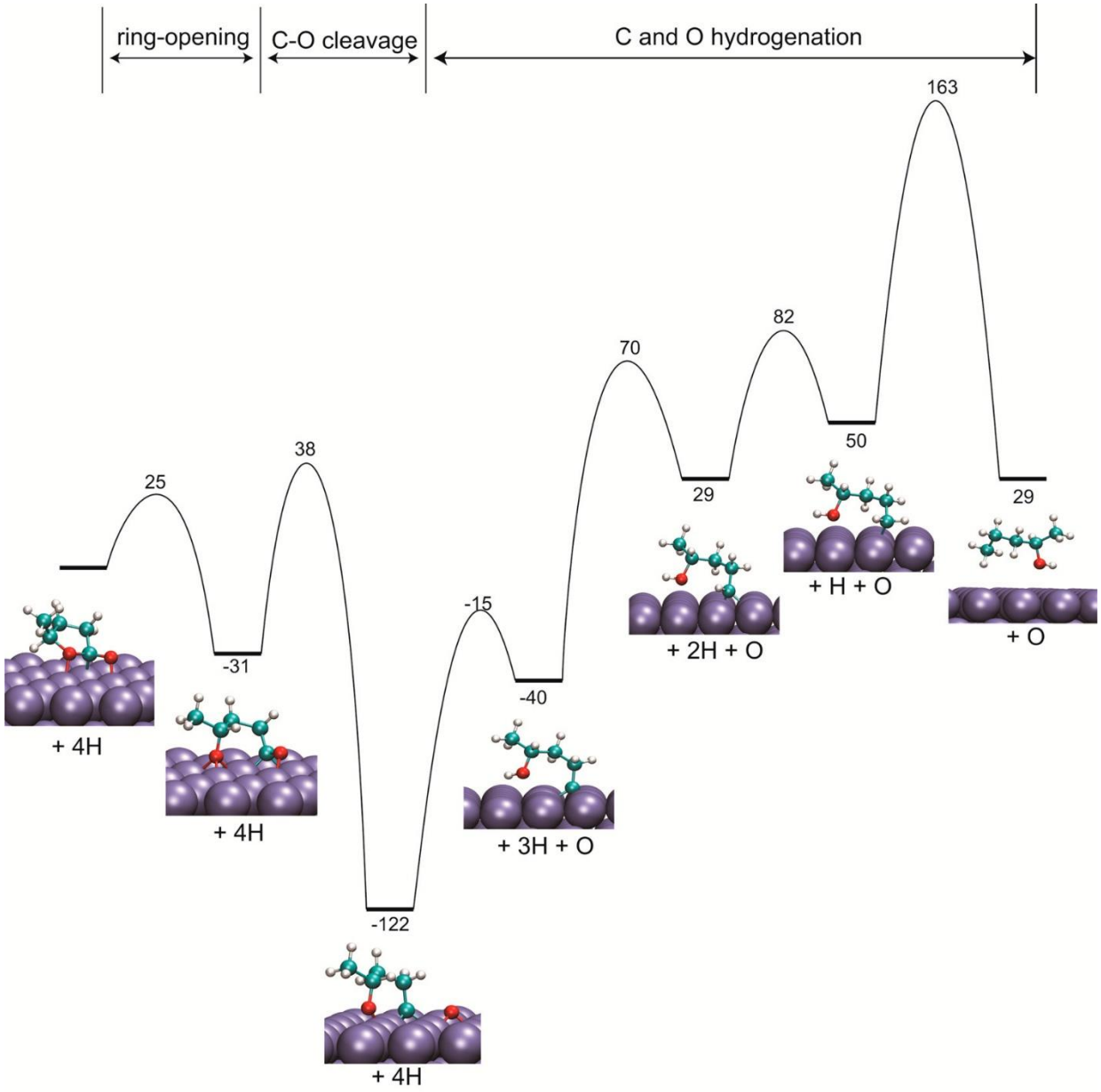

Figure 10 Energy profile calculations (kJ/mol) for the formation of 2-PeOH from GVL

This ring-opening reaction leads to an acyl intermediate, which can go through four sequential hydrogenation steps to yield 1,4-PDO. The subsequent steps for the formation of 1,4-PDO are the hydrogenation of the two O atoms, followed by two hydrogenation steps of the carbonyl carbon. The first hydrogenation step occurs at the carbonyl oxygen atom (O(1)) with a true energy barrier of 100 kJ/mol. Hydrogenation of the other oxygen atom (O(2)) as the first step was also considered, but calculations show a higher activation barrier for this route, because of the fact that O(1) is adsorbing on a top site of the Ru surface compared to the O(2) atom, which is adsorbed on a face-centered cubic (FCC) site. The reaction to form 1,4-PDO from GVL is endothermic with a reaction energy of 74 kJ/mol and an apparent barrier of 146 kJ/mol. The rate-limiting step is the hydrogenation step, because of the strong interaction between Ru and the unsaturated C and O atoms in the GVL ring-opening product,[128] which suggests that the formation of 1,4-PDO is very sensitive to the hydrogen coverage. High coverage of hydrogen may affect both the stability of the acyl intermediate, because of lateral interaction between adsorbates, and the activation barriers of the hydrogenation steps. This is consistent with a recent study on hydrogenation of furfural on Pd at different hydrogen coverages,[34] where it was shown that hydrogen coverage affects both adsorption energies of furfural and activation barriers for the hydrogenation steps. This result is supported by the enhanced yield measured experimentally when increasing H2 pressure.[122] The energy profile in Figure 9 also shows a moderate activation barrier for the reverse reaction, that is, dehydrogenation of the 1,4-PDO to form the ring-opening acyl intermediate. As discussed later in the text, this ring-opened GVL can lead to the formation of 2-BuOH and 2-PeOH. In other words, 2-BuOH and 2-PeOH may be formed either as a primary product from GVL or a secondary product via 1,4-PDO.

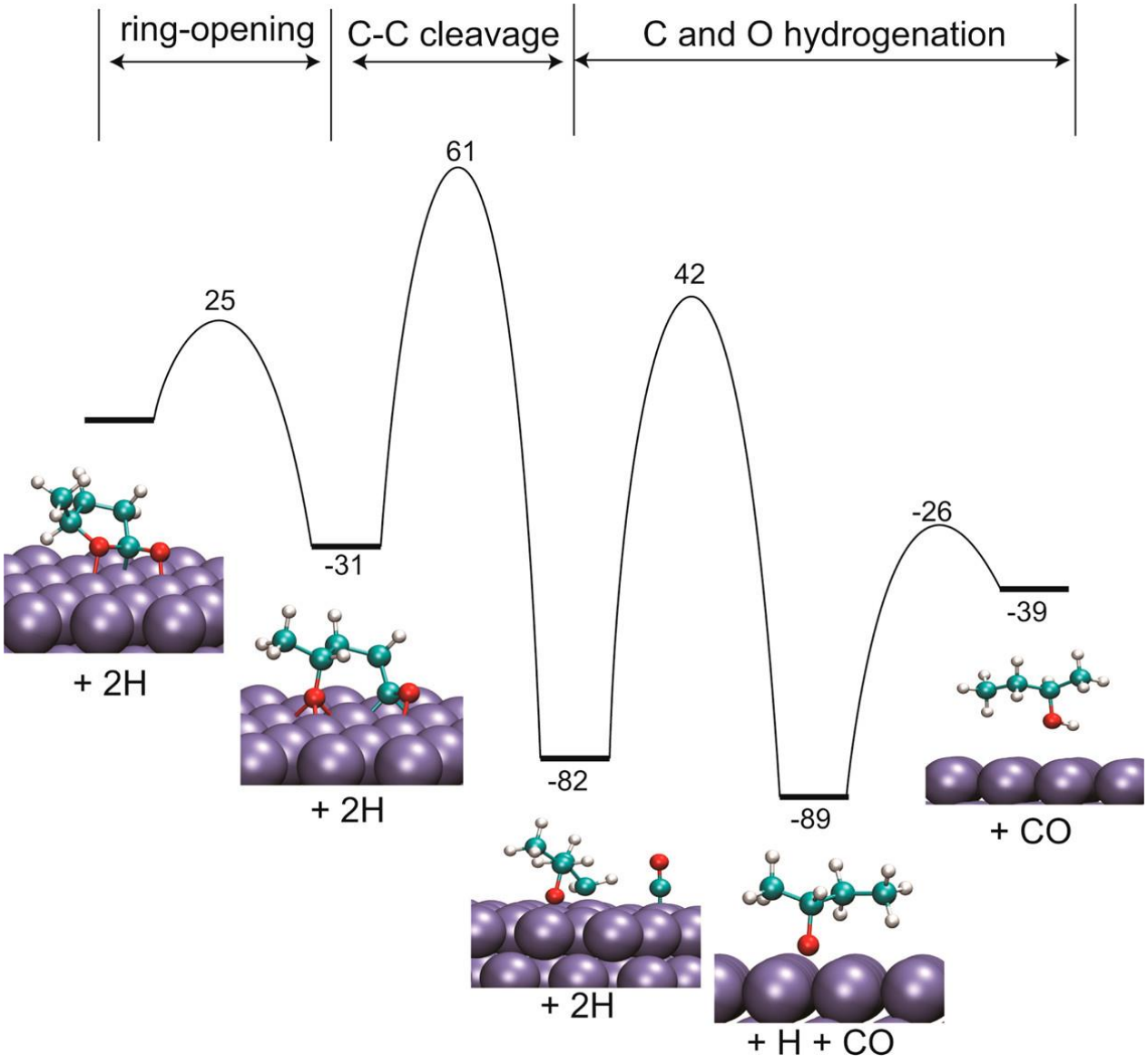

Figure 11 Energy profile calculations (kJ/mol) for the formation of 2-BuOH from GVL

The second pathway examined in this contribution is the formation of 2-PeOH. The first step in this reaction is the same formation of the ring-opened acyl intermediate CH3CH(O*)–(CH2)2–C*–O*. The subsequent step in this reaction is the direct deoxygenation of the intermediate to form CH3CH(O*)–(CH2)2–C* and an O atom adsorbed on the surface. This deoxygenation step has an energy barrier of 69 kJ/mol and is exothermic (91 kJ/mol). The exothermicity of this step is due to the strong interaction of the O atom with Ru (0001), and the newly formed α-carbon

strongly interacting with the Ru surface. The hydrogen-assisted deoxygenation has also been investigated in this case, where C(1)–O(1) bond breaking occurred after the hydrogenation of the O(1) oxygen. The calculated true activation barrier is 24 kJ/mol, much lower than that of the direct deoxygenation shown in Figure 10. However, as shown in Figure 9, the hydrogenation step of this the O(1) atom has an activation barrier of 100 kJ/mol, which is higher than that for direct deoxygenation (69 kJ/mol). Therefore, direct deoxygenation is more likely to happen rather than hydrogen-assisted deoxygenation. The subsequent steps in the formation of 2-PeOH are the hydrogenation of the second oxygen atom (O(2)), which has an energy barrier of 107 kJ/mol, followed by three hydrogenation steps of the unsaturated α-carbon, as shown in Figure 10. The rate-limiting step of these reactions is the third hydrogenation of the α-carbon to completely break the Ru–C bond. This overall reaction has apparent activation energy of 163 kJ/mol, with an energy cost of 29 kJ/mol.

Next, we examined the reaction path for the conversion of GVL to 2-BuOH. Figure 11 shows that this pathway involves a decarbonylation step of the acyl intermediate formed, as a result of GVL ring opening. Decarbonylation of CH3CH(O*)–(CH2)2–C*–O* to yield CH3CH(O*)–CH2–CH2* and carbon monoxide has an energy barrier of 92 kJ/mol and is exothermic (−51 kJ/mol). Once the CH3CH(O*)–CH2–CH2* intermediate is formed, hydrogenation of the oxygen atom and the α-carbon have true energy barriers of 124 and 63 kJ/mol, respectively. The rate-limiting step of forming 2-BuOH is thus the decarbonylation of the acyl intermediate. Indeed, Rozenblit et al. have shown strong inhibition effect for forming 2-BuOH when CO is introduced,[122] which supports the conclusion that the direct decarbonylation of the ring-opened GVL is rate-limiting.

Now we are in a position to compare all the reaction pathways. First, we note that the formation of 2-BuOH has the lowest apparent barrier (61 kJ/mol) and can be formed directly from GVL through a ring-opened acyl intermediate. This result is consistent with the experimental results showing that 2-BuOH is the most abundant product.(24) The above study also suggests that all products are primary and can be formed directly from the aforementioned acyl intermediate. Meanwhile, the moderate barrier for 1,4-PDO to form the same acyl intermediate (72 kJ/mol, as indicated in Figure 9 by an arrow) suggests that, once 1,4-PDO forms, it can easily convert to 2-BuOH and MTHF as well, which probably explains why the yield of 1,4-PDO is always very low.[121, 122] Instead, because of the large activation barrier, the formation of 2-PeOH should be very limited. Note that the DFT calculations reported here have been performed on clean metal surfaces under vacuum, while, in the experiments, reactions were run in the presence of a water solvent. It has been shown that the protic solvent may affect the reaction in complicated ways, such as via solvation of the surface species or via proton shuttling.[130-133] In the present case, the apparent barrier for the formation of 1,4-PDO and 2-PeOH may be overestimated in the calculations, because of the likely reduced barriers in water for the multiple hydrogenation steps involved along the reaction pathways. However, we expect that the formation of 2-BuOH may not be affected much by the water solvent, because, in this case, the rate-limiting step is decarbonylation rather than hydrogenation.

Because of the thermal stability of the acyl intermediate and large activation barrier for the hydrogenation, the Ru surface may be covered mostly by the acyl species under the reaction conditions.[122] We have also calculated the adsorption energies of GVL and all the products on the Ru surface, which is summarized in Table 2. The adsorption energies are rather similar, which may suggest competitive adsorption of these species on the surface. Particularly, because of the

large heat of adsorption on the Ru surface, 1,4-PDO may remain on the surface and undergo dehydrogenation to form other products, such as 2-BuOH, 2-PeOH, and 2-MTHF, which is supported by the experimental observation of 2-BuOH, 2-MTHF, and 2-PeOH when feeding 1,4-PDO.[122] The reaction of 1,4-PDO may proceed through dehydrogenation followed by decarbonylation and hydrogenolysis, which has been proposed for other alkanols under similar reaction conditions.[134]

	E_{ads} (kJ/mol)
GVL	−96
1,4-PDO	−113
2-PeOH	−107
2-BuOH	−98
2-MTHF	−98

Table 2 Adsorption Energy of GVL and All the Products

We do not present details of the formation of MTHF here, since previous experiments over a Ru catalyst have shown that MTHF is a secondary product[122] and can be obtained from 1,4-PDO.(22, 23) We have calculated the ring-closure reaction using the deoxygenated acyl species CH3CH(O*)–(CH2)2–C* in Figure 10 as the initial structure, and found a very high activation barrier of 318 kJ/mol for this ring-closure step, because of the fact that this ring closing requires the breaking of multiple C–Ru and O–Ru bonds. One possibility is that MTHF forms from CH3CH(O*)–(CH2)2–HC* through ring closing and hydrogenation, because the dehydrogenated C(1) carbon may weaken the interaction between C(1) and the Ru surface, leading to a reduced barrier for ring closure. This unsaturated alcohol intermediate, CH3CH(O*)–(CH2)2–HC*, can be formed by C–O hydrogenolysis of CH3CH(O*)–(CH2)2–HC*–OH; however, because of the smaller activation barrier for further dehydrogenation and the competing C–C cleavage for

decarbonylation to form CH3CH(O*)–(CH2)2 and sequentially hydrogenation, 2-BuOH may be more competitive, compared to the formation of MTHF. So MTHF may not be formed through a direct transformation from GVL. Instead, MTHF should be formed via ring closure of the same CH3CH(O*)–(CH2)2–HC* intermediate that is formed from the dehydrogenation and hydrogenolysis of 1,4-PDO, followed by a hydrogenation step, as described in Appendix B.

These results indicate that, if 1,4-PDO and MTHF were target molecules for commercial applications, one would design bimetallic catalysts that, at the same time, retain a high activity for ring opening, such as Ru, but promote the hydrogenation steps, such as Pt or Pd. Particularly for MTHF as a direct product from 1,4-PDO, one would promote the hydrogenolysis step to remove the terminating OH in 1,4-PDO and inhibit further dehydrogenation and decarbonylation. For the latter purpose, Cu may be a good component for a bimetallic catalyst, since it does not have strong interaction with the dehydrogenated C atoms. In addition, high hydrogen pressure may also inhibit the decarbonylation pathway, because of its high sensitivity to hydrogen, compared to the hydrogenolysis step.[134]

3.4 Conclusion

In this study, we report a detailed reaction mechanism study for the conversion of GVL on a ruthenium catalyst. Our calculations suggest that 1,4-PDO, 2-BuOH, and 2-PeOH can be formed through a common surface intermediate, but their rate-limiting step varies differently from hydrogenation for 1,4-PDO and 2-PeOH to decarbonylation for 2-BuOH, the latter has the smallest activation barrier. These results agree with previous experimental results reported in the literature and can be used as a guide for design of new catalysts with tailored reaction selectivity.

Acknowledgements

This contribution was identified by Hongliang Xin (Virginia Polytechnic Institute and State University) as the Best Presentation in the session “Computational Chemistry for Energy Application” of the 2016 ACS Fall National Meeting in Philadelphia, PA. The authors also appreciate valuable discussion with Drs. Tawan Sooknoi and Qiaohua Tan. The authors thank the support from U.S. Department of Energy, DOE/EPSCOR (Grant No. DESC0004600). The DFT calculations were performed at the National Energy Research Scientific Computing Center (NERSC) and the OU Supercomputing Center for Education & Research (OSCER) at the University of Oklahoma.

Chapter 4: Solvent-Mediated Charge Separation Drives Alternate Hydrogenation Path of Furanics in Liquid Water[*]

4.1 Introduction

Liquid-phase catalysis is of paramount importance in organic synthesis and chemical reformation[135-138]. For example, utilization of water/oil biphasic systems has allowed simultaneous separation of water- and oil-soluble products, while the catalytic reaction takes place at the water/oil interface[139]. However, the effects of the condensed liquid phase on the catalytic activity and selectivity are often not well understood. The presence of a dense surrounding medium may have multiple and distinct effects in these reactions, in addition to the well-known dissolution, heat transfer and heat sink effects, or the so-called cage effect.[140] In fact, it has been suggested that in addition to these conventional effects, solvents can change the kinetics of the reaction in cases in which the rate-determining step involves a solvated transition state[130, 131, 141]. Additionally, in aqueous solutions, water may directly participate in the reaction, as proposed for the case of water-assisted activation of CO[133] and O_2[142, 143] as well as for the enol/keto tautomerization[144]. In most previous studies, the solvent effects have been manifested indirectly by changes in reaction rates or selectivity[130, 131, 133, 142-144]. Here, we provide combined evidence from both measured reaction orders and free energy calculations for a predominant reaction pathway occurring during hydrogenation of furfural – a conjugated oxygenate – that includes a solution-mediated elementary step (Figure 1).

Furfural is an important platform chemical, produced from pyrolysis of biomass at moderate temperature by dehydration of xylose[114, 145, 146]. Hydrogenation of furfural produces furfuryl

[*] *Zhao, Z., et al., Solvent-mediated charge separation drives alternative hydrogenation path of furanics in liquid water. Nature Catalysis, 2019.*

alcohol (FOL), tetrahydrofurfural (THFAL) and tetrahydrofurfuryl alcohol (THFOL), as shown in Figure 2a. Further, metal-catalyzed hydrodeoxygenation of FOL produces meth furan (MF) [147, 148] while acid-catalyzed hydrolysis of FOL results in levulinic acid[131, 149]. All of these have potential industrial relevance. FOL is widely used in the manufacture of resins and fragrances[105], while both methyl furan (MF) and levulinic acid (LA) are desirable chemical building blocks in biorefineries[150].

Controlling the catalytic selectivity of furfural hydrogenation towards FOL represents a challenge for rational catalyst design[151-155]. Sitthisa *et al.* [36, 147, 156] showed that the hydrogenation selectivity in the vapor phase is dictated by the adsorption configuration of furfural on the metal surface. That is, a strong interaction between the furanyl ring and the Pd or Ni surface leads to the formation of furan, while a tilted adsorption configuration on the group VIII metals through the carbonyl group results in a high selectivity to FOL. Liquid-phase catalysis provides another option for tuning the selectivity. Previous experiments in the liquid phase, particularly in polar solvents[157-159], over supported single metal[158-161] and multi-metallic metal[157, 158, 162, 163] generally showed high yields of FOL. However, the underlying mechanism of this reaction in the liquid phase remains elusive[164].

Here, we provide insight into the solvent effects in furfural hydrogenation, derived from combined experimental and computational studies. The studies include a comparison of catalytic activity and selectivity in different solvents over a supported Pd catalyst under different H_2 pressures and free energy calculations of the reaction profile based on density functional theory (DFT). We conclude that the water solvent has multiple distinct effects that may greatly influence the catalytic reaction. In particular, we find that hydrogen can be uptaken as a proton through surface charge separation and transferred by water, leading to a reduced activation barrier for

hydrogenation of the carbonyl group, and that while hydrogenation of the C=O bonds involve predominantly a solution-mediated path, hydrogenation of the C=C bond is dominated by the surface reaction, due to the hydrophobic nature of the C atoms and the absence of H-bonded channels.

4.2 Methods

Experimental methods

Sample characterization. SEM characterization was performed with a Zeis Neon 40 EsB operated with an accelerating voltage of 5 keV, equipped with field emission and INCA Energy 250 Energy Dispersive X-ray (EDX) Microanalysis detector. EDX was used to map the Pd catalyst particles supported on the alumina. The surface metal dispersion of 1% Pd/α-Al2O3 and 2% Pd/α-Al2O3 intermediate catalysts was examined for the effectiveness of the sequential incipient wetness. For TEM characterization, a JEOL 200FX operated with an accelerating voltage of 200 kV and equipped with a LaB6 filament was used. The TEM images were used to determine the average particle size and size distribution of Pd particles. The particles were measured using ImageJ software and the particle diameter distributions were analyzed by histogram for average particle diameter calculation.

Measurement of the catalytic activity. The liquid phase furfural hydrogenation reactions were carried out in a total volume of 300 mL high-temperature and high-pressure Parr Batch stirred reactor (Series 4564). 90 mL of solvent and a certain amount of catalyst were loaded in the reactor before the reaction. N2 was purged into the whole reaction system to vent the air, followed by H2. The catalyst was reduced in the absence of reactant under 0.69 Mpa (100 psi) in H2 and at 100°C for 1 hour. The reactor was cooled down to 40°C. Then, additional 30 mL of solvent containing reactant was injected into the reactor until pressure reached 5.52 Mpa (800 psi), holding the

temperature at 40°C and stirring at 500 RPM. This moment is taking as the starting point of reaction time. The H2 inlet valve was kept open to maintain the constant pressure.

The liquid product was filtered and analyzed by gas chromatography. Shimadzu GCMS-QP2010S equipped with a Zebron ZB-1701 column was used for identification of products in the liquid mixture. Agilent 7890B GC-FID equipped with a Zebron ZB-WAXplus column was used for quantification of the individual product. Conversion and yields toward each product are defined as follows:

Solvents used in the study were classified as non-polar and protic polar. Non-polar solvent was cyclohexane (99.5%, Sigma-Aldrich). Protic solvent was purified deionized water. Reactant furfural (FAL, 99%, Sigma-Aldrich) was distillated in the N2 flow before use.

$$Conversion\ x\% = \frac{mole\ of\ reactant\ reacted}{mole\ of\ reactant\ fed} \times 100\% \qquad \text{(Equation 1)}$$

$$Yield\ y\% = \frac{mole\ of\ product\ i\ obtained}{mole\ of\ reactant\ fed} \times 100\% \qquad \text{(Equation 2)}$$

Computational methods

The Pd (111) surface was modelled using a (4×4) supercell. Each supercell contained repeated slabs with four metal layers separated by an 18 Å vacuum region. The bottom two layers of Pd have been fixed at their bulk positions while the top two layers were fully relaxed. A larger (6×6) supercell has been checked and no significant change has been found. A number of water molecules were chosen to fill the vacuum region above the metal slab to make the density of water approximately the same as that of liquid water at the standard conditions. The density functional theory (DFT) calculations and ab initio molecular dynamics (AIMD) simulations were carried out using the VASP package[91]. The Perdew-Burke-Ernzerhof generalized gradient approximation

exchange-correlation potential (PBE-GGA)[92] was used, and the electron-core interactions were treated in the projector augmented wave (PAW) method[93, 94]. Structures have been optimized until the atomic forces were smaller than 0.02 eV Å-1 with a kinetic cut off energy of 400 eV. We tried to increase the cut off energy to 450 eV and find insignificant difference of reaction energy and activation barrier. The van der Waals interactions were taken into account using DFT-D3 semi-empirical method[165]. Reaction pathways and the associated barriers were determined with the Climbing Image Nudged Elastic Band method[125, 126] and the dimer method[166]. The surface Brillouin zone was sampled with single k point at Gamma for the AIMD simulations and NEB and dimer calculations for the reaction profile at the solid/liquid interface. For simulations of the water-Pd (111) interface, AIMD simulations at finite temperatures (see text) were performed in canonical ensembles. The time step was set to 0.5 fs. After thermal equilibrium has been reached, multiple snapshots were taken and optimized for further DFT calculations. For example, 10 snapshots each for furfural positioned at the water/Pd interface and in the water bulk were optimized to compare the total energy difference.

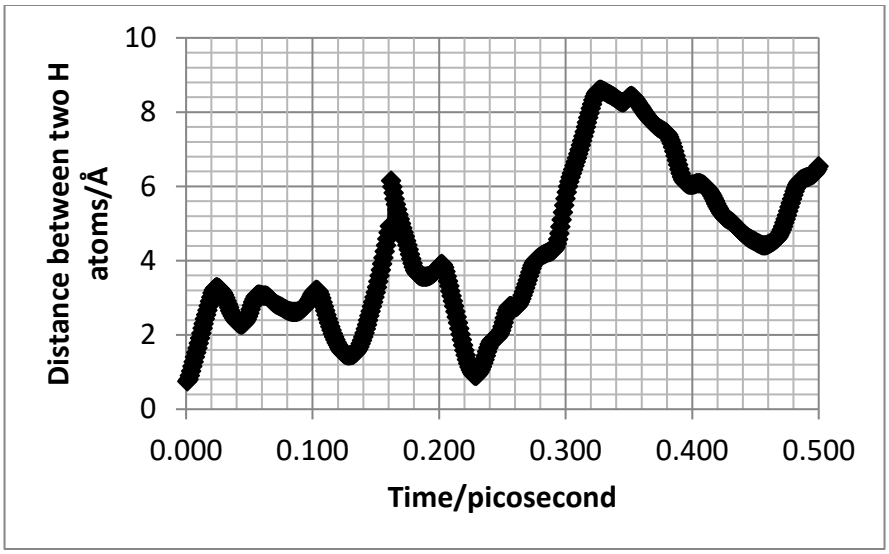

Figure 12. AIMD simulation of dissociation of H_2 on Pd (111). The change of the distance between two H atoms over time, obtained from ab initio MD simulations at 493 K. The two hydrogen atoms were initially in the form of H_2.

Ab initio Molecular Dynamics (AIMD) Simulations and DFT calculations. Figure 12 shows the change of the distance between the two hydrogen atoms over time when the temperature is 493 K. Simulation results at other temperatures including 373 K and 300 K show similar behavior for the change of the H-H distance. As shown in Figure 13, the initial distance between the two hydrogen atoms is 0.75 Å, the equilibrium bond length of H2. It is observed that the distance increases so rapidly that only after 0.01 ps, the molecule is essentially dissociated. AIMD simulations show that the two separate atoms diffuse on Pd (111) with the FCC site the most stable, and that the bridge and HCP sites are less stable. Most of time, the atoms stay near FCC sites while they diffuse from one FCC site to another. Occasionally, the two hydrogen atoms combine and return to the form of H2, but the resulted H2 dissociates rapidly again. Therefore, in the following calculations and simulations, we assume that hydrogen on Pd (111) is in the form of atoms with the FCC site as its preferred bonding site. Figure 13 shows results in the AIMD simulations for furfural dissolved in water and adsorbed at the Pd/water interface. The total energies start to

equilibrium after 10 ps. We picked up 10 snapshots after 12 ps, assuming that the thermal equilibrium has been reached, and optimized the structures using PBE-D3. The average energy of the 10 structures of water adsorbed at the Pd/water surface is 17 kJ/mol less negative (less stable) than the one of furfural dissolved in water.

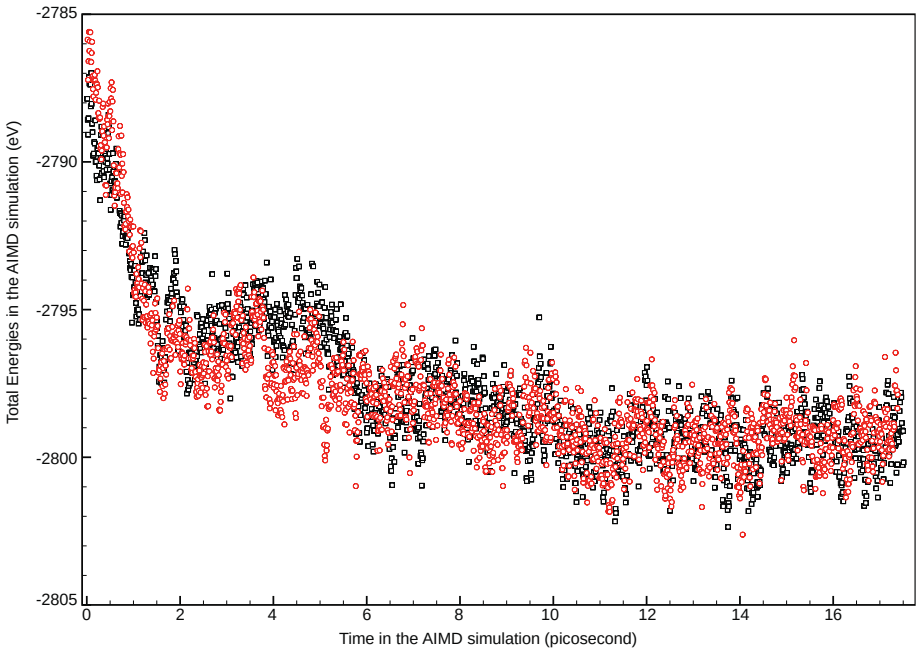

Figure 13. ***AIMD simulations of furfural at the water/Pd interface.*** *Comparison of AIMD energy of FAL at two different locations in the water/Pd system at the reaction temperature (320 K), that is, FAL positioned at the interface (red), and the FAL positioned in the water layer (black).*

DFT Calculations with Organic Solvent. Note We didn't include the organic solvent explicitly in the calculations shown in Figure 19 because of two reasons: (1) it is very challenging to model an organic solvent quantum mechanically due to the computational cost and the accuracy issue to treat the weak intermolecular interaction; (2) more importantly, previous seminal work done by Vannice et al.[167] performed hydrogenation of an unsaturated oxygenate in eight different solvents, including cyclohexane, and showed that the kinetics could be well modeled with a rate equation based on a standard Langmuir–Hinshelwood (LH) mechanism. The rate equation

was the same as a typical LH one for a gas-phase reaction except that it included the competitive adsorption of the solvent. Vannice et al. [167] was able to show that the reaction order and intrinsic reaction barrier could be the same among all eight organic solvents, which should be the same as a gas-phase reaction, since everything else in the rate equation is essentially the same as in a gas-phase LH model. In fact, Szmant et al. found a similar trend when they investigated oxidation of thiols in less polar solvents[168], though they didn't model the kinetics in details.

Enthalpy corrections. Temperature-dependent enthalpy was calculated using DFT calculated electronic energy at 0 K and the harmonic approximation for zero-point energy and heat capacity which accounts for the difference in temperature between DFT calculated energies at $0\ K$ and the actual experiment temperature of 313.15 K.

where k_B is the Boltzmann constant, h the plank's constant, and v_i is the vibrational frequency obtained based on DFT calculations. All the vibrational frequencies from DFT were used to evaluate the zero-point energy and thermal capacity.

$$H(T) = E_{elec} + E_{ZPE} + \int_{0K}^{T} C_v dT \qquad \text{(Equation 3)}$$

$$E_{ZPE} = \frac{1}{2}\sum_{i=0}^{\#DOF} hv_i \qquad \text{(Equation 4)}$$

$$\int_{0K}^{T} C_v dT = \sum_{i=0}^{\#DOF} \frac{hv_i}{e^{hv_i/k_BT} - 1} \qquad \text{(Equation 5)}$$

Entropy calculation. Vibrational entropy contribution was calculated using the harmonic normal mode approximation

Translational and rotational contributions to entropy for all surface reactions were assumed to be constant. On the other hand, gas phase adsorbate species (furfural and furfuryl alcohol) were assumed to retain $\sim\frac{2}{3}$ of gas phase entropy upon adsorption, and then remain constant over the elementary steps of surface reactions. This assumption was based on previous work on adsorbed alkanes[169]. The Gibbs free energy change was calculated based on enthalpy and entropy changes

$$S\,(T) = k_B \sum_{i=0}^{\#DOF} \frac{h\nu_i}{k_B T\left(e^{h\nu_i/k_B T} - 1\right)} - \ln\left(1 - e^{-h\nu_i/k_B T}\right) \qquad \text{(Equation 6)}$$

4.3 Kinetic analysis

$$\Delta G = \Delta H(T) - T * \Delta S(T) \qquad \text{(Equation 7)}$$

To ensure the collection of reliable kinetic data, mass transfer tests were conducted to ensure no transport limitations of hydrogen transfer from gas phase to liquid phase and the reactant from bulk to the catalyst surface. Heat transport limitations in liquid-phase reactions are commonly not dominant due to the high heat capacities and good thermal conductivities compared to gas-phase reactions[164]. To ensure the reaction was carried out with no mass transfer limitations, the stirring speed was increased until conversion no longer changed. These tests were performed for the furfural hydrogenation reaction. Water was chosen to be the solvent due to the highest hydrogenation activity being shown, which may exhibit the mass transfer resistance from the bulk liquid phase to the catalyst surface. 0.1 M of furfural was reacted over 0.1g of 3%Pd/α-Al_2O_3 for 0.8h at 425 rpm and 600 rpm, respectively.

Chambers and Boudart[170] pointed out this test may fail in laboratory reactors, because the stirring speed is still at low Reynolds number where the mass transfer coefficient is insensitive with increase of the stirring speed. In order to further prove that the reactions are in the kinetic

regime, the widely used criteria in three phases stirring reactors[171-173] were used. Proposed by Ramachandran and Chaudhari[174], the criteria define the ratio of observed rate to the maximum rate. α1 describes the gas-liquid mass transfer ratio, and α2 describes the liquid-solid mass transfer ratio. The criteria are shown as followed:

where k_{lab} is the gas-liquid mass transfer coefficient, CA* is the saturation solubility that is calculated by Henry's Law, ks is the effective diffusivity, and ap is the catalyst external surface area. The calculation gave the values for α1 is 0.04 and α2 is 2.035×10^{-5}, both smaller than 0.1, showing the kinetic data acquired were in the absence of external mass transfer limitation.

$$\alpha_1 = \frac{(r_A)_{obs}}{k_l a_b C_A^*} < 0.1 \qquad \text{(Equation 8)}$$

$$\alpha_2 = \frac{r_{obs}}{k_s a_p C_A^*} < 0.1 \qquad \text{(Equation 9)}$$

In addition, the low surface area and the extremely low pore volume of the catalyst support diminish the presence of intra-particle mass transfer limitation. The reactions in the study were conducted under 425 rpm in order to provide a moderate agitation so that the thermal couple is fully immersed in the liquid and the catalyst wouldn't splash.

Rate Equation. We assume the organic molecules and hydrogen are adsorbed on different sites based on the literature as well as our previous work of kinetic fitting. The work by Nakagawa[175] showed that furfural hydrogenation rate over Pd/SiO2 increases with H2 pressure, while the furfural concentration change results a negligible change in reaction rate. H2 doesn't compete active sites with other organic molecules. Moreover, in the kinetic study using Pt/C as the catalyst, dual site kinetic model provided the best fit of experimental data [160]. Actually, most modern reviews on hydrogenation reactions have concluded that the most appropriate models consider adsorption of H and reactants on separate (non-competing) sites [164, 176, 177]. In the following,

the hydrogenation kinetic models of furfural hydrogenation to furfuryl alcohol are developed based on the Langmuir-Hinshelwood surface mechanism, which involves adsorption, surface reaction and desorption as follows:

Where k_i is rate constant, and S represents empty Pd sites.

$$H_2^g \leftrightarrow H_2^l \quad \text{(Equation 10)}$$

$$H_2^l + 2S \overset{k_1}{\leftrightarrow} 2HS \quad \text{(Equation 11)}$$

$$FAL + S \overset{k_2}{\leftrightarrow} FALS \quad \text{(Equation 12)}$$

$$FALS + HS \overset{k_3}{\rightarrow} FALHS + S \quad \text{(Equation 13)}$$

$$FALHS + HS \overset{k_4}{\rightarrow} FOLS + S \quad \text{(Equation 14)}$$

$$FOLS \overset{k_5}{\leftrightarrow} FOL + S \quad \text{(Equation 15)}$$

Depending on whether the first or the second hydrogenation is the rate-determining step, the initial reaction rate when final product is negligible can be expressed as:

Where K_i is adsorption constant. Equation 16 represents the rate when the first hydrogenation of furfural is the rate-determining step, and Equation 17 is the rate expression when the second hydrogenation is the rate-determining step. When the reactions are carried out under low H_2 pressure, the $\sqrt{P_{H_2}K_{H_2}}$ term becomes insignificant; the $1 + \sqrt{P_{H_2}K_{H_2}}$ term in the denominator is approximate to 1. Therefore, the reaction order based on H_2 at low H_2 pressure is half order for Eq. (10) and first order for Eq. (11), respectively. Similarly, the hydrogenation of furfural to tetrahydrofurfural generates the same reaction order for both surface mechanisms. The difference in reaction order based on the H_2 pressure leads to distinguished rate-determining steps during hydrogenation. Furfural hydrogenation is further investigated in cyclohexane and water.

$$r = \frac{k_3 K_{FAL} C_{FAL} \sqrt{P_{H_2} K_{H_2}}}{(1 + K_{FAL} C_{FAL})(1 + \sqrt{P_{H_2} K_{H_2}})} \quad \text{(Equation 16)}$$

$$r = \frac{k_4 K_{FALS} K_{FAL} C_{FAL} (P_{H_2} K_{H_2})}{(1 + K_{FAL} C_{FAL} + K_{FALS} K_{FAL} C_{FAL} \sqrt{P_{H_2} K_{H_2}})(1 + \sqrt{P_{H_2} K_{H_2}})} \quad \text{(Equation 17)}$$

Maximum rate analysis. In order to determine the most likely pathway based on the free energy calculations, the maximum rate of each elementary step in the mechanism was calculated with the assumption that this step is the rate-limiting one while all other steps are equilibrated.[178] The partial pressures and concentrations of reactants and products and reaction temperature were set based on experimental conditions.

The 2-site elementary steps for furfural hydrogenation on Pd (111) are the same as Equations 10-15 described above. The maximum rate of the elementary steps is then calculated according to the following equations:

$$r_{1,max} = \frac{k_B T}{h} e^{\left(-\Delta G_1^{\ddagger} / k_B T\right)} p_{H_2} \quad \text{(Equation 18)}$$

$$r_{2,max} = \frac{k_B T}{h} e^{\left(-\Delta G_2^{\ddagger} / k_B T\right)} p_{FAL} \quad \text{(Equation 19)}$$

$$r_{3,max} = \frac{k_B T}{h} e^{\left((-\Delta G_3^{\ddagger} - \Delta G_1 - \Delta G_2) / k_B T\right)} p_{FAL} p_{H_2}^{0.5} \quad \text{(Equation 20)}$$

$$r_{4,max} = \frac{k_B T}{h} e^{\left(\left(-\Delta G_4^{\ddagger} - \Delta G_1 - \Delta G_2 - \Delta G_3\right) / k_B T\right)} p_{FAL} p_{H_2} \quad \text{(Equation 21)}$$

$$r_{5,max} = \frac{k_B T}{h} e^{\left(\left(-\Delta G_5^{\ddagger} - \Delta G_1 - \Delta G_2 - \Delta G_3 - \Delta G_4\right) / k_B T\right)} p_{FAL} p_{H_2} \quad \text{(Equation 22)}$$

with $\Delta G_i^{\ddagger}$ indicating the transition state Gibbs free energy change and ΔG_i the reaction Gibbs free energy change. All the rates were evaluated with respect to the gas phase as discussed in the

literature[178]. The rate is not directly compared to the experiments but used to compare different elementary steps to identify the RLS.

Resistance. Datta et al. drew an electrical analogy of the sequence of steps involved in a chemical reaction to a sequence of resistors[179]. Resistance for each elementary step assuming it is rate limiting is defined based on Ohm's law:

$$R_{i,max} = \frac{1}{r_{i,max}} \quad \text{(Equation 23)}$$

where R_i is the resistance of step i to the overall reaction.

The resistance calculation is used to illustrate the parallel pathways in the reaction network. The analysis was performed based on a few assumptions (see below), particularly the adsorption entropy and entropy of furfural and furfuryl alcohol in water.

When calculating the maximum rate, we used the following parameters:

1. Pre-exponential factor = k_BT/h, where k_B is the Boltzmann constant, T the reaction temperature and h Planck's constant.
2. The adsorption energy of reactants and the activation barriers were adopted from Figure 16 in the main text.
3. Furfural adsorption energy in the gas phase was taken from experimental TPD values of -0.98 ± 0.20 eV [151, 152]. We tried different values from -0.5 to -2.0 eV, and the conclusion of reaction order in the maximum rate analysis is insensitive to the exact values of the furfural adsorption. Experimentally furfural desorption occurs around 260 K and is complete by 460 K indicating different adsorption states on the Pd surface.[152] In Table 3, we only showed the values using -0.8 eV – the lower bound of the range – as the furfural adsorption energy.
4. FOL adsorption in gas phase was taken from experimental TPD values of -0.70 ± 0.14 eV [151, 152]. Its adsorption at the water/Pd interface was assumed to be thermal neutral. The conclusion of reaction order holds true when varying these values.

5. Adsorption of furfural and FOL in water is difficult to be obtained experimentally. We obtained 0.18 eV for furfural adsorption by comparing overall 20 snapshots from two different AIMD simulations – furfural adsorbed at the water/Pd interface and in the water phase (Figure 13). To be consistent in the maximum rate analysis, we assume the adsorption enthalpy is zero for both furfural and FOL in water, and thus, the adsorption/desorption is driven by entropy. Again, varying the adsorption enthalpies don't change conclusion of the reaction orders with respect to H_2 pressure.
6. For entropy change of both furfural and FOL upon adsorption, we assumed that the adsorbed molecules retain 2/3 of the gas phase entropies[169].

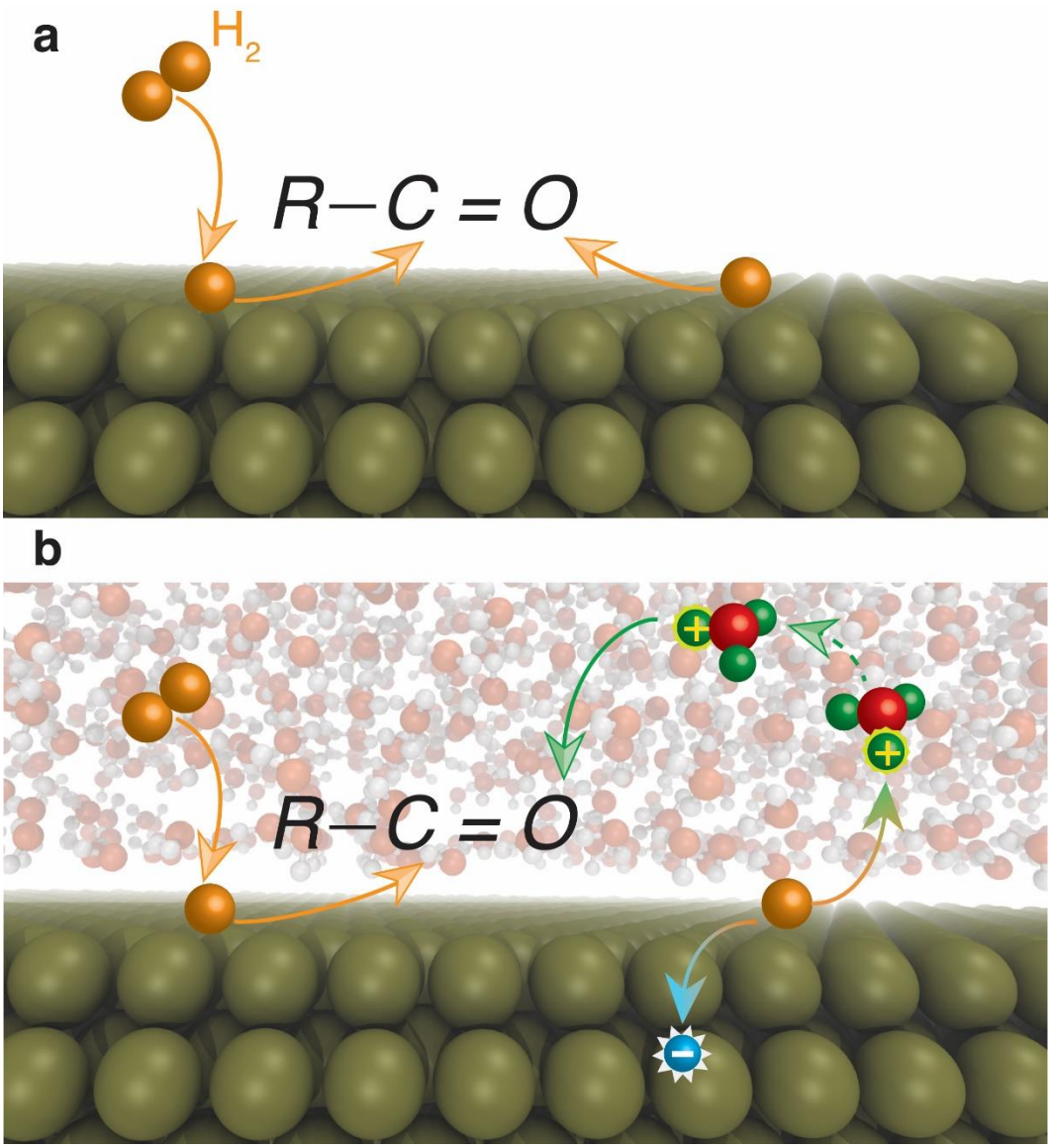

Figure 14. Schematic for reaction path in liquid-phase catalysis. Presence of a solvent in (b) provides an alternate reaction path as compared to gas-phase reactions (a). The additional degree freedom of the reaction may be determined by the rate of surface charge separation for formation of protons in the solvent.

4.4 Results and discussion

Solvent effect on selectivity. The Pd catalyst was prepared on an α-Al2O3 substrate through a series of sequential incipient wetness impregnation steps. Figure 15 shows a TEM image of the 3% Pd/α-Al2O3 sample. A histogram of Pd particle diameter distribution resulting from counting 100 particles is included. The calculated volume-weighted averaged particle size is 4.4 nm. Figure

15c shows the FAL conversion and product yields in two different solvents (cyclohexane and water). Cyclohexane was chosen to represent the organic solution because of its moderate miscibility with furfural. When using decalin as the solvent a fast catalyst deactivation was observed, probably due to the low solubility of furfural in this solvent that enhanced deposition on the catalyst surface and polymerization of reactants and reaction intermediates. In agreement with previous studies[175], the only products observed, in both cyclohexane and water media, were FOL, THFAL and THFOL. The average carbon balance in all the runs was around 95%. Figure 15c also shows that THFAL is the main product in cyclohexane, suggesting that furanyl ring hydrogenation (Figure 15a) is preferred in this solvent. Distinctly, when the reaction was carried out in water, a protic polar solvent, the furfural conversion was twice as high as in cyclohexane (Figure 15c). Moreover, a dramatic difference in selectivity was observed. That is, at comparable conversion levels, while in cyclohexane the dominant product was THFAL, the main product observed in water was FOL, which is generated via hydrogenation of the carbonyl group, rather than the furanyl ring.

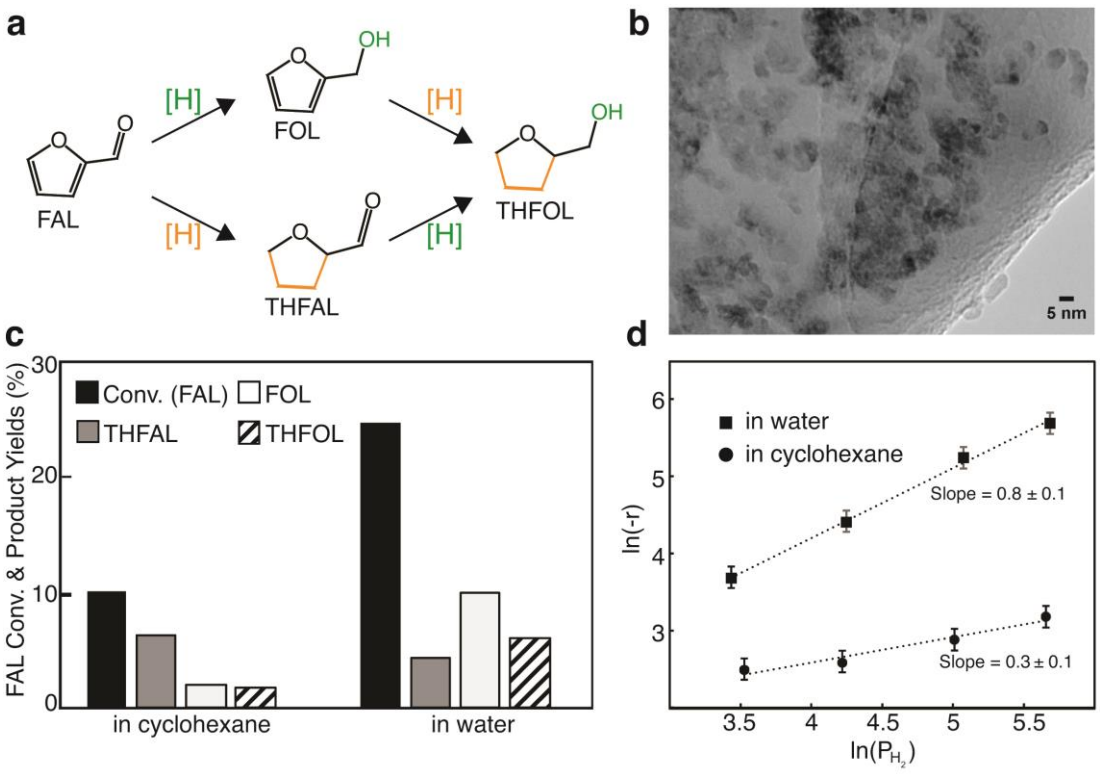

Figure 15. Catalyst characterization and test. (a) Possible reaction paths and products. (b) TEM image of the 3% Pd/α-Al2O3 catalyst. (c) FAL hydrogenation conversion and products yields in different solvents. Reaction conditions: initial concentration of FAL is 0.1 M, T = 40°C, P = 5.52 MPa, catalyst amount = 250 mg 3% Pd/α-Al2O3, reaction time = 0.8 h. (d) Different reaction orders with respect to the partial pressure of H2 in water and cyclohexane. The error bar was determined by two reactions conducted under the same conditions.

Furthermore, Figure 15d shows that, at similar overall furfural conversion (~10%), the reaction order with respect to the pressure of H2 was about 0.3 in cyclohexane and 0.8 in water, respectively, indicating different rate-limiting steps in the two solvents. That is, hydrogenation of the C=O requires two sequential steps (hydrogenation of the C and the O in the carbonyl group, Figure 15a). If, after eliminating the mass transport limitation, the first hydrogenation is rate limiting, the reaction order in H2 should be approximately half at low H2 pressure (see Equation 17 derived based on a two-site model[164, 177]). By contrast, if the second hydrogenation is rate limiting, the reaction rate should be first order in H2 pressure (that is, one half for each step, as shown in Equation 17). The different reaction orders indicate that, indeed, the rate-limiting steps for furfural

hydrogenation are different in water and in cyclohexane. Furthermore, to emphasize the role of water, we conducted reactions in deuterated water (D2O) under the same reaction conditions. However, we found that a fast H/D exchange between the product alcohol and the solvent made it challenging to unambiguously demonstrate the role of water.

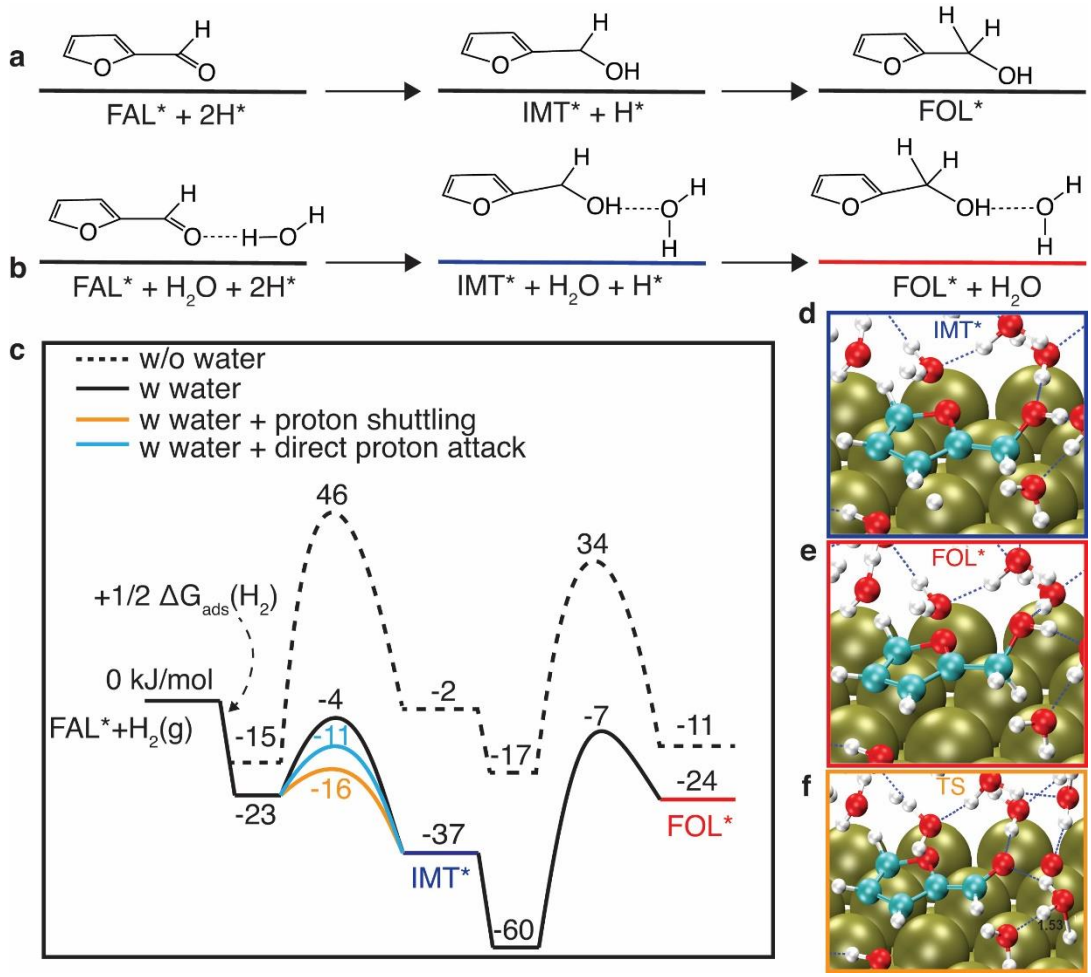

Figure 16.. Free energy calculations of hydrogenation of furfural. (a) Schematic reaction path in the vapor phase. (b) Reaction path in water; water helps the surface charge separation to form solvated protons in water and electrons left in the metal reservoir, both of which reach the adsorbed reactants simultaneously. (c) Calculated energy profile of hydrogenation on Pd in the gas phase (dotted black) and in the aqueous phase when water does not directly participate in the reaction (filled black) and when water helps the surface charge separation (blue and orange). Note for the latter two, the second step of the reaction – C hydrogenation – is the same. (d-f) Structures of the surface bound species (IMT and FOL*) and the first transition state (TS) in water.*

Ab Initio molecular dynamics simulations of furfural in an explicit water solvent. We explored these solvent effects by using computational calculations. We first performed ab initio molecular dynamics (AIMD) simulations for H_2 on a Pd (111) surface at various temperatures. As expected, we found that at the operating temperatures of typical catalytic reactions H2 rapidly dissociates on Pd (111) (Figure 12). In the absence of liquid water, we found that, in agreement with previous calculations[151], the most stable adsorption configuration of FAL on Pd(111) is one with the furanyl ring lying parallel to the surface. Similarly, at the water-Pd (111) interface, we observed that furfural adopts a configuration with the furanyl ring almost parallel to the surface, but with the aldehyde group tilted up slightly, towards the water phase. That is, the interaction with water in the close proximity lifts the oxygen from the surface, weakening the interaction with the metal surface, which may facilitate its hydrogenation (see below)[180]. The AIMD energy profile at the reaction temperature of furfural in both water and at the water/Pd interface is shown in Figure 13. By analyzing the snapshots from the AIMD simulations Figure 13, we find that furfural in water is about 17 kJ/mol more stable than when positioned at the water/Pd interface, indicating that partition of furfural on the Pd surface is comparable to solvation in water.

Free energy calculations of different hydrogenation routes. Figure 16 shows the calculated reaction pathways of furfural hydrogenation with and without liquid water. In these calculations, the hydrogen atoms adsorbed on the surface directly participate in hydrogenation (Figure 16a) we find that the sequential hydrogenation of the O atom followed by the C atom in the carbonyl group has an overall free energy barrier of 46 kJ/mol (Figure 16c). The opposite sequence, that is, C first and O second, has a much higher activation barrier (Appendix C). Therefore, in the ensuing discussion, we only focus on the former reaction pathway, with O and then C hydrogenated sequentially since the barrier for the latter is higher.

In liquid water, the overall activation barrier decreases significantly (Figure 16c). The surface reaction becomes more exothermic in water than on a clean Pd (111) surface. This favored energetics results from the stabilization of the reaction intermediate (IMT) and the surface bound FOL by the water phase. Figure 16d and 16e show that neighboring water molecules form H bonds with the intermediate and the product FOL. Because of this stabilization effect of the IMT, the energy of the transition state in the oxygen hydrogenation step is reduced by 50 kJ/mol and becomes very close to that of the sequential carbon hydrogenation step. In this scenario, water does not participate directly in any of the reaction steps, but its presence changes the energetics of the adsorbed intermediate and surface bound product.

In the second scenario, theoretical calculations suggest that a water molecule can directly participate in the reaction, as shown in Figure 16b. Specifically, a water molecule, adsorbed in the proximity of furfural can form a H bond with the carbonyl group and, in the liquid phase, can take the H atom directly from the surface, while transferring one of its original H atoms to the carbonyl group, via the aforementioned H bond. The atomic structures are shown in Figure 17. The transition state includes a proton bound to a water molecule and a negative charge remaining in the metal (Figure 18). In this case, the water molecule is within the first solvation shell and acts as a bridge between the carbonyl group and the surface H atom. The barrier for oxygen hydrogenation is further reduced by 7 kJ/mol. The hydrogenation of carbon becomes the rate-limiting step (Figure 16c). Because of the dynamic nature of the H transfer process, the H atom carries no dynamic "memory" of its origins at the surface. We also observe that, though only one water molecule directly participates in the reaction, the aqueous environment helps stabilizing the transition state: The true activation barrier for the first hydrogenation step in liquid water is lower than that when only a single water molecule was present. Figure 17 shows the charge density difference between

this H3O+ species and the remaining part of the transition state. The stabilization of the transition state in liquid water is caused by the dielectric screening of the liquid water, which is manifested by a noticeable charge redistribution between water molecules and the H3O+ species (Figure 17). This observation agrees with well-studied static and dynamic solvent-induced charge stabilization and redistribution in homogeneous catalysis[181, 182]. Furthermore, the stabilization of the hydrogenated intermediate and FOL by liquid water through hydrogen bonding results in a lower true activation barrier for the hydrogenation of the C atom in water (47 kJ/mol) compared to the single water case (67 kJ/mol) (see Figure 17).

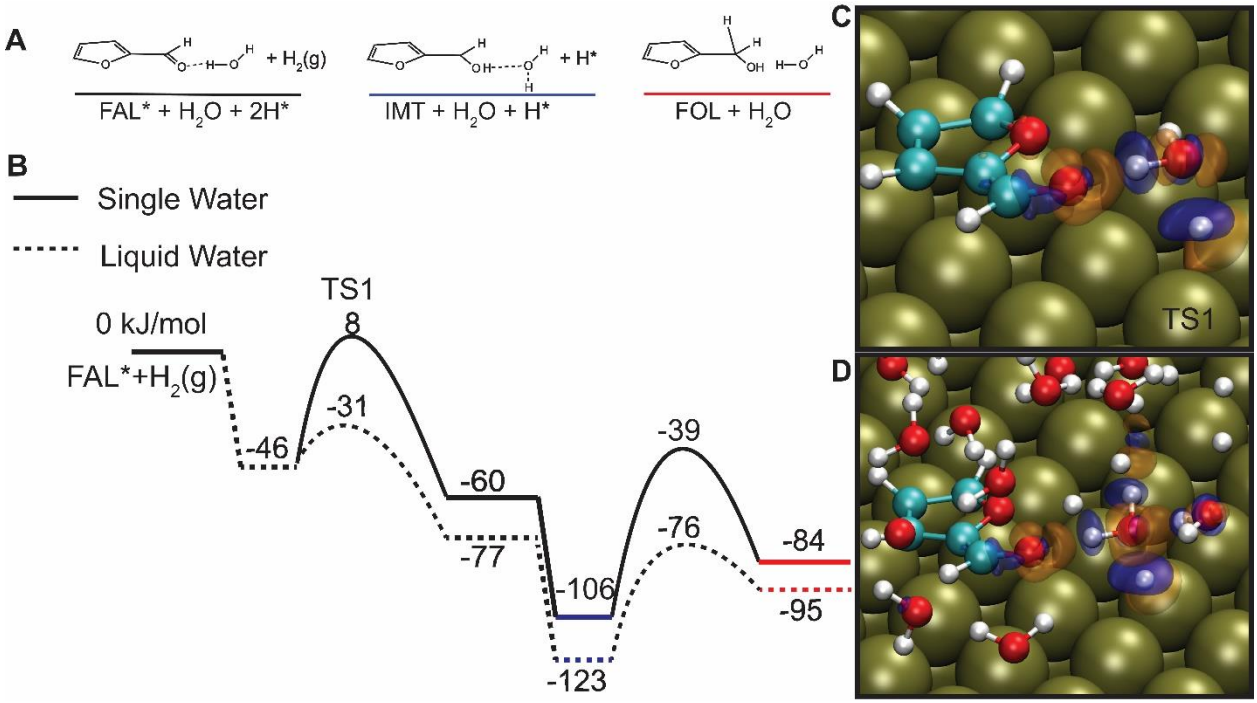

Figure 17. ***DFT calculations of hydrogenation of the carbonyl group of furfural in the presence of water.*** *Only the DFT-calculated total energies were used to plot this figure. (A) Schematics of the surface bound initial, intermediates and final products; (B) Energy profile of reaction via a single water molecule (solid line) and in liquid water (dashed line). (C) The charge transfer between the H_3O and the surroundings at the transition state (TS1) in (B); (D) Charge transfer between the H_3O and the surroundings at the transition state in (B), with yellow and blue indicating electron accumulation and depletion, respectively. The value used for the isosurface plot is ±0.02 e/Å^3.*

Additionally, we find that the liquid-phase water molecule that is outside the first solvation shell and does not form an H bond with the carbonyl group can also pick up a surface hydrogen to form H3O+, leaving an electron in the metal reservoir. This hydrogen-uptake step is the same as the Volmer step in any conventional electrochemical hydrogen oxidation reaction[183]. Once the surface H atom becomes a proton in solution, it can be shuttled through a H-bonded water network, via the well-known Grotthuss mechanism, with a low activation barrier of around 10 kJ/mol[184]. When the proton reaches a water molecule that forms an H bond with the carbonyl group, we find that the protonation step (and simultaneously the charge neutralization by the metal substrate) is barrierless. This shuttling scenario reduces the energy of the transition state for the oxygen hydrogenation by 12 kJ/mol as compared to the direct surface hydrogenation mechanism (Figure 15c). This process involves a series of proton transfers and is more likely to happen than the second scenario of a single step water-assistant proton transfer. Note that in all the reaction paths involving a water-mediated H transfer, the second hydrogenation step – the hydrogenation of the C in the aldehyde group – is the rate-determining step. This C atom does not form H-bonds with the neighboring H_2O molecules, and thus its hydrogenation is only affected indirectly by the modified adsorption configuration of the intermediate and final products. The more stabilized hydrogenation products via the H-bonds and the positively charged transition states by the dielectric screening work synergistically to reduce the energy of the transition state by more than 50 kJ/mol as compared to the water-free reaction path (Figure 15c). Note that the mechanism suggested here follows a conventional proton-coupled electron transfer (PCET), typically proposed for electrochemical reactions[185]. The description of the exact charge transfer process occurring at the interface is beyond the scope of this work.

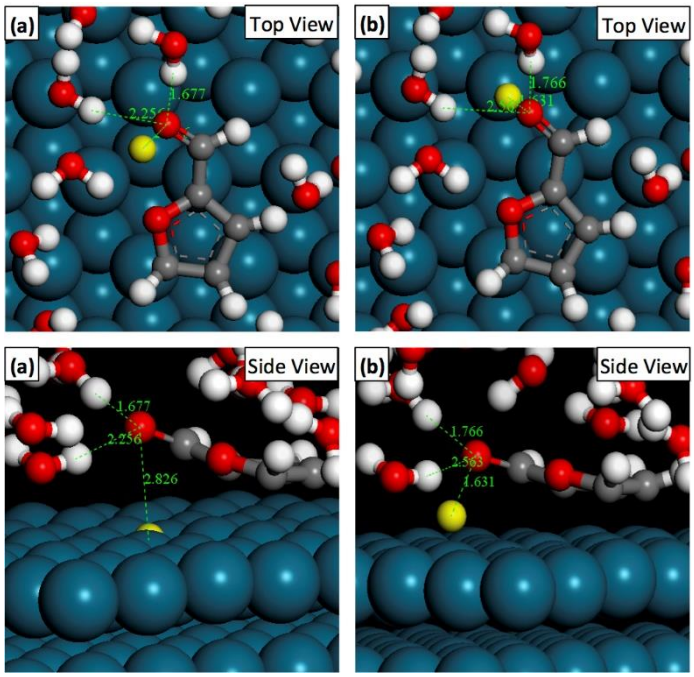

Figure 18 ***Structures of the initial and transition states.*** *(a) The initial low-energy configuration of furfural and a hydrogen atom at the water-Pd (111) interface (before hydrogenation). (b) The configuration of the transition state for hydrogenation when the surface hydrogen migrates towards the oxygen atom of the aldehyde group. The hydrogen atom that is initially on the surface is highlighted with a yellow color. For better visualization, some water molecules are not shown.*

Microkinetic analysis. To further identify the most likely reaction pathways, the maximum rate analysis has been performed[178]. Accordingly, we calculated the maximum rate of each elementary step, assuming in each case that this step is rate limiting while all the others are equilibrated. We find that, in the absence of water, the slowest step is the first one – oxygen hydrogenation; the maximum rate of this step is lower than the C hydrogenation by about an order of magnitude (Table 3). On the contrary, in the presence of water, the rate of O hydrogenation is significantly enhanced due to the reduced activation barrier. The maximum rate of O hydrogenation is about two orders of magnitude higher than hydrogenation of the C. That is, the latter becomes rate limiting, indicating a first-order dependence with respect to H2. This conclusion holds true for both mechanisms involving water-mediated proton transfer, and also true when considering all the O hydrogenation paths occurring in parallel. The maximum rate analysis thus agrees well with the experimental finding of approximately half order in H2 in the absence of water and about first order in H2 in the presence of water. This analysis thus suggests that the hydrogenation reaction of the aldehyde group more likely involves a water-mediated hydrogenation route for the O atom and surface-mediated hydrogenation path for the C atom, as summarized in Figure 20.

Steps	No water		Water (shuttling)		Water (parallel)		
	Max rate	Resistance	Max rate	Resistance	Max rate	Resistance	
1	1.3E+14	7.7E-15	1.3E+14	7.7E-15	1.3E+14	7.7E-15	
2	8.1E+7	1.2E-8	1.2E+8	8.6E-9	1.2E+8	8.6E-9	
3[a]	**9.5E+6**	**1.1E-7**			2.6E+7	3.8E-8	2.8 E-10
3[b]					3.8E+8	2.6E-9	
3[c]			3.1E+9	3.2E-10	3.1E+9	3.2E-10	
4	3.2E+8	3.1E-9	**6.3E+6**	**1.6E-7**	**6.3E+6**	**1.6E-7**	
5	1.8E+10	5.4E-11	4.2E+15	2.4E-16	4.2E+15	2.4E-16	

Table 3. Maximum rate analysis. The maximum rates and the corresponding resistances are compared for reactions in the absence and presence of water, respectively. In water, both the shuttling mechanism and the parallel reaction paths have been taken into account.

By contrast, in the hydrogenation of furfural in cyclohexane, the ring hydrogenation becomes the dominant reaction pathway. The calculated free energy profile suggests that, in the absence of water, the first hydrogenation step has the highest apparent barrier (Figure 19), supporting the experimental finding that the reaction is approximately half order in cyclohexane. This calculation was performed without explicitly including the cyclohexane solvent, the role of which we consider is merely competing for surface sites[167]. Although the exact free energy profile in cyclohexane may be different from this clean surface calculation, the trend should be the same.

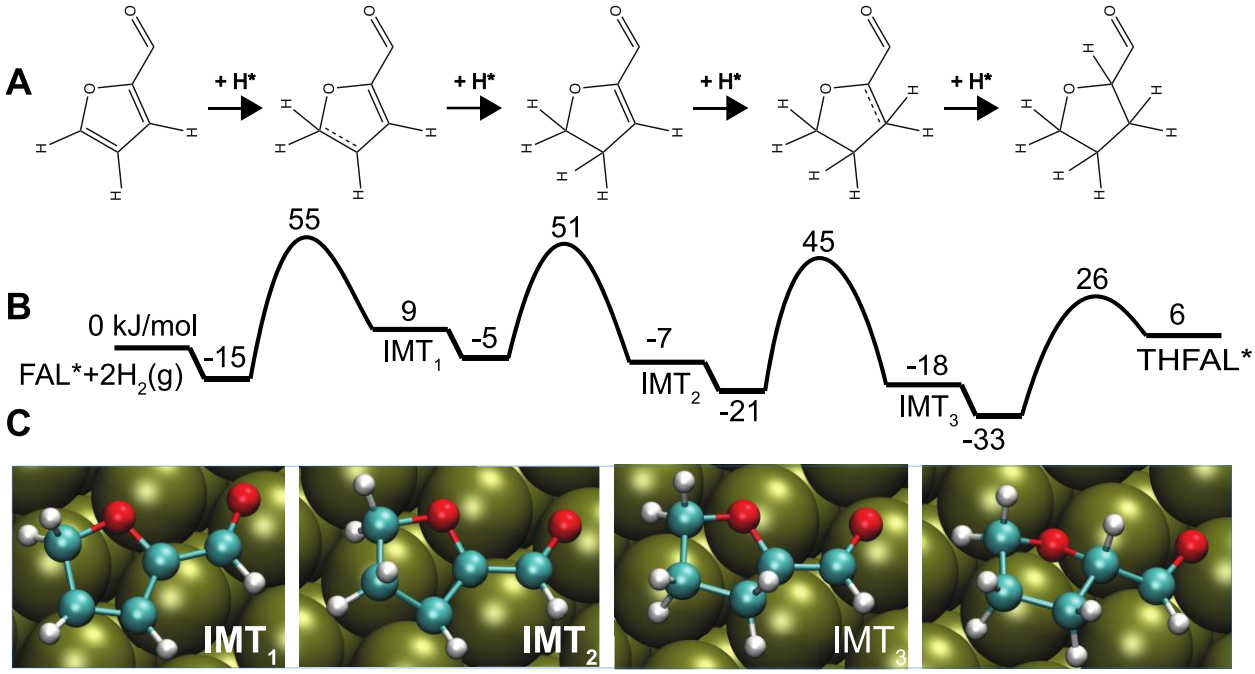

Figure 19. ***Free energy calculations of ring hydrogenation of furfural****. (A) Schematic reaction path in the vapor phase. (B) Reaction profile on clean Pd (111) surface to model the reaction in the oil phase. (C) atomic structures of the intermediates and final products.*

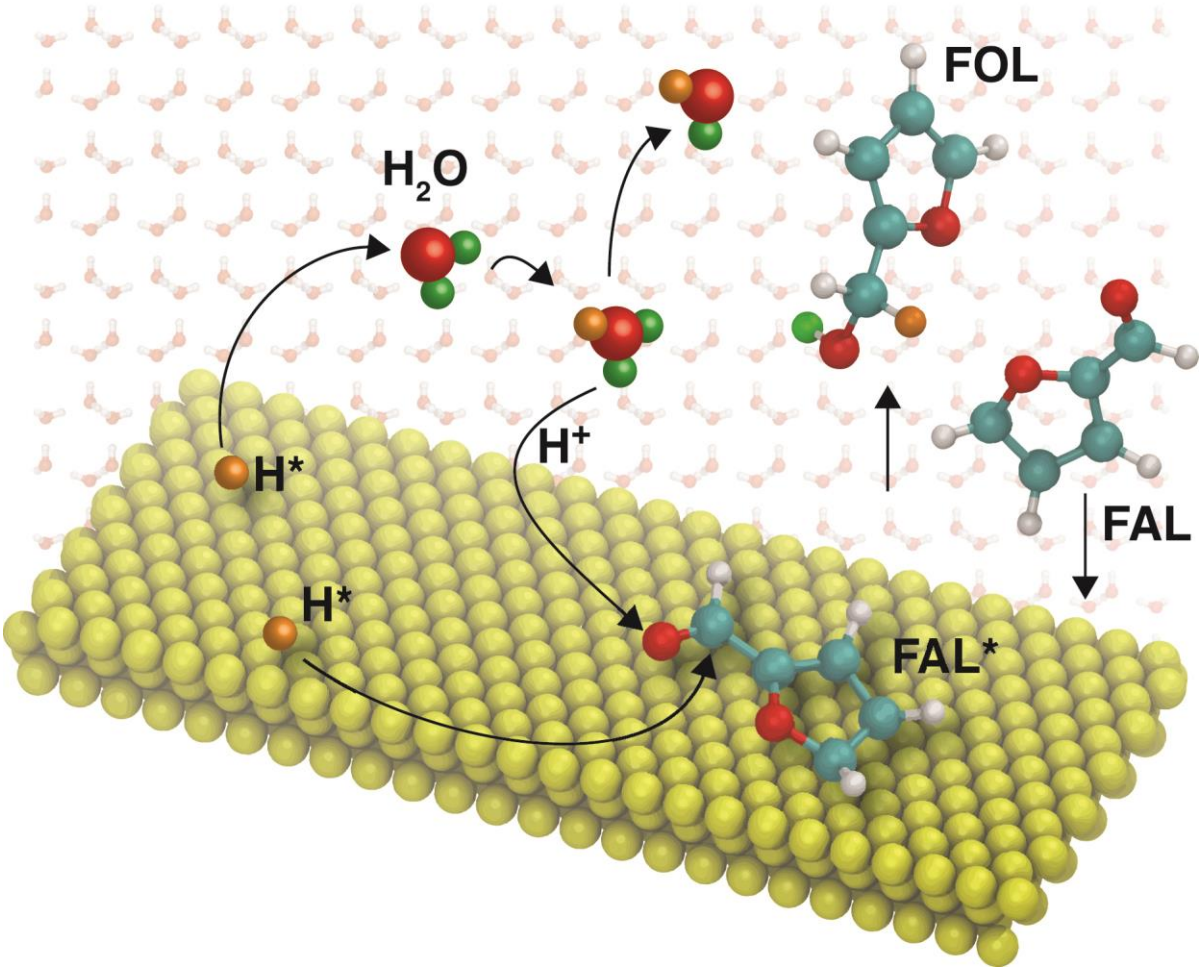

Figure 20. Reaction Scheme for the hydrogenation of furfural over a metal surface in water. Water directly participates in the key elementary steps. Both surface- and solvent-mediated hydrogenation paths are involved but play different roles for hydrogenation of C and O atoms in the aldehyde group.

4.4 Conclusion

We provide here theoretical insight and solid experimental evidences for an alternative reaction path provided by water over a Pd catalyst. That is, water influences the hydrogenation rate by taking part in the kinetically relevant step of furfural activation. Proton hopping within the first solvation shell and shuttling through the H-bonded water network reduces the activation barrier for the hydrogenation of the carbonyl group. Moreover, this work demonstrates the general concept that a solvent can provide additional degrees of freedom for tuning the activity and selectivity of a catalytic reaction. This phenomenon relies on feasible charge separation on the metal surface,

the extent of which may be affected by the intrinsic properties of the metal substrate[186], which opens up a number of potential opportunities for tailoring activity and selectivity.

Chapter 5: Mechanics Study of Electrocatalytic Conversion of Furfural to Methyl furan as a Primary and Major Product

5.1 Introduction

Furfurals are the second most abundant organic compounds (1st being acetic acid) obtained in the stage 1 torrefaction process of lignocellulosic raw material.[12] The conjugated carbon-carbon double bond in the furanic ring along with the aldehyde functional group in furfural can help establish principles for selectivity control towards hydrogenation of C=C, C=O, and C-OH hydrogenolysis of renewable oxygenates. Furfural has been used extensively in literature as a model compound for selectivity studies. Specifically, the hydrogenation and hydrogenolysis of furfural to yield more fuel-like compounds over different supported metal catalysts in a vapor phase has been studied. Sitthisa et al.[36, 147, 187] conducted a comparative study of Pd, Ni, and Cu for the hydrodeoxygenation of furfural in a vapor phase. Using SiO_2 as the support for all metals, the author showed that the selectivity in the vapor phase is dictated by the adsorption configuration of furfural on the metal surface. That is, a strong interaction between the heteroaromatic furanyl ring and the Pd or Ni surface leads to the formation of furan, while a tilted adsorption configuration on Cu through the carbonyl group results in a high selectivity to FOL. Through kinetic study of furfural on Cu supported on SiO_2, Sitthisia et al. also show that methyl furan can be obtained as a secondary product resulting from the hydrodeoxygenation of the furfuryl alcohol intermediate following an A → B → C type of reaction.

Thermal liquid-phase catalysis provides another option for tuning the selectivity. Previous results in the liquid phase, particularly in polar solvents [188, 189] on supported single metal[189] and multi-metallic metal[190] generally showed high yields of FOL. However, the underlying mechanism, particularly the role of water, is unclear.

Another strategy of upgrading furfural is through electrochemical hydrogenation and hydrodeoxygenation. Jung et al.[191] studied the impact of pH and catholytes on the electrochemical upgrading of furfural. Using a divided H-type cell, the group controlled the pH by using NH_4Cl and H_2SO_4 at different concentrations. The main products in the electrochemical hydrogenation and hydrodeoxygenation of furfural in acidic medium are furfuryl alcohol and methyl furan. Using 0.2 M NH_4Cl (pH = 3.4), the main product was furfuryl alcohol, while the yield of methyl furan was negligible. In sulfuric acid electrolytes, the nature of the products didn't change; however, the yield toward methyl furan increased significantly. In fact, the products yield of furfuryl alcohol and methyl furan in 0.1 M H_2SO_4 (pH = 1.1) was similar, between 11 and 14%. Increasing the pH to 0 by using 0.5 M H_2SO_4 showed a switch in selectivity of products. The selectivity towards methyl furan increased beyond that of furfuryl alcohol. The change in product distribution was explained to be due to the coverage of hydrogen on the working electrode surface. The group claims that an increase in pH provides a higher driving force for H-adsorption on the surface which results in the further hydrogenation of the intermediate furfuryl alcohol to yield methyl furan. The reaction of furfural favors the 4 (H^+, e^-) pair process to produce methyl furan compared to the 2 (H^+, e^-) pair process to produce furfuryl alcohol in more acidic conditions. Jung et al. also studied the effect of catholyte on the hydrogenation and hydrodeoxygenation of furfural. The authors added acetonitrile as a co-solvent to increase the solubility of furfural in electrolyte. It is established in literature that furfural can form larger molecular weight side products known as humins through homogeneous reactions in the presence of acids. Using 0.5 M H_2SO_4, they introduced acetonitrile at different ratios. They observed no increase in the mole balance of the reaction, which suggests that adding acetonitrile even at higher ratio (acetonitrile/water = 80%) did not hinder the degradation of furfural or inhibited side reactions. The group concluded that

mole balance of the reaction was not affected by adding an aprotic solvent. To further investigate mole balance, the authors plotted the yield of products and mole balance as a function of furfural conversion. They observed a linear decrease in mole balance as conversion of furfural increased. The yield of furfuryl alcohol and methyl furan increased with a slope lower in magnitude compared to mole balance. This decrease in mole balance was more apparent in the case of 0.2 M NH_4Cl, where furfuryl alcohol is the main product compare to that of 0.5 M H_2SO_4 where methyl furan is the main product. The authors concluded that furfuryl alcohol might be the source of the unbalanced carbon as it can undergo condensation to larger molecules that are hard to detect during product analysis. We should note here that if the reaction follows an A → B → C type of scheme, and that furfuryl alcohol (B) undergoes self-condensation to form polyfurfuryl alcohol, then a drop in mole balance should affect the yield of methyl furan (B → C). However, this is not what the authors observed as the increase in yields of furfuryl alcohol and methyl furan was linear throughout the whole reaction. Jung et al. studied the nonelectrochemical homogeneous reaction of furfural, furfuryl alcohol, and methyl furan as a function of time using the three different electrolytes previously stated. The group showed that furfuryl alcohol and methyl furan undergo homogeneous reactions in the presence of extremely acidic electrolyte (0.5 M H_2SO_4). They concluded that the fast evaporation of methyl furan captured in the acetonitrile trap prevented it from forming humins compared to furfuryl alcohol which accumulated in the catholyte giving more opportunity for self-condensation reactions.

Li et al. [192] also studied furfural reduction on copper electrode with the focus on gaining a better understanding on the mechanism of the electrocatalytic reduction of furfural to furfuryl alcohol and methyl furan. To distinguish between products resulting from electroreduction mechanisms, where protonation can occur in the bulk electrolyte with an electron transfer through

an outer-sphere process, and electrocatalytic hydrogenation, where a strong interaction between reacting species and electrode surface is needed for H_{ads} transfer, the group modified the copper electrode with SAMs of organothiols. Organothiols can rapidly form compact SAMs on copper which have been shown to inhibit electron transfer to substrates.[193, 194] The degree of inhibition is dependent on the chain length of organothiols used: a long chain can inhibit both inner and outer-sphere electron transfer processes, and a shorter chain allows the transfer of electrons through outer-sphere process while inhibiting the inner-sphere electron transfer process. For this study, the modification with a short chain organothiol would suppress reaction pathways resulting from electrocatalytic hydrogenation while allowing for electrochemical reduction of furfural. Based on their results, the authors concluded that the formation of hydrofuroin, which is not affected by the addition of SAMs, results from the electroreduction mechanism of furfural where a proton from the bulk and an electron transfer through the ligand is responsible for the protonation. On the other hand, the formation of furfuryl alcohol and methyl furan was greatly affected by the addition of SAMs. Methyl furan formation was almost completely suppressed during the reactions where 3-mercaptopropionic acid (MPA), 12-mercaptododecanoic acid (MDA) and a heterocyclic 2-mercaptobenzothiazole (MBT) were added. The rate of furfuryl alcohol formation was also reduced but not completely suppressed in the case of MBT and MPA modified electrodes. The authors claimed that this was due to the presence of pinhole defects or accessible sites resulting from the incomplete film of SAMs formed on the surface of the electrode. Based on these results, the group concluded that furfuryl alcohol and methyl furan formation followed an electrocatalytic hydrogenation mechanism where the reacting species interact strongly with the surface of the electrode. To further confirm that furfuryl alcohol and methyl furan are generated through electrocatalytic hydrogenation and hydrodeoxygenation mechanisms, the group used a different

electrode material on which electroreduction mechanisms are knows to dominate. Copper electrode was replaced by a lead electrode where hydrogen is known to adsorbed very weakly. The selectivity as a function of electrode and pH showed that over the lead electrode, a dominant selectivity towards hydrofuroin along with the suppression of furfuryl alcohol and methyl furan formation. This proves that an interaction of both reacting species (furfural and hydrogen) with the surface of the electrode is necessary for the hydrogenation and hydrodeoxygenation of furfural to form both furfuryl alcohol and methyl furan. Jung et al., as previously noted, suggested that methyl furan is a secondary product of furfural reduction on copper, with furfuryl alcohol as an intermediate under acidic conditions. This would result in a selectivity switch as conversion increases where furfuryl alcohol would be the major product at low conversion, while methyl furan would be the preferred product at higher conversion. In contradiction to Jung et al., Li et al. found that the selectivity of products remained constant with respect to reaction time and degree of conversion. The authors concluded that furfuryl alcohol and methyl furan are generated through parallel, not consecutive reactions, on copper electrodes.

Despite extensive discussion of the electrocatalytic hydrogenation of furanics in the literature as summarized in recent reviews[24, 195], it remains unclear if the bias-driven reaction has the same mechanism as in the gas-phase and aqueous-phase reactions as shown in the example of phenol and benzaldehyde; if the mechanisms are different, it remains unclear which hydrogen species participate in the kinetically relevant elementary steps. This ambiguity is partially caused by the co-existence of several different hydrogen species, such as protons, surface-adsorbed hydrogen atoms, and hydrides, and partially caused by the complexity, e.g. presence of solvent and electrode potential, of this system. These are the questions that we intend to address in this contribution.

5.2 Methods

Experimental methods

SiO_2 was used as a support for a 10 wt. % Cu catalyst, synthesized by a sequence of incipient wetness impregnation steps. The silica support was acquired from Sigma-Aldrich. A series of three sequential incipient wetness impregnation steps was applied, incorporating 3.3 wt. % of Cu during each step, followed by intermediate heating treatments. To minimize the occlusion of Cu precursor in each impregnation, a liquid/solid ratio of 0.1 mL per gram of SiO_2 was used in each step. After the first incipient wetness impregnation with the $Cu(NO_3)_2.2.5\ H_2O$ aqueous solution, the catalyst was dried in a vacuum oven overnight at 70°C, followed by calcination in air at 400°C for 4h. Identical steps were followed for the second and the third impregnations, resulting in a final loading of 10 wt.% Cu.

Liquid phase reactions were carried out in a high-temperature, high-pressure Parr stirred batch reactor with a total volume of 50 mL. 30 mL total volume of solvent and reactants and 70 mg of catalyst were loaded into the reactor before reaction. The reaction system was purged with H_2 to vent air, and then the reactor was pressurized to 400 psi of H_2. The catalyst was reduced at 270 °C for 3h. The reactor was cooled down to reaction temperature and then 5 mL of solvent which contained distilled furfural was purged into the reactor for a total final pressure of 1000 psi.

The liquid product was filtered and analyzed by gas chromatography. Shimadzu GCMS-QP2010S equipped with a Zebron ZB-1701 column was used for identification of products in the liquid mixture. Agilent 7890B GC-FID equipped with a Zebron ZB-WAXplus column was used for quantification of the individual product. Conversion and yields toward each product are defined as follows:

Electrocatalytic reactions

$$\text{Conversion x\%} = \frac{\text{mole of reactant reacted}}{\text{mole of reactant fed}} * 100\% \quad (1)$$

$$\text{Yield y\%} = \frac{\text{mole of product i obtained}}{\text{mole of reactant fed}} * 100\% \quad (2)$$

A custom-built electrochemical cell made from polycarbonate was employed for the electrocatalytic study (Figure 21). The cell consists of 2 chambers of 15 mL maximum volume capacity. During all experiments, 11 mL of solution was used on each chamber. The cathode side chamber was connected to a trap for the collection of volatile products. The working electrode and the refence electrode were maintained parallel to each other to insure uniform voltage. The cell was designed to have a large electrode area of 8.4 cm^2.

Electrochemical reactions were carried out with an Agilent B2902A Precision Source/Measure Unit (SMU). Data was collected vs. Ag/AgCl reference. Copper foil (thickness 0.05 mm, reagent grade, Carolina) was used as the working electrode. Prior to each experiment, the surface was mechanically polished until no discoloration was visible then chemically polished using 0.1 M HCl solution to remove any oxides. Platinum foil was used as the counter electrode. The proton exchange membrane (CMI-7000, Membranes International Inc.) separating the two chambers of the electrochemical cell was immersed in 0.5 M H_2SO_4 for 24 hours prior to experiment. The liquid products from the anode and cathode chambers were extracted using Diethyl ether with a 1:1 ratio. 5 mL of pure acetonitrile was used to trap volatile products. The products analysis was carried in a similar fashion as in the thermal reactions. Impedance spectroscopy was conducted to calculate the resistance in the electrolyte. The reported potentials are adjusted to reflect the actual values after elimination of resistance.

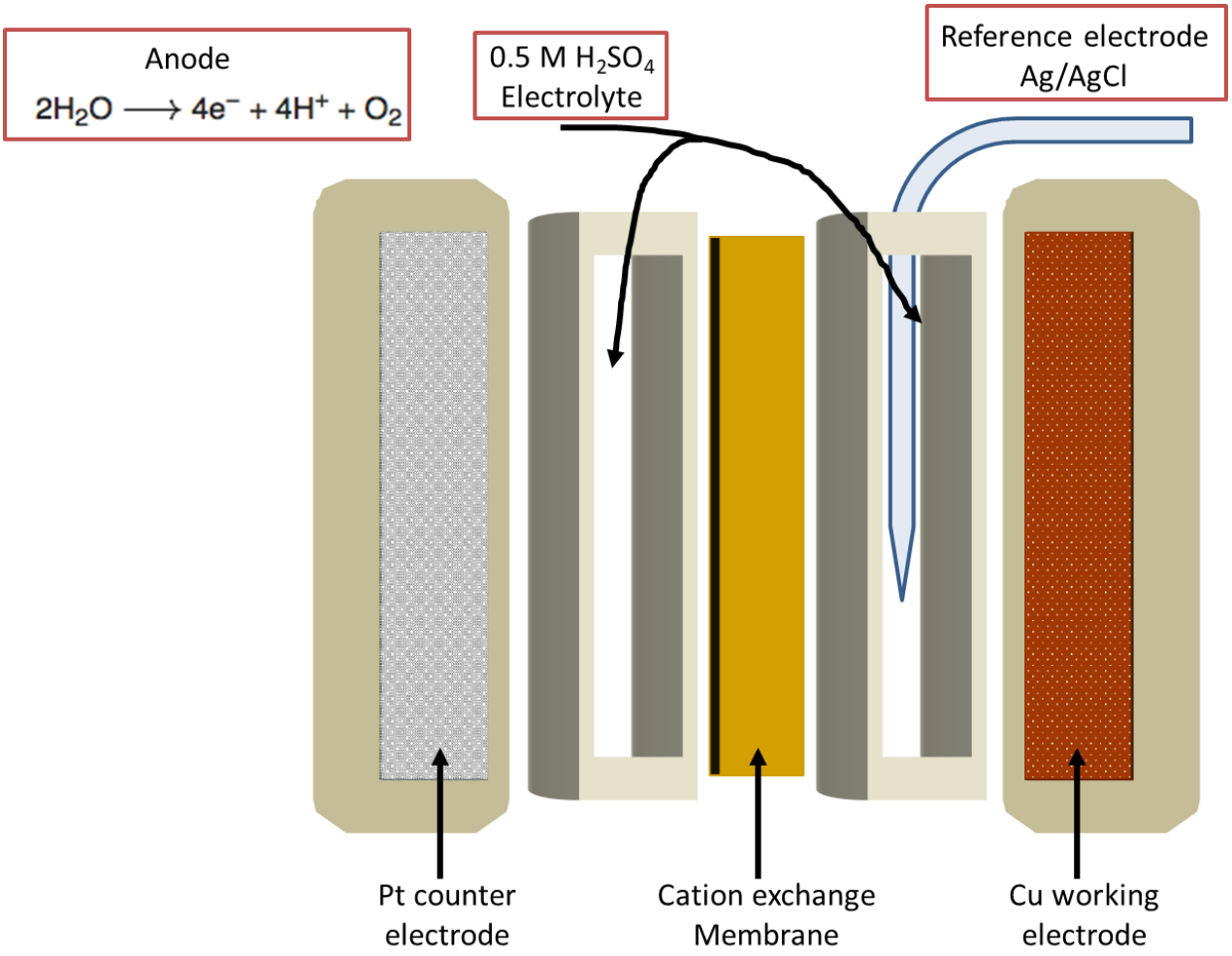

Figure 21. Schematic of the electrochemical cell (Adapted from [196])

Computational simulations.

The Cu (111) surface was modeled using a (4×4) supercell. Each supercell contained repeated slabs with four metal layers separated by an xx Å vacuum region. The bottom two layers of Cu have been fixed at their bulk positions while the top two layers were fully relaxed. A number of water molecules were chosen to fill the vacuum region above the metal slab to make the density of water approximately the same as that of liquid water at the standard conditions. The density functional theory (DFT) calculations and ab initio molecular dynamics (AIMD) simulations were carried out using the VASP package[91]. The Perdew-Burke-Ernzerhof generalized gradient approximation exchange-correlation potential (PBE-GGA)[92] was used, and the electron-core

interactions were treated in the projector augmented wave (PAW) method[93, 94]. Structures have been optimized until the atomic forces were smaller than 0.02 eV $Å^{-1}$ with a kinetic cut off energy of 400 eV. The van der Waals interactions were taken into account using DFT-D3 semi-empirical method[165]. Reaction pathways and the associated barriers were determined with the Climbing Image Nudged Elastic Band method[125, 126] and the dimer method[166]. The surface Brillouin zone was sampled with single k point at Gamma for the AIMD simulations and NEB and dimer calculations for the reaction profile at the solid/liquid interface. For simulations of the water-Cu (111) interface, AIMD simulations at finite temperatures (see text) were performed in canonical ensembles. The time step was set to 0.5 fs. After thermal equilibrium has been reached, multiple snapshots were taken and optimized for further DFT calculations.

Enthalpy corrections. Temperature-dependent enthalpy was calculated using DFT calculated electronic energy at 0 K and the harmonic approximation for zero-point energy and heat capacity which accounts for the difference in temperature between DFT calculated energies at 0 K and the actual experiment temperature of 313.15 K.

$$H(T) = E_{elec} + E_{ZPE} + \int_{0K}^{T} C_v dT$$

$$E_{ZPE} = \frac{1}{2} \sum_{i=0}^{\#DOF} h\nu_i$$

$$\int_{0K}^{T} C_v dT = \sum_{i=0}^{\#DOF} \frac{h\nu_i}{e^{h\nu_i/k_B T} - 1}$$

where k_B is the Boltzmann constant, h the plank's constant, and v_i is the vibrational frequency obtained based on DFT calculations. All the vibrational frequencies from DFT were used to evaluate the zero-point energy and thermal capacity.

Entropy calculation. Vibrational entropy contribution was calculated using the harmonic normal mode approximation

$$S\,(T) = k_B \sum_{i=0}^{\#DOF} \frac{hv_i}{k_B T\left(e^{hv_i/k_B T} - 1\right)} - \ln\left(1 - e^{-hv_i/k_B T}\right)$$

Translational and rotational contributions to entropy for all surface reactions were assumed to be constant. On the other hand, gas phase adsorbate species (furfural and furfuryl alcohol) were assumed to retain $\sim\frac{2}{3}$ of gas phase entropy upon adsorption, and then remain constant over the elementary steps of surface reactions. This assumption was based on previous work on adsorbed alkanes[169]. The Gibbs free energy change was calculated based on enthalpy and entropy changes $\Delta G = \Delta H(T) - T * \Delta S(T)$.

5.3 Results and discussion

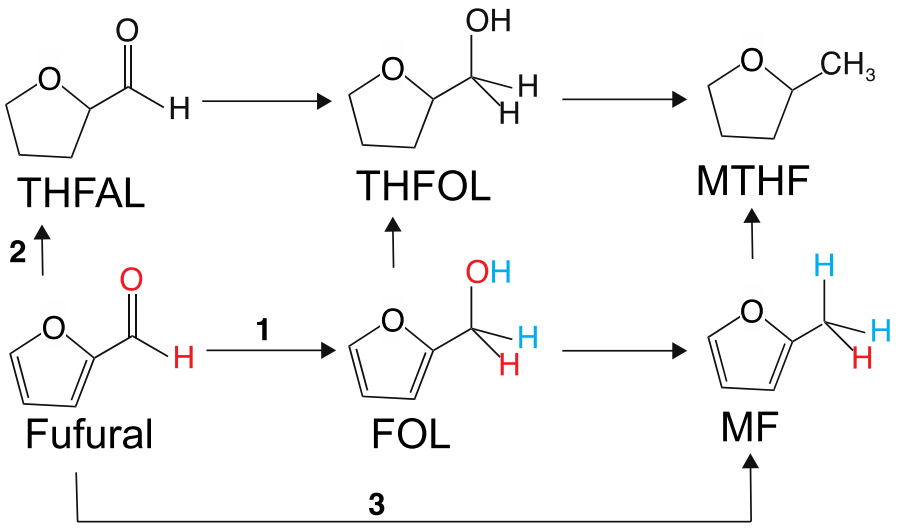

Figure 22 Reaction network of hydrogenation of the conjugated C=O and C=C bonds in furfural leading to production of a variety of different chemicals. On a copper catalyst, the dominate reactions are highlighted by thick arrows.

Figure 22 shows the reaction scheme of furfural when using copper as the catalyst. Hydrogenation of the aldehyde group (route 1) and furan ring (route 2) leading to production of FOL and THFAL; hydrogenolysis of the C-O bond in FOL produces MF. It is generally considered that the MF is a secondary product from the primary FOL, however, as discussed below, production of MF could be primary and dominant in electrocatalysis (route 3). Vapor-phase hydrogenation of furfural has been well-studied in literature[147]. It is generally believed that, because of the weak interaction between the furan ring and the Cu surface, the C=O double bond, rather than the furan ring, is hydrogenated producing FOL; due to the low activity for hydrogenolysis of the C-O bond on Cu, manifested by a high activation barrier calculated in DFT calculations[197], production of MF is very limited. Hydrogenation of the C=C bond of furfural to make tetrahydrofurfural (THFAL) via route 1 is also of low selectivity because of the feasible hydrogenation of the C=O bonds.

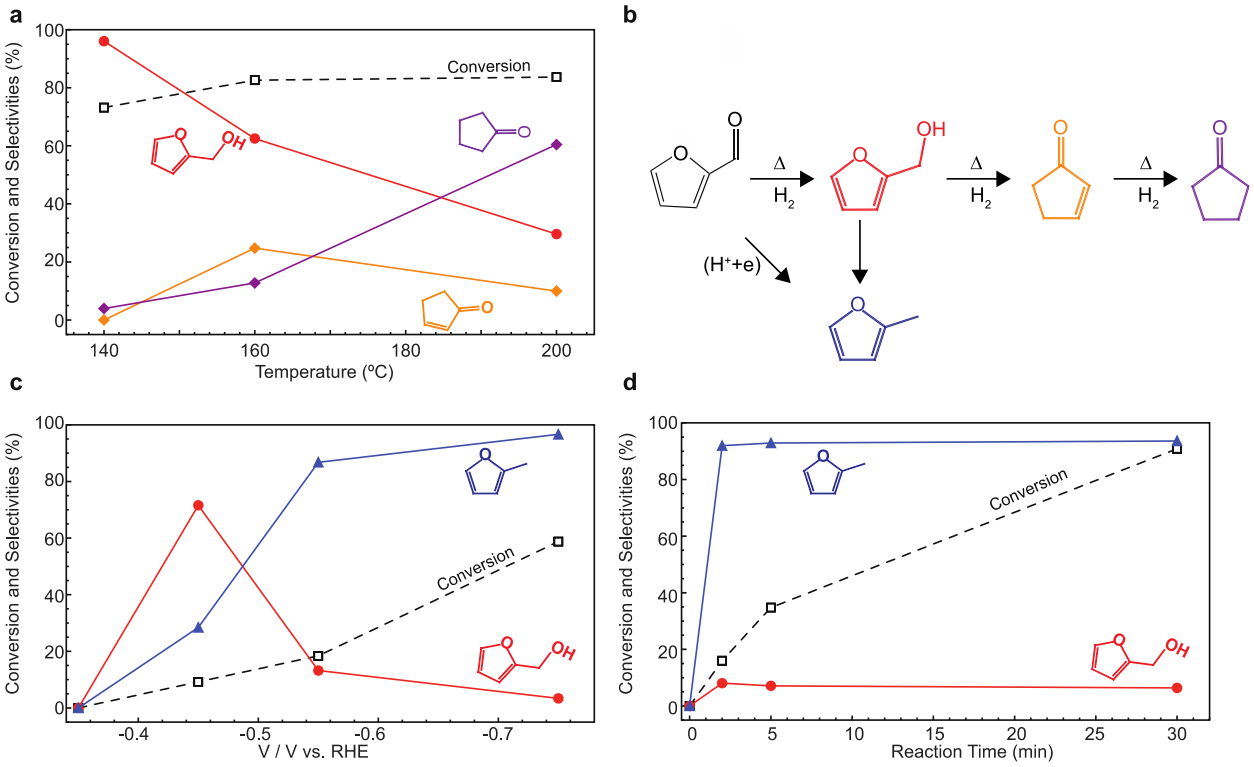

Figure 23(a) Conversion and selectivity of furfural conversion in a thermal-driven aqueous phase reaction (b) Schematic of reaction in thermal-catalysis and electrocatalysis (c) and electrocatalysis at different electrode potentials (d) and as a function of time.

In the following we compare aqueous-phase thermal hydrogenation of furfural and its electrocatalytic reaction using copper catalysts. Figure 23 shows catalytic selectivity at different temperatures of Cu-catalyzed furfural hydrogenation in water. Similar to the vapor phase, FOL is the major product; MF is not detected in the liquid-phase reaction. Note we intentionally operated the reaction at high conversion; No MF production was detected over a wide range of conversion. When the reaction temperature is higher than 140 °C, ring-arrangement products including cyclopentanone and cyclopentenone start to dominate product distribution. The product distribution at different temperatures suggest that production of cyclopentenone (green curve) is secondary, through water-assisted ring-arrangement of FOL, while cyclopentenone is produced from hydrogenation of cyclopentenone (Figure 23b). Note MF has not been observed at these

temperatures. This low activity to hydrogenolysis could be caused by dissolution of FOL, which has higher solubility than furfural in water and feasible ring-arrangement reactions at high-temperatures (>140 °C). Note there is also a selectivity difference between aqueous-phase and vapor-phase reactions: in vapor-phase hydrogenation of furfural on Cu/SiO_2, previous works showed small but significant amount of MF as a secondary product[147], while in the current aqueous-study, we didn't detect production of MF. This high selectivity to FOL agrees with the previous report of almost 100% selectivity toward FOL using Cu/SiO_2 catalysts[163]. One explanation is that due to the high solubility of FOL in water and a considerable activation barrier for hydrogenolysis of FOL to produce MF, the selectivity to MF is further lowered in an aqueous phase than it in a vapor phase.

Distinctly, Figure 23c shows product distribution in an electrocatalytic cell, in which it shows MF is the major product. Production of FOL is moderate and is almost independent of the electrode potential. This selectivity is different from catalysis using other transition metals as the electrocatalysts, such as Pd, Pt and Ni, on which FOL is the primary and major product[198-200]. Figure 32b shows the product yields as a function of reaction time at an electrode potential of -0.9 V vs RHE. Analysis of the data at the beginning of the run (Figure 23d) shows MF is also a primary product, rather than via the hydrogenolysis of FOL. This intriguing result is very different from Cu-catalyzed vapor and liquid-phase reactions and suggests a different route that produces MF directly from furfural. Note other recent reports also indicated a parallel reaction path for producing FOL and MF, though the mechanism has not been revealed.

We tried to feed FOL as the reactants in the electrochemical cell, but the carbon balance was very low likely caused by polymerization of the partially hydrogenated intermediates[201]. This result is very different from the same reaction but conducted in a water phase at 160 °C, in which,

similar to the vapor phase, FOL is the major product. Note as a significant difference, MF is not detected in the liquid-phase reactions.

In the following, we applied DFT-based free energy calculations to investigate the reaction mechanism. The reaction energy is shown in Figure 24. Based on the activation energies calculated from the first principles study, we find that the first hydrogenation step of the C=O double bond starts with the hydrogenation of the carbon on a Cu surface (Ea = 64 kJ/mol) rather than O (Ea = 72 kJ/mol) in liquid water, which agrees with previous DFT calculations[197]. The opposite hydrogenation sequence, that is, O first followed by C on Cu, is less favored both thermodynamically and kinetically as shown in figure 24. However, in the case of applied bias in electrocatalytic reactions, the dehydration route of furfural to produce directly methyl furan might become more energetically favored. The electronegative oxygen in the aldehyde group can be easily protonated by protons in the electrolyte to form the dehydrated intermediate FAL-CH, resulting in a direct route to produce methyl furan. Once furfural alcohol is produced, hydrogenolysis breaks the C-O bond and hydrogenation of the C produces MF. Though the reaction is energetically favored, the high solubility of FOL in water may lead to desorption prohibiting sequential reactions, which explains why no methyl furan was detected in the thermal reactions.

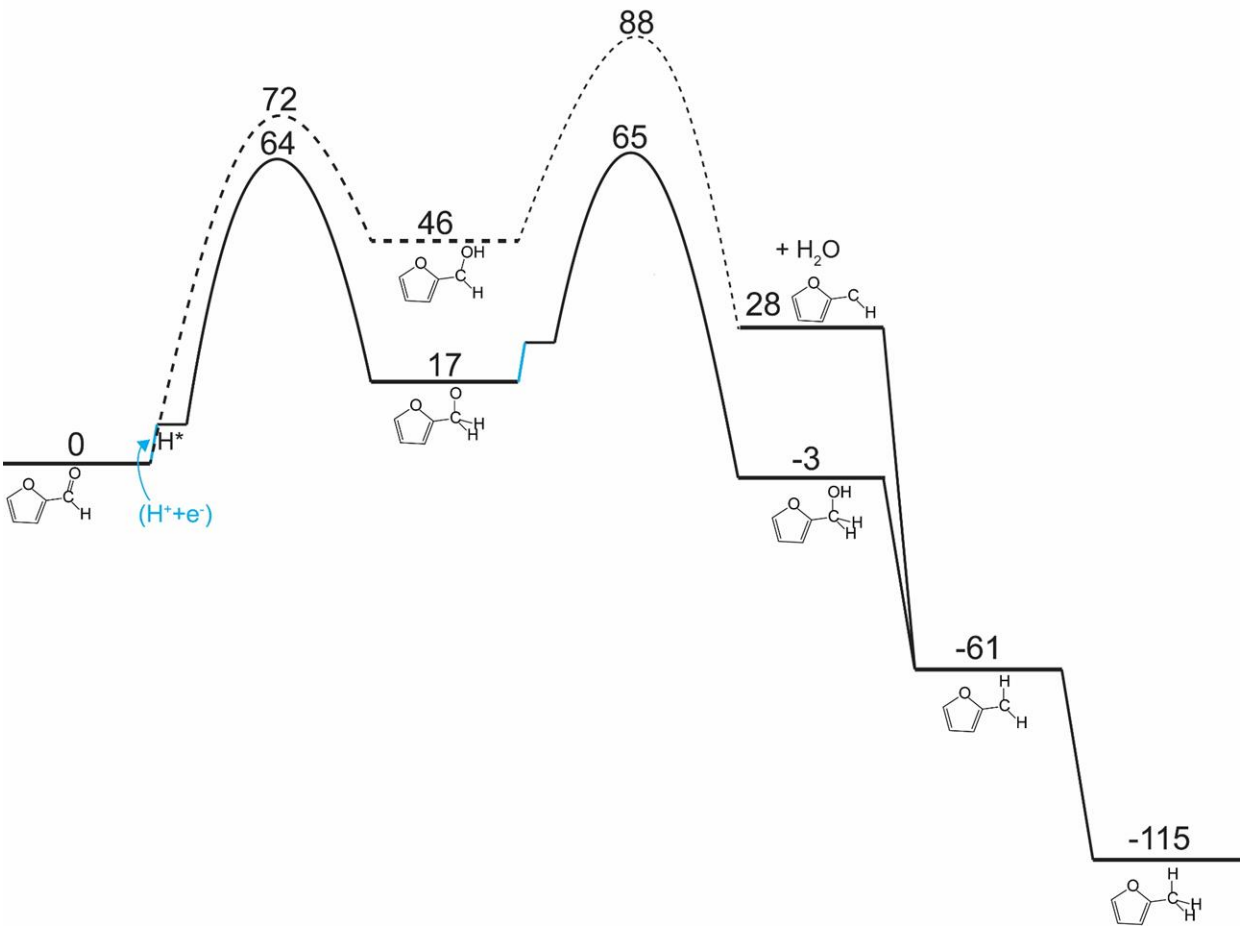

Figure 24 calculated reaction energies of furfural routes to furfuryl alcohol and methyl furan in liquid water.

Based on experimental results shown in figure 23, methyl furan becomes a major and primary product in the case where a negative electrode potential is applied. Note that in the calculations presented in figure 24, hydrogenation always starts with a surface bounded hydrogen species, while in electrocatalysis, (H^+ and e^-) pair drive the reaction. Protons transported in the electrolyte from the anode side to the electrode side can protonate directly the electronegative oxygen of the aldehyde group. When the electrode potential is introduced, the activation energy for the protonation of the oxygen in the C=O double bond is significantly lowered (figure 25). A second proton attacks O atom through the H-bonded water network, accompanied by an electron transfer through the electrode surface in a likely concerted way[202], leads to a hydrogenolysis of the C-

O bond and formation of a water molecule (second step in figure 25). The first protonation step of the oxygen when a -0.5 V bias is applied becomes barrierless, while the activation energy for the second protonation to break the C-O bond becomes more energetically favored compared to the hydrogenation of the carbon of the aldehyde group resulting from a hydrogen originating from the surface of the electrode to produce furfuryl alcohol (figure 25). Further hydrogenation of the –CH group produces methyl furan without reacting through the furfuryl alcohol intermediate. In the last two hydrogenation steps, the reaction is driven by surface reactions, because the –CH group is rather hydrophobic and doesn't form H-bonded water network for proton shuttling (figure 24). Note production of furfuryl alcohol and methyl furan is a 2- and 4-electron process[191, 199] respectively, and our results here suggest that the sequence of the (H^+ and e^-) can be tuned by the electrode potential. It is interesting to notice liquid phase thermal catalytic and electrocatalytic conversion of phenol have no significant change in terms product distribution in previous works[203, 204], which supports our hypothesis that the bias-driven and water-assisted hydrogenation and dehydration is more pronounced when the reactants possess a polar functional group such as aldehyde and alcohol groups.

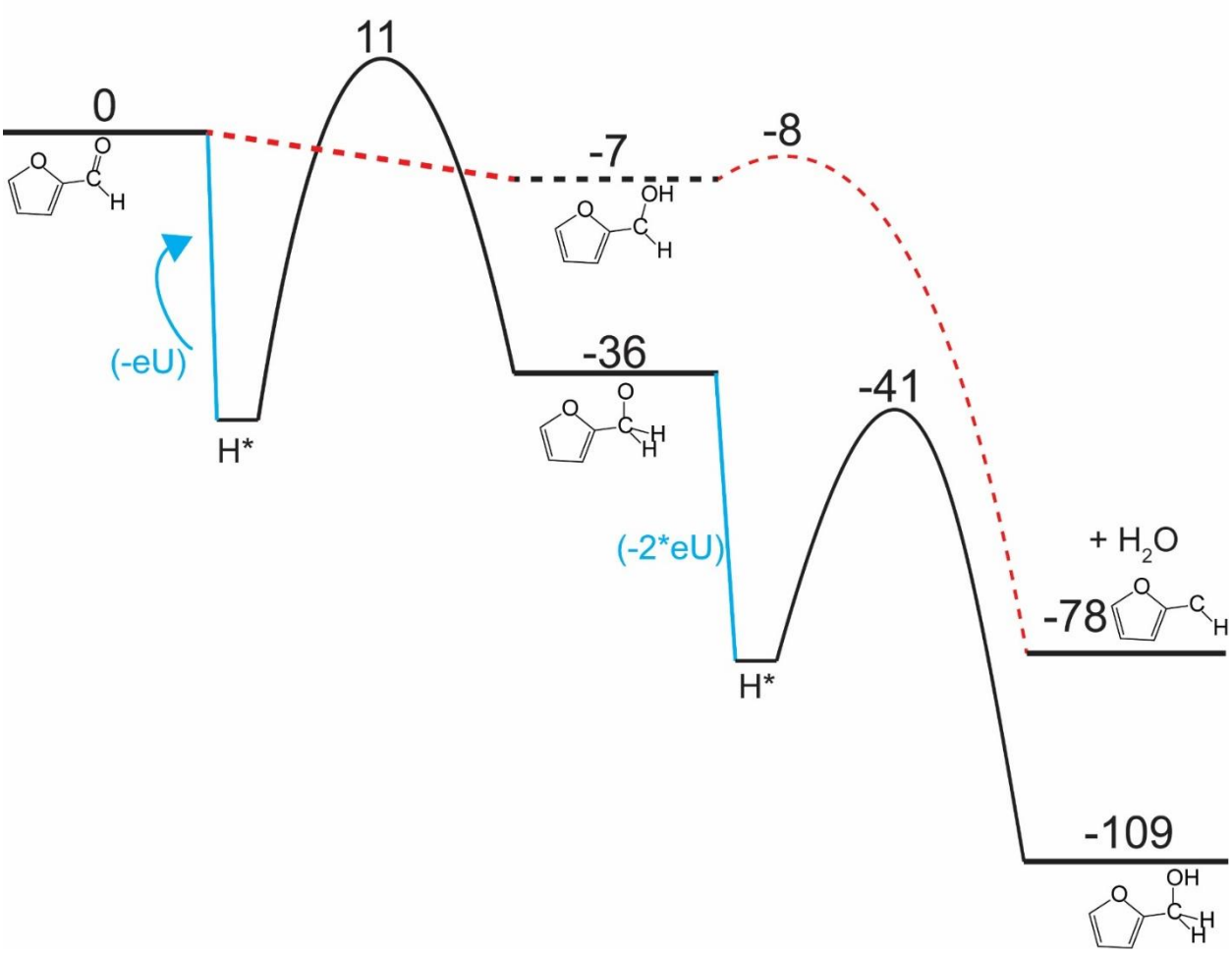

Figure 25. Calculated reaction energies of furfural routes to furfuryl alcohol and methyl furan in liquid water with a bias of -0.55 eV.

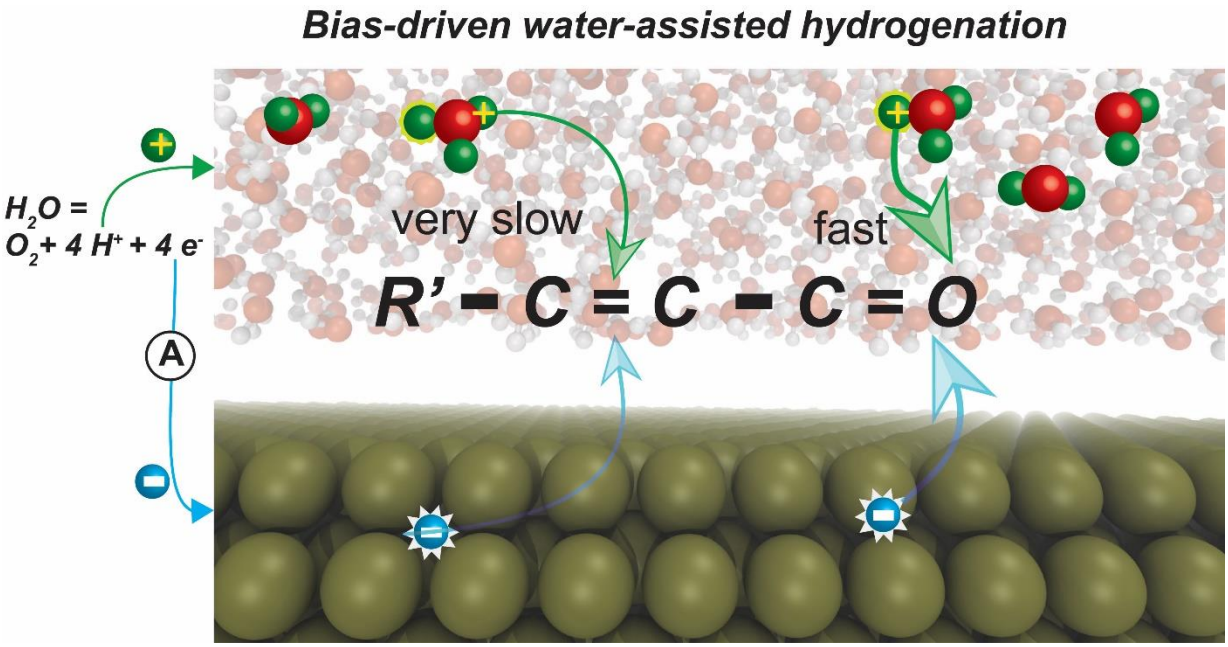

Figure 26. Schematics to show that water-assisted proton transfer under negative electrode potentials, which facilitates hydrogenation and hydrogenolysis of the aldehyde group in furfural or more generally oxygenates.

5.4 Conclusion

As discussed in the results of thermal/electro catalytic furfural hydrogenation, we can conclude that hydrogenation of the aldehyde group HC=O is preferred in the presence of the liquid phase, and that the hydrogenolysis of the C-O bond is driven by the electrode potential, which changes the free energy of the reaction profile, while the oxygen and C=C bonds within the furan ring was not affected much, in other words, no ring opening products and few ring-hydrogenated products were detected in the reaction. These phenomena can be explained by the water-assisted proton transfer, which is further dictated by the electronic potential. We plan to investigate a few more biomass-derived model compounds to further establish the reaction principles and then extend it to C5 and C6 sugars. The latter one may allow producing valuable chemicals from biomass within much less reaction steps.

Acknowledgements

We appreciate Ian Sellers, Vincent Whiteside and Gabriel LeBlanc for assistance with the impedance measurement. This work was supported by the U.S. Department of Energy, Basic Energy Sciences (Grant DE-SC0018284). The computational research used the supercomputer resources of the National Energy Research Scientific Computing Center (NERSC) and the OU Supercomputing Center for Education & Research (OSCER) at the University of Oklahoma.

Chapter 6: Conclusions and outlook

6.1 Dissertation Summary

Utilization of renewable carbon sources in the production of fuel and attractive chemicals requires obtaining and processing inexpensively an abundant biomass feedstock. Due to the high chemical diversity of compounds in biomass, understanding the mechanism step by step at the atomic level of their upgrading is important. Multiple factors can influence the selectivity of reactions in heterogeneous catalysis. To acquire a great and detailed understanding of how reactions can be influenced to produce valuable products using biomass, extensive experimental and computational studies were conducted. The following studies described in the thesis investigate the factors that influence selectivity in heterogenous catalysis.

In Chapter 2, ligand effect was investigated. The strong parallels between coordination chemistry and adsorption on metal surfaces, with molecules and ligands forming local bonds to individual atoms within a metal surface, have been established over many years of study. The recently proposed “surface trans-effect” (STE) appears to be a further manifestation of this analogous behavior, but so far, the true nature of the modified molecule–metal surface bonding has been unclear. The STE could play an important role in determining the reactivities of surface-supported metal–organic complexes, influencing the design of systems for future applications. However, the current understanding of this effect is incomplete and lacks reliable structural parameters with which to benchmark theoretical calculations. Using X-ray standing waves, we demonstrate that ligation of ammonia and water to iron phthalocyanine (FePc) on Ag (111) increases the adsorption height of the central Fe atom; dispersion corrected density functional theory calculations accurately model this structural effect. The calculated charge redistribution in the FePc/H_2O electronic structure induced by adsorption shows an accumulation of charge along

the σ-bonding direction between the surface, the Fe atom and the water molecule, similar to the redistribution caused by ammonia. This apparent σ-donor nature of the observed STE on Ag (111) is shown to involve bonding to the delocalized metal surface electrons rather than local bonding to one or more surface atoms, thus indicating that this is a true surface trans-effect.

In Chapter 3, detailed mechanistic study of biomass-derived oxygenate was conducted. Conversion of biomass-derived γ-valerolactone (GVL) to valuable chemicals has been experimentally studied extensively. However, a detailed understanding of the reaction mechanism which is very valuable for improving turnover rates and product selectivity was never reported in literature. Here, we report first-principles density functional calculations, through which we show in detail the reaction pathways of GVL conversion on a Ru (0001) surface, in good agreement with recent experimental results performed on supported Ru catalysts. We find that (*i*) GVL undergoes a ring-opening reaction rather easily, and (*ii*) the rate-limiting step toward the formation of 1,4-pentanediol (1,4-PDO) and 2-pentanol (2-PeOH) is the hydrogenation step. The high energy barrier for this step is caused by a strong interaction between Ru and the unsaturated acyl intermediate that is formed after opening the ring. Among all the primary products, formation of 2-butanol (2-BuOH) has the smallest activation barrier, while the slowest step is C–C bond cleavage in the decarbonylation step. We further show that the same acyl intermediate after ring opening of GVL can also be formed by dehydrogenation of 1,4-PDO with a moderate activation barrier, which suggests that both 2-PeOH and 2-BuOH can also be produced in secondary steps.

In Chapter 4, the solvent influence on selectivity in heterogenous catalysis was studied. Compared to the vapor phase, liquid-phase heterogeneous catalysis provides additional degrees of freedom for reaction engineering, but the multifaceted solvent effects complicate analysis of the reaction mechanism. Here, using furfural as an example, we reveal the important role of water-

mediated protonation in a typical hydrogenation reaction over a supported Pd catalyst. Depending on the solvent, we have observed different reaction orders with respect to the partial pressure of H_2, as well as distinct selectivity towards hydrogenation of the conjugated C=O and C=C double bonds. Free energy calculations show that H_2O participates directly in the kinetically relevant reaction step and provides an additional channel for hydrogenation of the aldehyde group, in which hydrogen bypasses the direct surface reaction via a hydrogen-bonded water network. This solution-mediated reaction pathway shows the potential role of the solvent for tuning the selectivity of metal-catalyzed hydrogenation when charge separation on the metal surface is feasible.

In Chapter 5, an extra degree of freedom was added along solvent to influence selectivity. By combining density functional calculations and experimental study of both aqueous-phase thermal catalytic and electrocatalytic conversion of biomass-derived furfural, we reveal the fundamental difference in elementary steps in the two reaction systems and provide an explanation for the distinct product selectivity. Specifically, we observed that furfural alcohol and methyl furan, which are the hydrogenation and hydrogenolysis products of furfural, respectively, are both primary products in electrocatalysis with the latter one dominating the product distribution. While in the aqueous-phase thermal reaction, furfural alcohol and its derivatives are the major products without production of methyl furan. Density functional theory based free energy calculations show that, though thermodynamics favors all hydrogen-involving reactions in the same way under negative electrode potential, the kinetics are greatly enhanced only when protons are directly involved in the rate-limiting steps. Electrocatalysis, by controlling the free energy of protons and electrons, thus provides an alternate approach for selective conversion of oxygenates.

References

1. Gallezot, P., *Conversion of biomass to selected chemical products.* Chemical Society Reviews, 2012. **41**(4): p. 1538-1558.
2. CHERUBINI, F., et al., *CO2 emissions from biomass combustion for bioenergy: atmospheric decay and contribution to global warming.* GCB Bioenergy, 2011. **3**(5): p. 413-426.
3. Alonso, D.M., J.Q. Bond, and J.A. Dumesic, *Catalytic conversion of biomass to biofuels.* Green Chemistry, 2010. **12**(9): p. 1493-1513.
4. Huber, G.W., S. Iborra, and A. Corma, *Synthesis of Transportation Fuels from Biomass: Chemistry, Catalysts, and Engineering.* Chemical Reviews, 2006. **106**(9): p. 4044-4098.
5. Resasco, D.E., *Furfurals as chemical platform for biofuels production. Solid Waste as a Renewable Resource: Methodologies*. 2011. 103.
6. Hayes, D.J., *An examination of biorefining processes, catalysts and challenges.* Catalysis Today, 2009. **145**(1): p. 138-151.
7. Bridgwater, A.V., D. Meier, and D. Radlein, *An overview of fast pyrolysis of biomass.* Organic Geochemistry, 1999. **30**(12): p. 1479-1493.
8. Bridgwater, A.V., *Renewable fuels and chemicals by thermal processing of biomass.* Chemical Engineering Journal, 2003. **91**(2): p. 87-102.
9. van der Stelt, M.J.C., et al., *Biomass upgrading by torrefaction for the production of biofuels: A review.* Biomass and Bioenergy, 2011. **35**(9): p. 3748-3762.
10. Zheng, A., et al., *Effect of Torrefaction Temperature on Product Distribution from Two-Staged Pyrolysis of Biomass.* Energy & Fuels, 2012. **26**(5): p. 2968-2974.
11. Waters, C.L., *Understanding thermochemical process and feedstock compositional impacts on strategies to control pyrolysis and torrefaction product distributions / by Christopher Lee Waters*. 2016, Norman, Oklahoma : University of Oklahoma.
12. Bjerkaas, D.J., *Adsorption of biomass torrefaction vapors on activated carbon.* Master thesis, University. of Oklahoma, 2017.
13. Herron, J.A., et al., *A Systems-Level Roadmap for Biomass Thermal Fractionation and Catalytic Upgrading Strategies.* Energy Technology, 2017. **5**(1): p. 130-150.
14. Pham, T.N., D. Shi, and D.E. Resasco, *Evaluating strategies for catalytic upgrading of pyrolysis oil in liquid phase.* Applied Catalysis B: Environmental, 2014. **145**: p. 10-23.
15. Gumidyala, A., T. Sooknoi, and S. Crossley, *Selective ketonization of acetic acid over HZSM-5: The importance of acyl species and the influence of water.* Journal of Catalysis, 2016. **340**: p. 76-84.
16. Zhang, L., et al., *Synthesis of C4 and C8 Chemicals from Ethanol on MgO-Incorporated Faujasite Catalysts with Balanced Confinement Effects and Basicity.* ChemSusChem, 2016. **9**(7): p. 736-748.
17. Sanna, A., T.P. Vispute, and G.W. Huber, *Hydrodeoxygenation of the aqueous fraction of bio-oil with Ru/C and Pt/C catalysts.* Applied Catalysis B: Environmental, 2015. **165**: p. 446-456.
18. Nie, L. and D.E. Resasco, *Kinetics and mechanism of m-cresol hydrodeoxygenation on a Pt/SiO2 catalyst.* Journal of Catalysis, 2014. **317**: p. 22-29.
19. Resasco, D.E., B. Wang, and D. Sabatini, *Distributed processes for biomass conversion could aid UN Sustainable Development Goals.* Nature Catalysis, 2018. **1**(10): p. 731-735.

20. Cho, H.J., et al., *Zeolite-Encapsulated Pt Nanoparticles for Tandem Catalysis.* Journal of the American Chemical Society, 2018. **140**(41): p. 13514-13520.
21. Pang, S.H., et al., *Directing reaction pathways by catalyst active-site selection using self-assembled monolayers.* Nature Communications, 2013. **4**: p. 2448.
22. Deng, Y., et al., *Solvent Tunes the Selectivity of Hydrogenation Reaction over α-MoC Catalyst.* Journal of the American Chemical Society, 2018. **140**(43): p. 14481-14489.
23. Kunkes, E.L., et al., *Catalytic Conversion of Biomass to Monofunctional Hydrocarbons and Targeted Liquid-Fuel Classes.* Science, 2008. **322**(5900): p. 417-421.
24. Chen, S., et al., *How Catalysts and Experimental Conditions Determine the Selective Hydroconversion of Furfural and 5-Hydroxymethylfurfural.* Chemical Reviews, 2018. **118**(22): p. 11023-11117.
25. Liu, S., et al., *Renewable lubricants with tailored molecular architecture.* Science advances, 2019. **5**(2): p. eaav5487-eaav5487.
26. Motagamwala, A.H., et al., *Toward biomass-derived renewable plastics: Production of 2,5-furandicarboxylic acid from fructose.* Science advances, 2018. **4**(1): p. eaap9722-eaap9722.
27. Mohanty, A.K., et al., *Composites from renewable and sustainable resources: Challenges and innovations.* Science, 2018. **362**(6414): p. 536.
28. Sitthisa, S., W. An, and D.E. Resasco, *Selective conversion of furfural to methylfuran over silica-supported NiFe bimetallic catalysts.* Journal of Catalysis, 2011. **284**(1): p. 90-101.
29. Pushkarev, V.V., et al., *High Structure Sensitivity of Vapor-Phase Furfural Decarbonylation/Hydrogenation Reaction Network as a Function of Size and Shape of Pt Nanoparticles.* Nano Letters, 2012. **12**(10): p. 5196-5201.
30. Xia, Y., et al., *Shape-Controlled Synthesis of Metal Nanocrystals: Simple Chemistry Meets Complex Physics?* Angewandte Chemie International Edition, 2009. **48**(1): p. 60-103.
31. Yu, W., et al., *Theoretical and experimental studies of the adsorption geometry and reaction pathways of furfural over FeNi bimetallic model surfaces and supported catalysts.* Journal of Catalysis, 2014. **317**: p. 253-262.
32. Schroeder, U. and L. De Verdier, *ChemInform Abstract: Influence of Oxygen and Iron in the Liquid-Phase Hydrogenation of . alpha.,β-Unsaturated Aldehydes.* ChemInform, 1993. **24**(45).
33. Claus, P., *Heterogeneously catalysed hydrogenation using gold catalysts.* Applied Catalysis A: General, 2005. **291**(1): p. 222-229.
34. Wang, S., V. Vorotnikov, and D.G. Vlachos, *Coverage-Induced Conformational Effects on Activity and Selectivity: Hydrogenation and Decarbonylation of Furfural on Pd(111).* ACS Catalysis, 2015. **5**(1): p. 104-112.
35. Liu, S., et al., *One-pot selective conversion of furfural into 1,5-pentanediol over a Pd-added Ir–ReOx/SiO2 bifunctional catalyst.* Green Chemistry, 2014. **16**(2): p. 617-626.
36. Sitthisa, S., et al., *Conversion of furfural and 2-methylpentanal on Pd/SiO2 and Pd-Cu/SiO2 catalysts.* Journal of Catalysis, 2011. **280**(1): p. 17-27.
37. Badia, A., et al., *Self-Assembled Monolayers on Gold Nanoparticles.* Chemistry – A European Journal, 1996. **2**(3): p. 359-363.
38. Agmon, N., *The Grotthuss mechanism.* Chemical Physics Letters, 1995. **244**(5): p. 456-462.

39. Nørskov, J.K., et al., *Density functional theory in surface chemistry and catalysis.* Proceedings of the National Academy of Sciences, 2011. **108**(3): p. 937.
40. Temel, B., et al., *Does phenomenological kinetics provide an adequate description of heterogeneous catalytic reactions?* The Journal of Chemical Physics, 2007. **126**(20): p. 204711.
41. Kandoi, S., et al., *Prediction of Experimental Methanol Decomposition Rates on Platinum from First Principles.* Topics in Catalysis, 2006. **37**(1): p. 17-28.
42. Behm, R.J., et al., *Adsorption of Co on Pd(100).* Journal of Chemical Physics, 1980. **73**(6): p. 2984-2995.
43. Purtell, R.J., et al., *Molecular Adsorbate Structures from Angular-Resolved Photoemission - Ammonia on Ir(111).* Physical Review Letters, 1980. **44**(19): p. 1279-1281.
44. Bao, S., et al., *Following the Changes in Local Geometry Associated with a Surface-Reaction - the Dehydrogenation of Adsorbed Ethylene.* Journal of Physics-Condensed Matter, 1994. **6**(6): p. L93-L98.
45. Batteas, J.D., et al., *A Tensor Leed Analysis of the Rh(110)-P2mg(2x1)-2co Structure.* Surface Science, 1994. **313**(3): p. 341-348.
46. Held, G. and D. Menzel, *The Structure of the P(Root-3x-Root-3) R30-Degrees Bilayer of D2o on Ru(001).* Surface Science, 1994. **316**(1-2): p. 92-102.
47. Kim, Y.J., et al., *Chemisorption geometry of NO on Rh(111) by X-ray photoelectron diffraction.* Surface Science, 1996. **359**(1-3): p. 269-279.
48. Lundgren, E., et al., *Surface x-ray-diffraction study of the Rh(111)+(2x2)-3CO structure.* Physical Review B, 1999. **59**(8): p. 5876-5880.
49. Sayago, D.I., et al., *Bond lengths and bond strengths in weak and strong chemisorption: N-2, CO, and CO/H on nickel surfaces.* Physical Review Letters, 2003. **90**(11).
50. Bradley, M.K., et al., *Methoxy Species on Cu(110): Understanding the Local Structure of a Key Catalytic Reaction Intermediate.* Physical Review Letters, 2010. **105**(8).
51. Kreikemeyer-Lorenzo, D., et al., *Face-Dependent Bond Lengths in Molecular Chemisorption: The Formate Species on Cu(111) and Cu(110).* Physical Review Letters, 2011. **107**(4).
52. Zheleva, Z.V., T. Eralp, and G. Held, *Complete Experimental Structure Determination of the p(3 x 2)pg Phase of Glycine on Cu{110}.* Journal of Physical Chemistry C, 2012. **116**(1): p. 618-625.
53. Woodruff, D.P., *The structure of surfaces: what do we know and what would we like to know?* Journal of Physics-Condensed Matter, 2010. **22**(8).
54. Flechtner, K., et al., *NO-induced reversible switching of the electronic interaction between a porphyrin-coordinated cobalt ion and a silver surface.* Journal of the American Chemical Society, 2007. **129**(40): p. 12110-+.
55. Hieringer, W., et al., *The Surface Trans Effect: Influence of Axial Ligands on the Surface Chemical Bonds of Adsorbed Metalloporphyrins.* Journal of the American Chemical Society, 2011. **133**(16): p. 6206-6222.
56. Coperet, C., et al., *Homogeneous and heterogeneous catalysis: Bridging the gap through surface organometallic chemistry.* Angewandte Chemie-International Edition, 2003. **42**(2): p. 156-181.

57. Palomares, E., et al., *State selective electron injection in non-aggregated titanium phthalocyanine sensitised nanocrystalline TiO2 films.* Chemical Communications, 2004(18): p. 2112-2113.
58. Bortolotti, C.A., et al., *A surface-immobilized cytochrome c variant provides a pH-controlled molecular switch.* Chemical Science, 2012. **3**(3): p. 807-810.
59. Auwaerter, W., et al., *Porphyrins at interfaces.* Nature Chemistry, 2015. **7**(2): p. 105-120.
60. Gottfried, J.M., *Surface chemistry of porphyrins and phthalocyanines.* Surface Science Reports, 2015. **70**(3): p. 259-379.
61. Hulsken, B., et al., *Real-time single-molecule imaging of oxidation catalysis at a liquid-solid interface.* Nature Nanotechnology, 2007. **2**(5): p. 285-289.
62. Murphy, B.E., et al., *Homolytic Cleavage of Molecular Oxygen by Manganese Porphyrins Supported on Ag(111).* Acs Nano, 2014. **8**(5): p. 5190-5198.
63. Duncan, D.A., et al., *Immobilised molecular catalysts and the role of the supporting metal substrate.* Chemical Communications, 2015. **51**(46): p. 9483-9486.
64. Waeckerlin, C., et al., *Controlling spins in adsorbed molecules by a chemical switch.* Nature Communications, 2010. **1**.
65. Ballav, N., et al., *Emergence of On-Surface Magnetochemistry.* Journal of Physical Chemistry Letters, 2013. **4**(14): p. 2303-2311.
66. Vaughan, O.P.H., et al., *A chemically switchable molecular pinwheel.* Angewandte Chemie-International Edition, 2006. **45**(23): p. 3779-3781.
67. Cho, W.J., et al., *Chromium Porphyrin Arrays As Spintronic Devices.* Journal of the American Chemical Society, 2011. **133**(24): p. 9364-9369.
68. Dougherty, D.B., et al., *Coverage-dependent surface magnetism of iron phthalocyanine on an O-Fe(110) surface.* Physical Review B, 2014. **90**(4).
69. Bohrer, F.I., et al., *Gas sensing mechanism in chemiresistive cobalt and metal-free phthalocyanine thin films.* Journal of the American Chemical Society, 2007. **129**(17): p. 5640-5646.
70. Seufert, K., W. Auwaerter, and J.V. Barth, *Discriminative Response of Surface-Confined Metalloporphyrin Molecules to Carbon and Nitrogen Monoxide.* Journal of the American Chemical Society, 2010. **132**(51): p. 18141-18146.
71. Sedona, F., et al., *Tuning the catalytic activity of Ag(110)-supported Fe phthalocyanine in the oxygen reduction reaction.* Nature Materials, 2012. **11**(11): p. 970-977.
72. Schnadt, J., et al., *Revisiting the structure of the p(4x4) surface oxide on Ag(111).* Physical Review Letters, 2006. **96**(14).
73. Gronbeck, H. and M. Odelius, *Photoemission core-level shifts reveal the thiolate-Au(111) interface.* Physical Review B, 2010. **82**(8).
74. Mercurio, G., et al., *Structure and Energetics of Azobenzene on Ag(111): Benchmarking Semiempirical Dispersion Correction Approaches.* Physical Review Letters, 2010. **104**(3).
75. Qiao, J., et al., *A review of catalysts for the electroreduction of carbon dioxide to produce low-carbon fuels.* Chemical Society Reviews, 2014. **43**(2): p. 631-675.
76. den Boer, D., et al., *Detection of different oxidation states of individual manganese porphyrins during their reaction with oxygen at a solid/liquid interface.* Nature Chemistry, 2013. **5**(7): p. 621-627.
77. Gutzler, R., et al., *Mimicking Enzymatic Active Sites on Surfaces for Energy Conversion Chemistry.* Accounts of Chemical Research, 2015. **48**(7): p. 2132-2139.

78. Gopakumar, T.G., et al., *Electron-Induced Spin Crossover of Single Molecules in a Bilayer on Gold.* Angewandte Chemie-International Edition, 2012. **51**(25): p. 6262-6266.
79. Jiang, S., et al., *Real-time electrical detection of nitric oxide in biological systems with sub-nanomolar sensitivity.* Nature Communications, 2013. **4**.
80. Auwaerter, W., et al., *Site-specific electronic and geometric interface structure of Co-tetraphenyl-porphyrin layers on Ag(111).* Physical Review B, 2010. **81**(24).
81. Floreano, L., et al., *Periodic arrays of Cu-phthalocyanine chains on Au(110).* Journal of Physical Chemistry C, 2008. **112**(29): p. 10794-10802.
82. Hartley, F.R., *Cis- Effect of Ligands and Trans-Effects of Ligands.* Chemical Society Reviews, 1973. **2**(2): p. 163-179.
83. Pinter, B., et al., *trans effect and trans influence: importance of metal mediated ligand-ligand repulsion.* Physical Chemistry Chemical Physics, 2013. **15**(40): p. 17354-17365.
84. Coe, B.J. and S.J. Glenwright, *Trans-effects in octahedral transition metal complexes.* Coordination Chemistry Reviews, 2000. **203**: p. 5-80.
85. Waeckerlin, C., et al., *On-surface coordination chemistry of planar molecular spin systems: novel magnetochemical effects induced by axial ligands.* Chemical Science, 2012. **3**(11): p. 3154-3160.
86. Woodruff, D.P., *Surface structure determination using x-ray standing waves.* Reports on Progress in Physics, 2005. **68**(4): p. 743-798.
87. Isvoranu, C., et al., *Ammonia adsorption on iron phthalocyanine on Au(111): Influence on adsorbate-substrate coupling and molecular spin.* Journal of Chemical Physics, 2011. **134**(11).
88. Fisher, C.J., et al., *Non-dipole photoemission effects in x-ray standing wavefield determination of surface structure.* Journal of Physics-Condensed Matter, 1998. **10**(35): p. L623-L629.
89. Rochford, L.A., et al., *Controlling templating effects at the organic/inorganic interface using (111) oriented copper iodide.* Journal of Materials Chemistry C, 2014. **2**(30): p. 6056-6060.
90. Bobaru, S.C., et al., *Structural Properties of Iron Phtalocyanines on Ag(111): From the Submonolayer to Monolayer Range.* Journal of Physical Chemistry C, 2011. **115**(13): p. 5875-5879.
91. Kresse, G. and J. Furthmuller, *Efficient iterative schemes for ab initio total-energy calculations using a plane-wave basis set.* Physical Review B, 1996. **54**(16): p. 11169-11186.
92. Perdew, J.P., K. Burke, and M. Ernzerhof, *Generalized gradient approximation made simple.* Physical Review Letters, 1996. **77**(18): p. 3865-3868.
93. Blochl, P.E., *Projector Augmented-Wave Method.* Physical Review B, 1994. **50**(24): p. 17953-17979.
94. Kresse, G. and D. Joubert, *From ultrasoft pseudopotentials to the projector augmented-wave method.* Physical Review B, 1999. **59**(3): p. 1758-1775.
95. Grimme, S., S. Ehrlich, and L. Goerigk, *Effect of the Damping Function in Dispersion Corrected Density Functional Theory.* Journal of Computational Chemistry, 2011. **32**(7): p. 1456-1465.
96. Klimes, J., D.R. Bowler, and A. Michaelides, *Van der Waals density functionals applied to solids.* Physical Review B, 2011. **83**(19).

97. Klimes, J., D.R. Bowler, and A. Michaelides, *Chemical accuracy for the van der Waals density functional.* Journal of Physics-Condensed Matter, 2010. **22**(2).
98. Barth, J.V., *Fresh perspectives for surface coordination chemistry.* Surface Science, 2009. **603**(10-12): p. 1533-1541.
99. Schlickum, U., et al., *Metal-organic honeycomb nanomeshes with tunable cavity size.* Nano Letters, 2007. **7**(12): p. 3813-3817.
100. Seitsonen, A.P., et al., *Density functional theory analysis of carboxylate-bridged diiron units in two-dimensional metal-organic grids.* Journal of the American Chemical Society, 2006. **128**(17): p. 5634-5635.
101. Huber, G.W., R.D. Cortright, and J.A. Dumesic, *Renewable alkanes by aqueous-phase reforming of biomass-derived oxygenates.* Angew. Chem., Int. Ed., 2004. **43**(12): p. 1549-1551.
102. Davda, R.R., et al., *A review of catalytic issues and process conditions for renewable hydrogen and alkanes by aqueous-phase reforming of oxygenated hydrocarbons over supported metal catalysts.* Appl. Catal., B, 2005. **56**(1-2): p. 171-186.
103. Christensen, E., et al., *Renewable Oxygenate Blending Effects on Gasoline Properties.* Energy Fuels, 2011. **25**(10): p. 4723-4733.
104. Alonso, D.M., J.Q. Bond, and J.A. Dumesic, *Catalytic conversion of biomass to biofuels.* Green Chem., 2010. **12**(9): p. 1493-1513.
105. Corma, A., S. Iborra, and A. Velty, *Chemical routes for the transformation of biomass into chemicals.* Chemical Reviews, 2007. **107**(6): p. 2411-2502.
106. Van de Vyver, S. and Y. Roman-Leshkov, *Emerging catalytic processes for the production of adipic acid.* Catal. Sci. Technol., 2013. **3**(6): p. 1465-1479.
107. Fegyverneki, D., et al., *Gamma-valerolactone-based solvents.* Tetrahedron, 2010. **66**(5): p. 1078-1081.
108. Wettstein, S.G., et al., *Production of levulinic acid and gamma-valerolactone (GVL) from cellulose using GVL as a solvent in biphasic systems.* Energy & Environmental Science, 2012. **5**(8): p. 8199-8203.
109. Bond, J.Q., et al., *Integrated Catalytic Conversion of gamma-Valerolactone to Liquid Alkenes for Transportation Fuels.* Science, 2010. **327**(5969): p. 1110-1114.
110. Palkovits, R., *Pentenoic Acid Pathways for Cellulosic Biofuels.* Angewandte Chemie-International Edition, 2010. **49**(26): p. 4336-4338.
111. Wright, W.R.H. and R. Palkovits, *Development of Heterogeneous Catalysts for the Conversion of Levulinic Acid to gamma-Valerolactone.* Chemsuschem, 2012. **5**(9): p. 1657-1667.
112. Alonso, D.M., S.G. Wettstein, and J.A. Dumesic, *Gamma-valerolactone, a sustainable platform molecule derived from lignocellulosic biomass.* Green Chemistry, 2013. **15**(3): p. 584-595.
113. Mehdi, H., et al., *Integration of homogeneous and heterogeneous catalytic processes for a multi-step conversion of biomass: From sucrose to levulinic acid, gamma-valerolactone, 1,4-pentanediol, 2-methyl-tetrahydrofuran, and alkanes.* Topics in Catalysis, 2008. **48**(1-4): p. 49-54.
114. Resasco, D.E., et al., *5. Furfurals as chemical platform for biofuels production*, in *Solid Waste as a Renewable Resource: Methodologies*, A.J.F. Albanese and M.P. Ruiz, Editors. 2011. p. 103.

115. Lange, J.-P., et al., *Furfural-a Promising Platform for Lignocellulosic Biofuels.* ChemSusChem, 2012. **5**(1): p. 150-166.
116. Xing, R., W. Qi, and G.W. Huber, *Production of furfural and carboxylic acids from waste aqueous hemicellulose solutions from the pulp and paper and cellulosic ethanol industries.* Energy & Environmental Science, 2011. **4**(6): p. 2193-2205.
117. Bui, L., et al., *Domino Reaction Catalyzed by Zeolites with BrOnsted and Lewis Acid Sites for the Production of -Valerolactone from Furfural.* Angewandte Chemie-International Edition, 2013. **52**(31): p. 8022-8025.
118. Bond, J.Q., et al., *gamma-Valerolactone Ring-Opening and Decarboxylation over SiO2/Al2O3 in the Presence of Water.* Langmuir, 2010. **26**(21): p. 16291-16298.
119. Christian, R.V., H.D. Brown, and R.M. Hixon, *Derivatives of Gamma-Valerolactone, 1,4-Pentanediol and 1,4-Di-(Beta-Cyanoethoxy)-Pentane.* Journal of the American Chemical Society, 1947. **69**(8): p. 1961-1963.
120. Geilen, F.M.A., et al., *Selective and Flexible Transformation of Biomass-Derived Platform Chemicals by a Multifunctional Catalytic System.* Angewandte Chemie-International Edition, 2010. **49**(32): p. 5510-5514.
121. Al-Shaal, M.G., A. Dzierbinski, and R. Palkovits, *Solvent-free gamma-valerolactone hydrogenation to 2-methyltetrahydrofuran catalysed by Ru/C: a reaction network analysis.* Green Chemistry, 2014. **16**(3): p. 1358-1364.
122. Rozenblit, A., et al., *Reaction mechanism of aqueous-phase conversion of gamma-valerolactone (GVL) over a Ru/C catalyst.* Journal of Energy Chemistry, 2016. **25**(6): p. 1008-1014.
123. Du, X.-L., et al., *Tunable copper-catalyzed chemoselective hydrogenolysis of biomass-derived gamma-valerolactone into 1,4-pentanediol or 2-methyltetrahydrofuran.* Green Chemistry, 2012. **14**(4): p. 935-939.
124. Deimel, P.S., et al., *Direct quantitative identification of the "surface trans-effect".* Chemical Science, 2016. **7**(9): p. 5647-5656.
125. Henkelman, G., B.P. Uberuaga, and H. Jonsson, *A climbing image nudged elastic band method for finding saddle points and minimum energy paths.* Journal of Chemical Physics, 2000. **113**(22): p. 9901-9904.
126. Henkelman, G. and H. Jonsson, *Improved tangent estimate in the nudged elastic band method for finding minimum energy paths and saddle points.* Journal of Chemical Physics, 2000. **113**(22): p. 9978-9985.
127. Yin, A.-X., et al., *Ru Nanocrystals with Shape-Dependent Surface-Enhanced Raman Spectra and Catalytic Properties: Controlled Synthesis and DFT Calculations.* Journal of the American Chemical Society, 2012. **134**(50): p. 20479-20489.
128. van Santen, R.A. and I. Tranca, *How molecular is the chemisorptive bond?* Physical Chemistry Chemical Physics, 2016. **18**(31): p. 20868-20894.
129. Mironenko, A.V., et al., *Ring Activation of Furanic Compounds on Ruthenium-Based Catalysts.* Journal of Physical Chemistry C, 2015. **119**(11): p. 6075-6085.
130. Madon, R.J. and E. Iglesia, *Catalytic reaction rates in thermodynamically non-ideal systems.* Journal of Molecular Catalysis a-Chemical, 2000. **163**(1-2): p. 189-204.
131. Mellmer, M.A., et al., *Solvent Effects in Acid-Catalyzed Biomass Conversion Reactions.* Angewandte Chemie-International Edition, 2014. **53**(44): p. 11872-11875.

132. Yoon, Y., et al., *First-Principles Study of Phenol Hydrogenation on Pt and Ni Catalysts in Aqueous Phase.* Journal of the American Chemical Society, 2014. **136**(29): p. 10287-10298.
133. Hibbitts, D.D., et al., *Mechanistic Role of Water on the Rate and Selectivity of Fischer-Tropsch Synthesis on Ruthenium Catalysts.* Angewandte Chemie-International Edition, 2013. **52**(47): p. 12273-12278.
134. Guerbuez, E.I., D.D. Hibbitts, and E. Iglesia, *Kinetic and Mechanistic Assessment of Alkanol/Alkanal Decarbonylation and Deoxygenation Pathways on Metal Catalysts.* Journal of the American Chemical Society, 2015. **137**(37): p. 11984-11995.
135. Carpenter, B.K., J.N. Harvey, and A.J. Orr-Ewing, *The Study of Reactive Intermediates in Condensed Phases.* Journal of the American Chemical Society, 2016. **138**(14): p. 4695-4705.
136. Chheda, J.N., G.W. Huber, and J.A. Dumesic, *Liquid-phase catalytic processing of biomass-derived oxygenated hydrocarbons to fuels and chemicals.* Angewandte Chemie-International Edition, 2007. **46**(38): p. 7164-7183.
137. Struebing, H., et al., *Computer-aided molecular design of solvents for accelerated reaction kinetics.* Nature Chemistry, 2013. **5**(11): p. 952-957.
138. Mellmer, M.A., et al., *Solvent-enabled control of reactivity for liquid-phase reactions of biomass-derived compounds.* Nature Catalysis, 2018. **1**(3): p. 199-207.
139. Crossley, S., et al., *Solid Nanoparticles that Catalyze Biofuel Upgrade Reactions at the Water/Oil Interface.* Science, 2010. **327**(5961): p. 68-72.
140. Franck, J. and E. Rabinowitsch, *Some remarks about free radicals and the photochemistry of solutions.* Transactions of the Faraday Society, 1934. **30**: p. 120-130.
141. Sicinska, D., D.G. Truhlar, and P. Paneth, *Solvent-dependent transition states for decarboxylations.* Journal of the American Chemical Society, 2001. **123**(31): p. 7683-7686.
142. Saavedra, J., et al., *Controlling activity and selectivity using water in the Au-catalysed preferential oxidation of CO in H-2.* Nature Chemistry, 2016. **8**(6): p. 585-590.
143. Saavedra, J., et al., *The critical role of water at the gold-titania interface in catalytic CO oxidation.* Science, 2014. **345**(6204): p. 1599-1602.
144. Yoon, Y., et al., *First-Principles Study of Phenol Hydrogenation on Pt and Ni Catalysts in Aqueous Phase.* Journal of the American Chemical Society, 2014. **136**(29): p. 10287-10298.
145. Lange, J.P., et al., *Furfural—a promising platform for lignocellulosic biofuels.* ChemSusChem, 2012. **5**(1): p. 150-166.
146. Resasco, D.E., B. Wang, and D. Sabatini, *Distributed processes for biomass conversion could aid UN Sustainable Development Goals.* Nature Catalysis, 2018. **1**(10): p. 731.
147. Sitthisa, S. and D.E. Resasco, *Hydrodeoxygenation of Furfural Over Supported Metal Catalysts: A Comparative Study of Cu, Pd and Ni.* Catalysis Letters, 2011. **141**(6): p. 784-791.
148. Panagiotopoulou, P., N. Martin, and D.G. Vlachos, *Effect of hydrogen donor on liquid phase catalytic transfer hydrogenation of furfural over a Ru/RuO2/C catalyst.* Journal of Molecular Catalysis a-Chemical, 2014. **392**: p. 223-228.
149. Maldonado, G.M.G., et al., *Experimental and theoretical studies of the acid-catalyzed conversion of furfuryl alcohol to levulinic acid in aqueous solution.* Energy & Environmental Science, 2012. **5**(5): p. 6981-6989.

150. Serrano-Ruiz, J.C., R. Luque, and A. Sepulveda-Escribano, *Transformations of biomass-derived platform molecules: from high added-value chemicals to fuels via aqueous-phase processing.* Chemical Society Reviews, 2011. **40**(11): p. 5266-5281.
151. Vorotnikov, V., G. Mpourmpakis, and D.G. Vlachos, *DFT Study of Furfural Conversion to Furan, Furfuryl Alcohol, and 2-Methylfuran on Pd(111).* Acs Catalysis, 2012. **2**(12): p. 2496-2504.
152. Pang, S.H. and J.W. Medlin, *Adsorption and Reaction of Furfural and Furfuryl Alcohol on Pd(111): Unique Reaction Pathways for Multifunctional Reagents.* Acs Catalysis, 2011. **1**(10): p. 1272-1283.
153. Wang, S.G., V. Vorotnikov, and D.G. Vlachos, *Coverage-Induced Conformational Effects on Activity and Selectivity: Hydrogenation and Decarbonylation of Furfural on Pd(111).* Acs Catalysis, 2015. **5**(1): p. 104-112.
154. Pang, S.H., et al., *Effects of Thiol Modifiers on the Kinetics of Furfural Hydrogenation over Pd Catalysts.* Acs Catalysis, 2014. **4**(9): p. 3123-3131.
155. Pang, S.H., et al., *Directing reaction pathways by catalyst active-site selection using self-assembled monolayers.* Nature Communications, 2013. **4**: p. 2448.
156. Sitthisa, S., W. An, and D.E. Resasco, *Selective conversion of furfural to methylfuran over silica-supported Ni-Fe bimetallic catalysts.* Journal of Catalysis, 2011. **284**(1): p. 90-101.
157. Fulajtarova, K., et al., *Aqueous phase hydrogenation of furfural to furfuryl alcohol over Pd-Cu catalysts.* Applied Catalysis a-General, 2015. **502**: p. 78-85.
158. Merlo, A.B., et al., *Bimetallic PtSn catalyst for the selective hydrogenation of furfural to furfuryl alcohol in liquid-phase.* Catalysis Communications, 2009. **10**(13): p. 1665-1669.
159. Chen, X.F., et al., *Highly selective hydrogenation of furfural to furfuryl alcohol over Pt nanoparticles supported on g-C3N4 nanosheets catalysts in water.* Scientific Reports, 2016. **6**: p. 28558.
160. Vaidya, P.D. and V.V. Mahajani, *Kinetics of liquid-phase hydrogenation of furfuraldehyde to furfuryl alcohol over a Pt/C catalyst.* Industrial & Engineering Chemistry Research, 2003. **42**(17): p. 3881-3885.
161. Lee, J.C., Y. Xu, and G.W. Huber, *High-throughput screening of monometallic catalysts for aqueous-phase hydrogenation of biomass-derived oxygenates.* Applied Catalysis B-Environmental, 2013. **140**: p. 98-107.
162. Frainier, L.J. and H.H. Fineberg, *Copper chromite catalyst for preparation of furfuryl alcohol from furfural*. 1979: US.
163. Villaverde, M.M., et al., *Selective liquid-phase hydrogenation of furfural to furfuryl alcohol over Cu-based catalysts.* Catalysis Today, 2013. **213**: p. 87-92.
164. Singh, U.K. and M.A. Vannice, *Kinetics of liquid-phase hydrogenation reactions over supported metal catalysts - a review.* Applied Catalysis a-General, 2001. **213**(1): p. 1-24.
165. Grimme, S., et al., *A consistent and accurate ab initio parametrization of density functional dispersion correction (DFT-D) for the 94 elements H-Pu.* Journal of Chemical Physics, 2010. **132**(15): p. 154104.
166. Henkelman, G. and H. Jonsson, *A dimer method for finding saddle points on high dimensional potential surfaces using only first derivatives.* Journal of Chemical Physics, 1999. **111**(15): p. 7010-7022.
167. Mukherjee, S. and M.A. Vannice, *Solvent effects in liquid-phase reactions II. Kinetic modeling for citral hydrogenation.* Journal of Catalysis, 2006. **243**(1): p. 131-148.

168. D'Souza, V.T., V.K. Iyer, and H.H. Szmant, *Thiol-olefin cooxidation (TOCO) reaction. 8. Solvent effects in the oxidation of some thiols with molecular oxygen.* The Journal of Organic Chemistry, 1987. **52**(9): p. 1725-1728.
169. Campbell, C.T. and J.R.V. Sellers, *The Entropies of Adsorbed Molecules.* Journal of the American Chemical Society, 2012. **134**(43): p. 18109-18115.
170. Chambers, R.P. and M. Boudart, *Lack of Dependence of Conversion on Flow Rate in Catalytic Studies.* Journal of Catalysis, 1966. **6**(1): p. 141-&.
171. Pham, T.N., D.C. Shi, and D.E. Resasco, *Evaluating strategies for catalytic upgrading of pyrolysis oil in liquid phase.* Applied Catalysis B-Environmental, 2014. **145**: p. 10-23.
172. Rajashekharam, M.V., et al., *Hydrogenation of acetophenone using a 10% Ni supported on zeolite Y catalyst: kinetics and reaction mechanism.* Catalysis Today, 1999. **48**(1-4): p. 83-92.
173. Wan, H.J., et al., *Kinetic investigations of unusual solvent effects during Ru/C catalyzed hydrogenation of model oxygenates.* Journal of Catalysis, 2014. **309**: p. 174-184.
174. Ramachandran, P.A. and R.V. Chaudhari, *Three-phase catalytic reactors*. Vol. 2. 1983: Gordan and Breach Science.
175. Nakagawa, Y., et al., *Total Hydrogenation of Furfural and 5-Hydroxymethylfurfural over Supported Pd-Ir Alloy Catalyst.* Acs Catalysis, 2014. **4**(8): p. 2718-2726.
176. Rekoske, J.E., et al., *Microkinetic Analysis of Diverse Experimental-Data for Ethylene Hydrogenation on Platinum.* Journal of Physical Chemistry, 1992. **96**(4): p. 1880-1888.
177. Dumesic, J.A., et al., *The Microkinetics of heterogeneous catalysis*. ACS professional reference book. 1993, Washington, DC: American Chemical Society. xii, 315 p.
178. Farberow, C.A., J.A. Dumesic, and M. Mavrikakis, *Density Functional Theory Calculations and Analysis of Reaction Pathways for Reduction of Nitric Oxide by Hydrogen on Pt(111).* Acs Catalysis, 2014. **4**(10): p. 3307-3319.
179. Vilekar, S.A., I. Fishtik, and R. Datta, *The steady-state kinetics of parallel reaction networks.* Chemical Engineering Science, 2010. **65**(10): p. 2921-2933.
180. Loffreda, D., et al., *Chemo-regioselectivity in heterogeneous catalysis: Competitive routes for C=O and C=C hydrogenations from a theoretical approach.* Journal of the American Chemical Society, 2006. **128**(4): p. 1316-1323.
181. Maroncelli, M., J. MacInnis, and G.R. Fleming, *Polar solvent dynamics and electron-transfer reactions.* Science, 1989. **243**(4899): p. 1674-1681.
182. Henriksen, N.E. and F.Y. Hansen, *Theories of molecular reaction dynamics: the microscopic foundation of chemical kinetics*. 2018: Oxford University Press.
183. Kibler, L.A., *Hydrogen electrocatalysis.* Chemphyschem, 2006. **7**(5): p. 985-991.
184. Agmon, N., *The Grotthuss Mechanism.* Chemical Physics Letters, 1995. **244**(5-6): p. 456-462.
185. Cukier, R.I. and D.G. Nocera, *Proton-coupled electron transfer.* Annual Review of Physical Chemistry, 1998. **49**: p. 337-369.
186. Norskov, J.K., et al., *Towards the computational design of solid catalysts.* Nature Chemistry, 2009. **1**(1): p. 37-46.
187. Sitthisa, S., et al., *Kinetics and mechanism of hydrogenation of furfural on Cu/SiO2 catalysts.* Journal of Catalysis, 2011. **277**(1): p. 1-13.
188. Chen, X., et al., *Highly selective hydrogenation of furfural to furfuryl alcohol over Pt nanoparticles supported on g-C3N4 nanosheets catalysts in water.* Scientific Reports, 2016. **6**: p. 28558.

189. Fuente-Hernández, A., et al., *Reduction of Furfural to Furfuryl Alcohol in Liquid Phase over a Biochar-Supported Platinum Catalyst.* Energies, 2017. **10**(3): p. 286.
190. Liu, L., H. Lou, and M. Chen, *Selective hydrogenation of furfural to tetrahydrofurfuryl alcohol over Ni/CNTs and bimetallic CuNi/CNTs catalysts.* International Journal of Hydrogen Energy, 2016. **41**(33): p. 14721-14731.
191. Jung, S. and E.J. Biddinger, *Electrocatalytic Hydrogenation and Hydrogenolysis of Furfural and the Impact of Homogeneous Side Reactions of Furanic Compounds in Acidic Electrolytes.* Acs Sustainable Chemistry & Engineering, 2016. **4**(12): p. 6500-6508.
192. Chadderdon, X.H., et al., *Mechanisms of Furfural Reduction on Metal Electrodes: Distinguishing Pathways for Selective Hydrogenation of Bioderived Oxygenates.* Journal of the American Chemical Society, 2017. **139**(40): p. 14120-14128.
193. Bard, A.J.F., L. R., *Electrochemical Methods: Fundamentals and Applications.* John Wiley & Sons, Inc.: New York, 2001(2nd ed.): p. 116.
194. Schmickler, W., *A unified model for electrochemical electron and ion transfer reactions.* Chemical Physics Letters, 1995. **237**(1): p. 152-160.
195. Kwon, Y., et al., *Electrocatalytic Conversion of Furanic Compounds.* Acs Catalysis, 2016. **6**(10): p. 6704-6717.
196. Kuhl, K.P., et al., *New insights into the electrochemical reduction of carbon dioxide on metallic copper surfaces.* Energy & Environmental Science, 2012. **5**(5): p. 7050-7059.
197. Shi, Y., et al., *Exploring Furfural Catalytic Conversion on Cu(111) from Computation.* Acs Catalysis, 2015. **5**(7): p. 4020-4032.
198. Green, S.K., et al., *The electrocatalytic hydrogenation of furanic compounds in a continuous electrocatalytic membrane reactor.* Green Chemistry, 2013. **15**(7): p. 1869-1879.
199. Li, Z.L., et al., *Aqueous electrocatalytic hydrogenation of furfural using a sacrificial anode.* Electrochimica Acta, 2012. **64**: p. 87-93.
200. Zhao, B., et al., *Electrocatalytic hydrogenation of furfural to furfuryl alcohol using platinum supported on activated carbon fibers.* Electrochimica Acta, 2014. **135**: p. 139-146.
201. Jung, S. and E.J. Biddinger, *Controlling Competitive Side Reactions in the Electrochemical Upgrading of Furfural to Biofuel.* Energy Technology, 2018. **6**(7): p. 1370-1379.
202. Cantu, D.C., et al., *A combined experimental and theoretical study on the activity and selectivity of the electrocatalytic hydrogenation of aldehydes.* ACS Catalysis, 2018. **8**(8): p. 7645-7658.
203. Singh, N., et al., *Electrocatalytic Hydrogenation of Phenol over Platinum and Rhodium: Unexpected Temperature Effects Resolved.* Acs Catalysis, 2016. **6**(11): p. 7466-7470.
204. Song, Y., et al., *Aqueous phase electrocatalysis and thermal catalysis for the hydrogenation of phenol at mild conditions.* Applied Catalysis B-Environmental, 2016. **182**: p. 236-246.

Appendix

A. Structural parameters and charge distribution in Chapter 2

A1.Structural parameters

The absolute heights for the FePc molecule before and after the ligation of ammonia and water are shown in Table S1, along with the corresponding coherent fractions and coherent positions. The comparable absolute heights from the DFT calculations using the functionals described above, are also reported for the center of the molecule above a hollow site, atop site and bridge site for iron phthalocyanine adsorbed on Ag(111) without any ligand (Table S2), with ligated ammonia (Table S3) and with ligated water (Table S4). Shown in Table S5 are the metal-ligand distances for chosen traditional trans-effect and surface trans-effect systems.

Ag(111)/FePc	Fe	N	C-N	C-C
F_C	0.9(1)	0.87(5)	0.9(1)	0.9(2)
P_C	0.11(1)	0.15(3)	0.20(2)	0.24(2)
D(hkl)+D(hkl)*P_H (Å)	2.61(1)	2.71(7)	2.83(5)	2.92(5)
Ag(111)/FePc/NH_3				
F_C	0.73(8)	0.9(3)	0.9(1)	0.95(11)
P_C	0.19(3)	0.21(1)	0.23(1)	0.27(1)
D(hkl)+D(hkl)*P_H (Å)	2.80(7)	2.84(2)	2.90(3)	2.98(3)
Ag(111)/FePc/H_2O				
F_C	0.75(7)	0.8(1)	0.9(1)	0.9(1)
P_C	0.14(2)	0.19(3)	0.21(1)	0.23(4)
D(hkl)+D(hkl)*P_H (Å)	2.68(4)	2.79(6)	2.84(2)	2.90(1)

Appendix Table 1 Coherent fractions (Fc) and coherent positions (Pc) found experimentally in this study for Fe, N and C atoms (C split into C-C and C-N species as identified in FIG. S1), as well as the height of the various species above bulk like termination of the Ag(111) surface. Note D(hkl) for Ag (111) is taken as 2.35 Å, and it is assumed that the molecule is over one layer spacing above the surface (otherwise unphysical results are obtained).

		Fe (Å)	N (Å)	C-N (Å)	C-C (Å)
DFT+D2-1L	Top	2.80	2.87	2.88	2.86
	HCP	2.72	2.84	2.86	2.86
	Bridge	2.71	2.83	2.85	2.86
	mean	2.74	2.85	2.86	2.86
	weighted	2.73	2.84	2.86	2.86
	std. dev.	0.05	0.02	0.02	0.00
DFT+D2-4L	Top	2.77	2.83	2.83	2.80
	HCP	2.65	2.77	2.79	2.81
	Bridge	2.63	2.76	2.78	2.80
	mean	2.68	2.79	2.80	2.80
	weighted	2.67	2.78	2.79	2.80
	std. dev.	0.08	0.04	0.03	0.01
DFT+D3	Top	2.82	2.95	2.97	3.02
	HCP	2.73	2.90	2.93	3.00
	Bridge	2.69	2.87	2.90	3.01
	mean	2.75	2.91	2.93	3.01
	weighted	2.73	2.90	2.93	3.01
	std. dev.	0.07	0.04	0.04	0.01
DFT+ optB88-VdW	Top	2.80	2.87	2.88	2.88
	HCP	2.60	2.77	2.79	2.89
	Bridge	2.59	2.74	2.77	2.90
	mean	2.66	2.79	2.81	2.89
	weighted	2.64	2.78	2.80	2.89
	std. dev.	0.12	0.07	0.06	0.01

Appendix Table 2 Absolute heights of the various components of the molecule above the Ag(111) surface as calculated for Ag(111)/FePc by DFT calculations with different methods to include the van der Waals interaction. The weighted mean is assuming that in each surface unit mesh there is

one unique atop site, two unique bridge sites and two unique hollow sites (assuming the FCC hollow site is identical to the HCP hollow site). When calculating the height of the atoms, the average height of the First layer Ag atoms has been used as the reference.

		Fe (Å)	N (Å)	C-N (Å)	C-C (Å)
DFT+D2-1L	Top	3.00	2.98	2.97	2.90
	HCP	2.90	2.92	2.93	2.89
	Bridge	2.91	2.92	2.92	2.89
	mean	2.94	2.94	2.94	2.89
	weighted	2.93	2.93	2.94	2.89
	std. dev.	0.08	0.03	0.03	0.01
DFT+D2-4L	Top	2.96	2.93	2.92	2.84
	HCP	2.84	2.86	2.86	2.83
	Bridge	2.83	2.84	2.85	2.82
	mean	2.88	2.88	2.88	2.83
	weighted	2.86	2.87	2.87	2.83
	std. dev.	0.07	0.05	0.04	0.01
DFT+D3	Top	3.14	3.11	3.11	3.08
	HCP	3.01	3.04	3.05	3.05
	Bridge	3.02	3.04	3.05	3.08
	mean	3.06	3.06	3.07	3.07
	weighted	3.04	3.05	3.06	3.07
	std. dev.	0.07	0.04	0.03	0.02
DFT+ optB88-VdW	Top	3.00	2.98	2.98	2.94
	HCP	2.85	2.89	2.91	2.96
	Bridge	2.81	2.86	2.88	2.96
	mean	2.89	2.91	2.92	2.95
	weighted	2.86	2.90	2.91	2.96
	std. dev.	0.10	0.06	0.05	0.01

Appendix Table 3 Absolute heights of the various components of the molecule above the Ag(111) surface as calculated for Ag(111)/FePc/NH3 by DFT calculations with different methods to include the van der Waals interaction. The weighted mean is assuming that in each surface unit

mesh there is one unique atop site, two unique bridge sites and two unique hollow sites (assuming the FCC hollow site is identical to the HCP hollow site). When calculating the height of the atoms, the average height of the first-Layer Ag atoms has been used as the reference.

ligand1/ FePc /ligand2	H_3N-Fe (Å)	O-Fe (Å)	ON-Fe (Å)
(NH_3)/FePc/(NH_3)	2.03	--	--
(H_2O)/FePc/(H_2O)	--	2.04	--
(H_2O)/FePc/(NH_3)	1.99	2.09	--
(NO)/FePc/(NO)	--	--	1.83
(NO)/FePc/(NH_3)	2.16	--	1.74
Ag(111)/FePc/(NH_3)	2.12[a]/2.11[b]	--	--
Ag(111)/FePc/(H_2O)	--	2.40[a]/2.45[b]	--

[a]*FePc adsorption on Ag with the Fe on top of a surface Ag atom.*

[b]*FePc adsorption on Ag with the Fe on top of a hcp site.*

Appendix Table 4 Fe – molecular ligand bond length from DFT-D2 calculations for NH3, H2O and NO trans to NH3, H2O, NO and Ag(111). A longer ligand – Fe bond length implies a stronger trans-effect of the trans-ligand.

A2.Charge redistribution maps

The charge redistribution maps, shown in FIG. 2 of the main manuscript and FIG. S2 were calculated by $\Delta\rho = \rho(A+B) - \rho(A) - \rho(B)$, that is, the electron density of the whole system $\rho(A+B)$ minus the one of each component, $\rho(A)$ and $\rho(B)$, with their atomic positions fixed in the optimized structure. For example, the label FePc(H)/Ag + NH_3 means $\Delta\rho = \rho(NH_3/FePc(H)/Ag) - \rho(FePc(H)/Ag) - \rho(NH_3)$, where $\rho(NH_3/FePc(H)/Ag)$ is the total electron density of NH_3 adsorption on FePc on Ag with the Fe located above the HCP site, and $\rho(FePc(H)/Ag)$ and $\rho(NH_3)$ are electron density of FePc(H)/Ag and NH_3 with their atoms fixed at the optimized adsorption positions for NH_3/FePc(H)/Ag. Thus, $\Delta\rho(NH_3/FePc(H)/Ag)$ displays the charge redistribution caused by adsorption of NH_3 on FePc/Ag. Similarly, FePc(H)/Ag+H_2O shows the charge redistribution induced by H_2O adsorption on FePc/Ag.

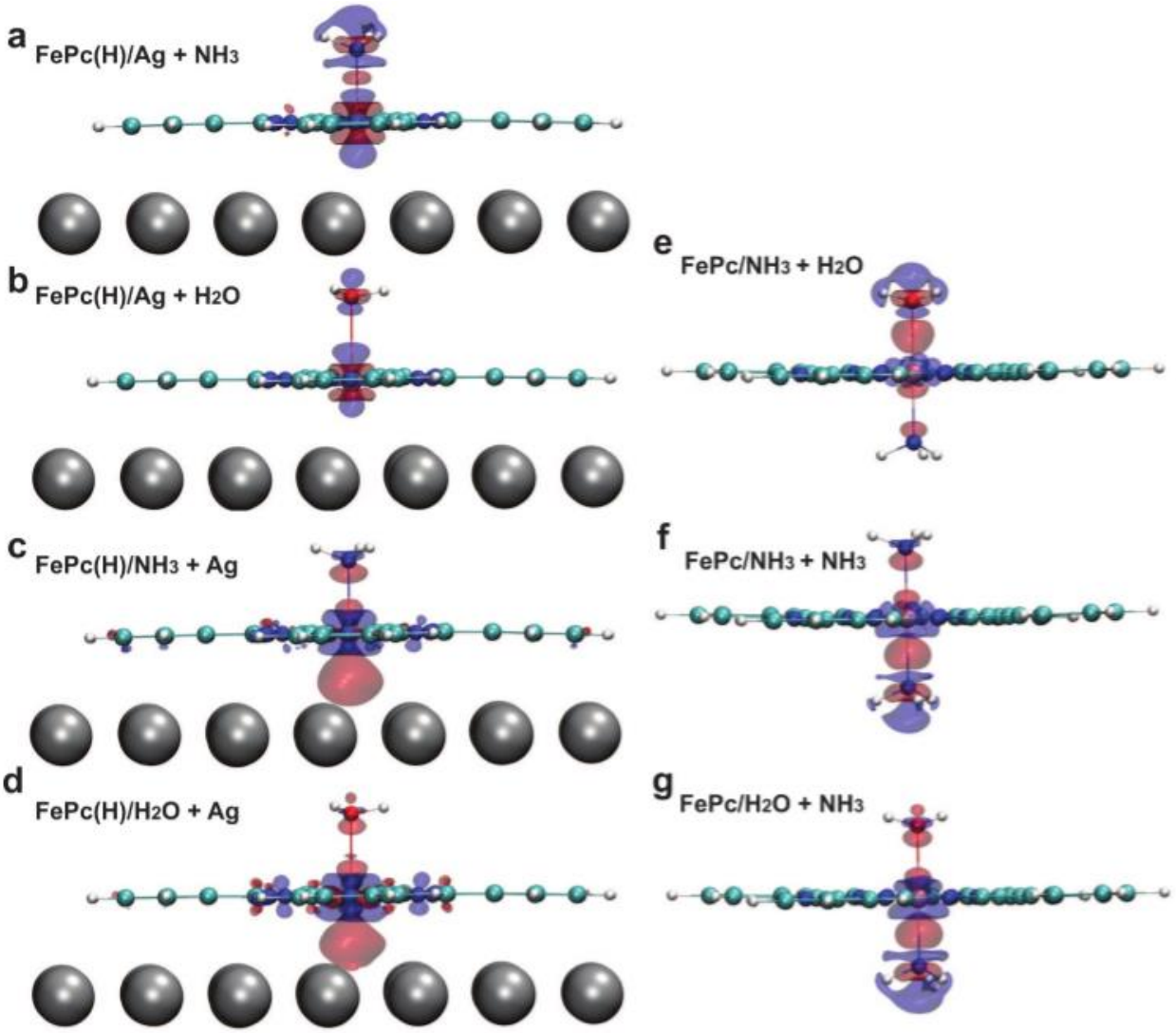

Appendix fig. 1 Calculated charge redistribution maps for introducing (a) ammonia and (b) water trans to the Ag(111) surface; Ag(111) surface trans to (c) ammonia and (d) water; ammonia trans to (g) water and (f) ammonia; and, finally, (e) water trans to ammonia. The charge density difference was plotted at an isosurface of ±0.02 eÅ-3. The red colour represents electron accumulation while blue colour shows electron depletion.

Appendix fig. 5 represents the predicted difference in the local charge density due to the introduction of a given ligand. So, in the case of FIG. S2, the plotted redistribution shows how introducing an ammonia molecule above the Fe atom of FePc adsorbed on Ag(111) results in charge accumulating in the Fe atom's d-xz and d-yz orbitals and a depletion in the Fe atom's d-z2 orbitals

A3.Electrostatic potential above the surface

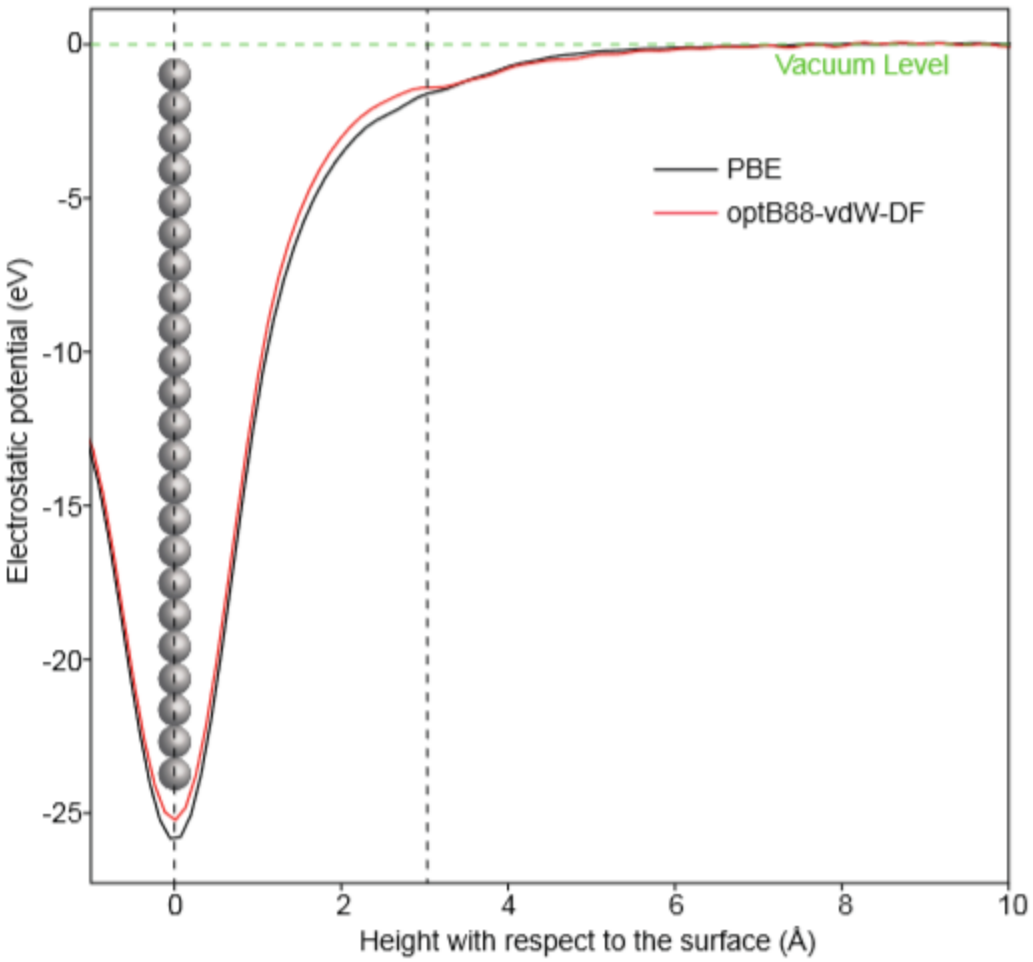

Appendix fig. 2 Calculated plane-averaged electrostatic potential above a clean Ag surface using the PBE functional (black) and the optB88-vdW-DF functional (red). Height of the Ag surface is set to zero. The vacuum level is used as the reference (green dashed line). At the molecular adsorption regime (within 3 Å above the surface, that is between the two dashed lines), optB88-vdW-DF functional calculation shows a less negative potential, corresponding to a lower local work function.

Here we use optB88-vdW-DF calculations to show the calculated electrostatic potential above a clean Ag surface, because calculations using the classical pair-wise force field potential, such as in DFT-D2 and D3 methods, of the same clean Ag surface will show no difference as compared the PBE-functional calculations. Within 3 Å above the surface (between the two black dashed lines), the difference between the electrostatic potential varies by 0.3-0.7 eV, and these two potentials both converge to the vacuum level eventually. The less negative potential of the optB88-vdW-DF calculated

Ag surface suggests a lower local work function, corresponding to a different charge distribution at the surface as compared to the PBE-calculated surface, that is a surface dipole pointing towards the surface. This lower local work function when using vdW-DF functional makes Ag a stronger trans ligand. When adding the Ag (111) surface trans to a water molecule, charge accumulation occurs at the interface. The lower local work function (an electric dipole pointing towards the surface) helps such a charge accumulation at the interface, and thus leads to a stronger interfacial binding as compared to the PBE-calculated results.

B. Reaction energy and reaction pathway of GVL in Chapter 3

B1. Adsorption conformation

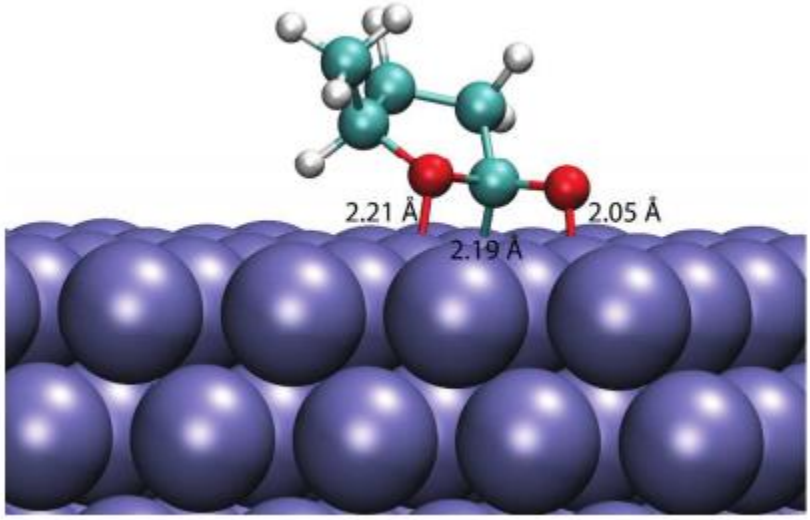

Appendix fig. 3 The most stable adsorption configuration of GVL on the Ru(0001) surface with the furanic O atom and carbonyl C and O atoms forming bonds with the Ru surface. The length of the Ru-C bond is indicated.

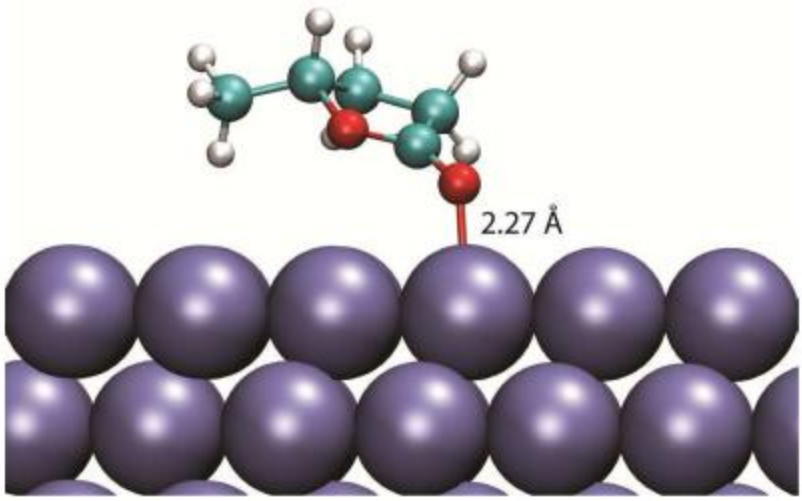

Appendix fig. 4 Adsorption of GVL on the Ru (0001) surface with the carbonyl O atom located above a surface Ru atom. The length of the Ru-C bond is indicated.

B2. Activation energies

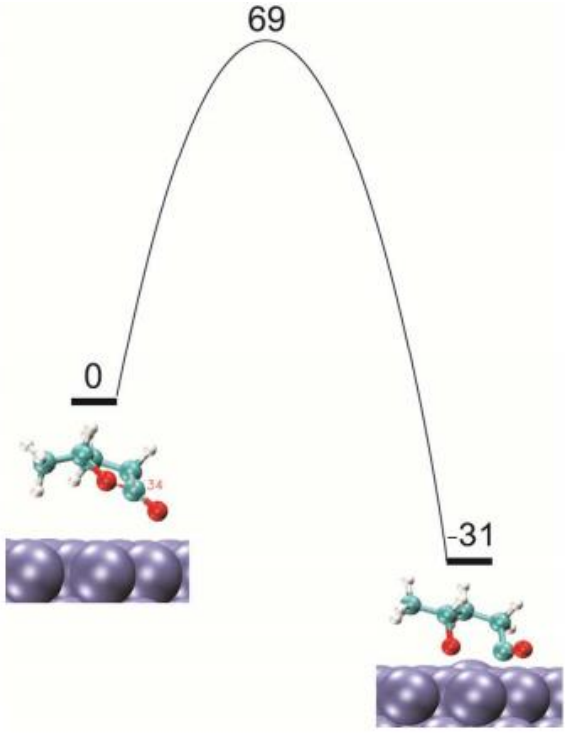

Appendix fig. 5 Ring opening of GVL adsorbed with the carbonyl O atom binding to the surface Ru atom.

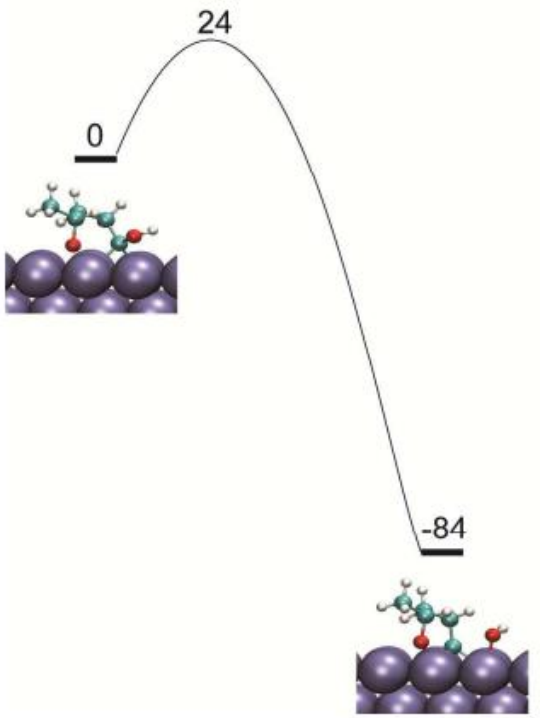

Appendix fig. 6 Hydrogen assisted hydrogenolysis of the acyl intermediate.

B3. Reaction pathway of GVL

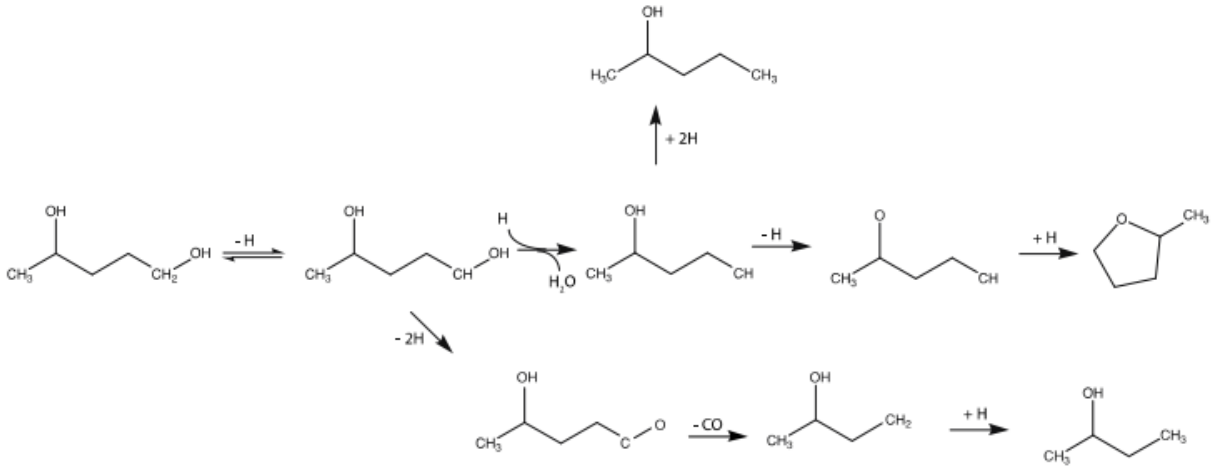

Appendix fig. 7 Possible reaction pathways for formation of MTHF, 2-BuOH and 2-PeOH from 1,4-PDO.

C. H/D exchange and DFT Energy profile in Chapter 4

C1. H/D Exchange

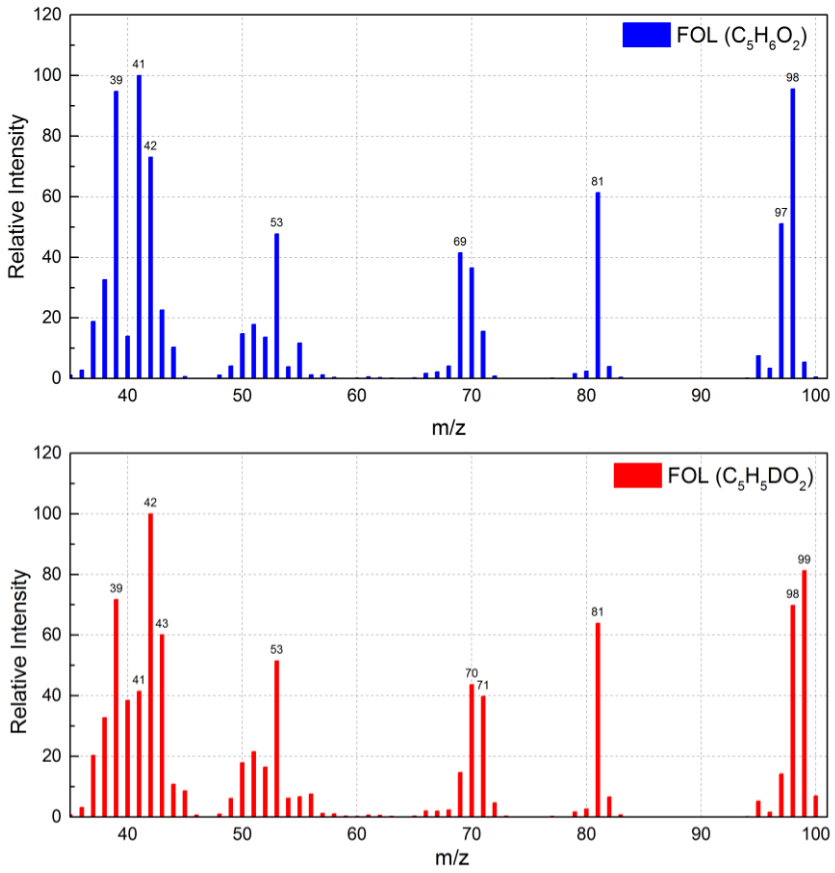

Appendix fig. 8 Full mass spectrum of FOL produced in H_2O (blue) and D_2O (red).

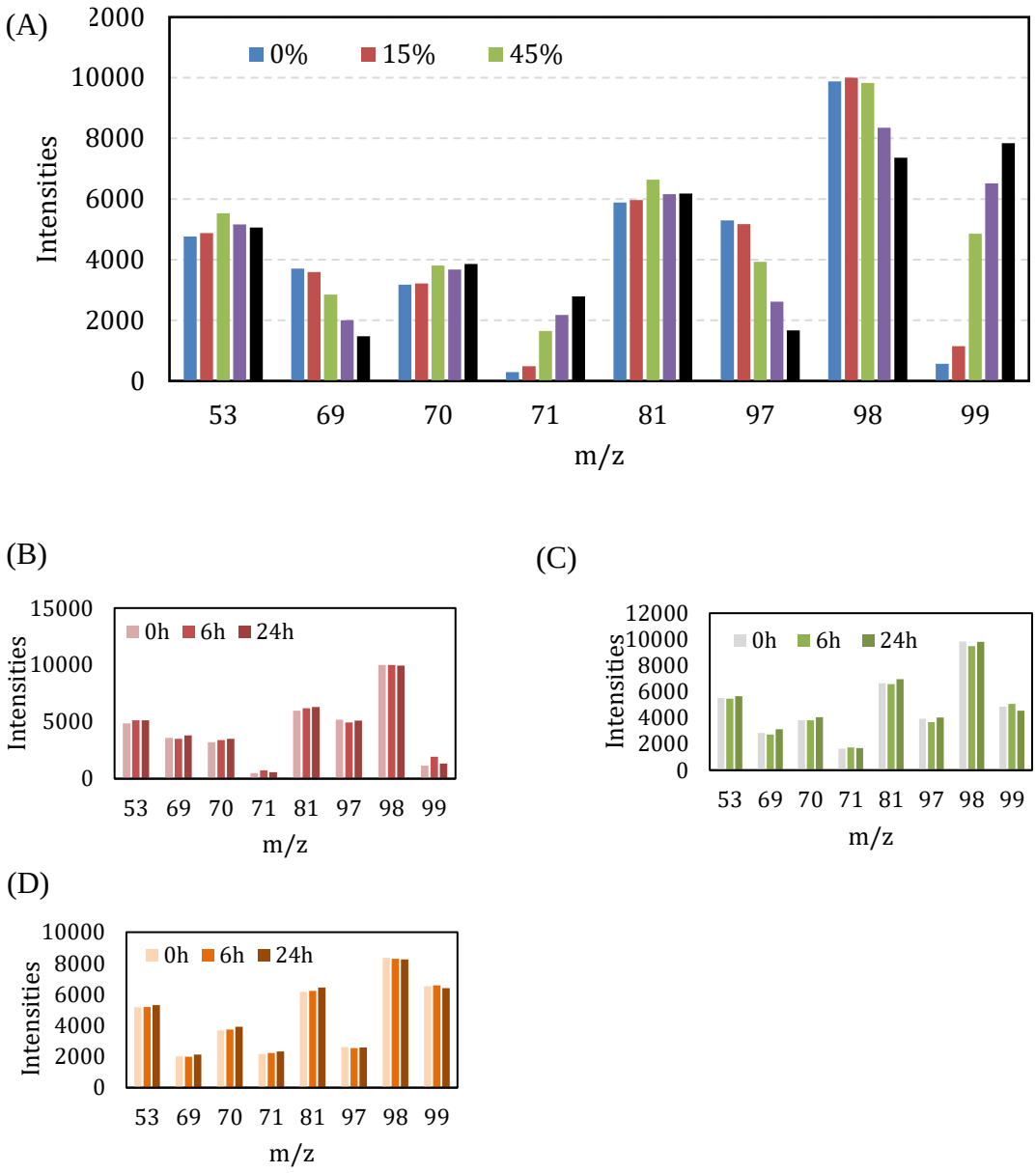

Appendix fig. 9 (A) Mass spectroscopy of FOL in mixtures with different D_2O percentage: 0% represents pure H_2O and 100% represent pure D_2O. The FOL concentrations were 0.1 M for all prepared solutions under room temperature. (B-D) Mass spectroscopy of FOL in mixtures with different time intervals: from left to right under same m/z is the time increment. B: FOL in 15% D_2O solution; C: FOL in 45% D_2O solution; D: FOL in 70% D_2O solution

We hypothesize that water participates in the reaction directly, and this causes the different reaction order in water and in cyclohexane. To prove or disprove it, we carried out a series of reactions of furfural hydrogenation in deuterated water (D2O) under the same reaction conditions.

The furfural hydrogenation reaction was carried out in D_2O under the same reaction conditions as in the other experiments. The products were analyzed at an overall FAL conversion of 50%. Full mass spectrum of FOL, THFAL and THFOL produced in H_2O and D_2O are shown in Appendix fig. 12. We indeed find D in the product – FOL, as evidenced particularly by the m/z=99 peak (deuterated O in the aldehyde group of FOL) in D_2O as compared to it in H_2O. This result seems to support the idea of proton shuttling, that is, the hydrogenation is mediated by D2O. However, we notice, as shown in Appendix fig.13 and discussed below, the quick H/D exchange between FOL and water makes it very challenging to identify the mechanism for the deuterated FOL.

The FOL aqueous solution was prepared at room temperature in pure H_2O, pure D_2O and then analyzed by GC-MS right after the preparation. As shown in Appendix fig. 13, deuterated FOL molecular ion, m/z = 99, appears in pure D2O, indicating the H atom of hydroxyl group in FOL has been exchanged with D instantly after the introduction of D2O under room temperature even without catalyst. The –OH group and D2O form hydrogen bonding network that allows D atoms to exchange with H readily. Notably, the concentration of FOL was much lower than the solvent D2O. The H atoms are supposed to be replaced by D atoms completely, resulting the disappearance of FOL molecular ion, which is m/z=98. On the contrary, the intensities of m/z=98 is as much as that of m/z=99 in pure D2O after the exchange. The MS spectra indicate that both regular FOL and deuterated FOL exist in the mixture.

The H-D exchange reaction was then carried out with various amount of D_2O-H_2O mixture and at different time intervals. As D_2O volume percentage increases in the mixture presented in Appendix fig. 13. Peaks of m/z=99 increases respectively. Therefore, H-D exchange reaction illustrates an equilibrium with D_2O. Higher percentage of D_2O yields more deuterated FOL in the mixture. To monitor the intensities evolution with time, the prepared solutions were later analyzed after 6 hours and 24 hours.

However, the intensities as a function of time, plotted in Appendix fig. 13 (B-D), remain constant for three mixtures. Therefore, the H-D exchange reaction happens drastically and reaches an equilibrium once FOL is mixed with D_2O.

Comparing the FOL H-D exchange results in pure D_2O with the FOL formed during furfural hydrogenation in D_2O, the ratios of m/z=99 to m/z=98 for both scenarios are similar, with 1.07 and 1.16 for each case. Unfortunately, the reaction of furfural hydrogenation going through water shuttling mechanism is unable to be unambiguously supported from isotope study due to the instant H-D exchange reaction once the FOL is being formed during the reaction.

C2. Energy profile of opposite sequence of furfural to furfuryl alcohol step in water

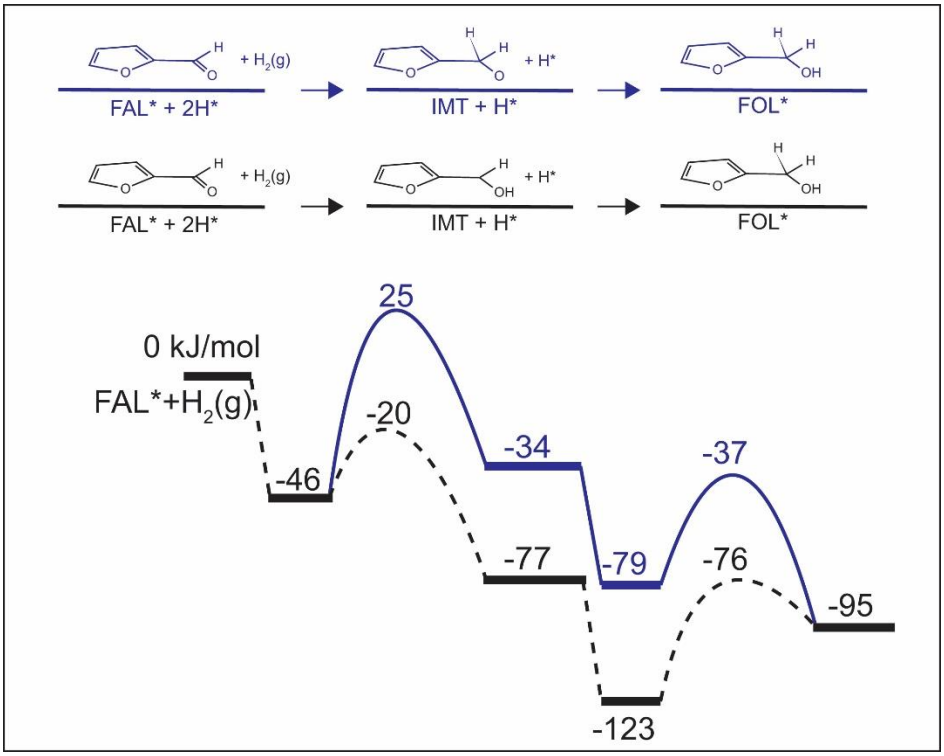

Appendix fig. 10 Reaction path of furfural hydrogenation on a Pd (111) surface in the presence of water. Different sequences ($C^{1st}O^{2nd}$ and $O^{1st}C^{2nd}$)of hydrogenation are compared. Only the DFT-calculated total energies were used to plot this figure and compare the two different reaction sequence. We were not able to precisely locate the transition state for the hydrogenation of the C in the $C^{1st}O^{2nd}$ scenario.

D. Computational Hydrogen Electrode Model for relating first principal study calculations to experimental results in Chapter 5

For a reaction step involving proton, electron pair transfer:

$$X^* + H^+ + e^- \rightarrow XH^*$$

The change in Gibbs free energy is:

$$\Delta G = G(XH^*) - G(X^*) - G(H^+) - G(e^-)$$

Considering the standard hydrogen electrode as reference. In equilibrium:

$$H^+{}_{(aq)} + \ e^- \leftrightarrow {}^1/_2\, H_{2\,(g)}$$

$$\mu(H^+) + \ \mu(e^-) = {}^1/_2\, \mu(H_{2\,(g)})$$

The change in Gibbs energy at 0V becomes:

$$\Delta G_{U=0} = G(XH^*) - G(X^*) - {}^1/_2\, G\left(H_{2\,(g)}\right)$$

When bias is introduced, the expression becomes:

$$\Delta G_{U=i} = G(XH^*) - G(X^*) - {}^1/_2\, G\left(H_{2\,(g)}\right) - neU$$

Based on the equation above, Bias affect was introduced to first principal calculations conducted at 0V to compare with experimental results.